Influence of the Particle Flux on Surface Modifications of Tungsten

Luxherta Buzi

Influence of the Particle Flux on Surface Modifications of Tungsten

Invloed van deeltjesflux op oppervlaktewijzigingen van wolfraam

Luxherta Buzi

Promoters: Prof. J-M. Noterdaeme, PhD, Prof. G. Van Oost, PhD, Prof. G. Bonhomme, PhD
Doctoral thesis submitted in order to obtain the academic degrees of
Doctor of Engineering Physics (Ghent University) and
Doctor of Physics (Lorraine University)

Department of Applied Physics
Head of Department: Prof. C. Leys, PhD
Faculty of Engineering and Architecture

École doctorale EMMA Lorraine
Collegium Sciences et Technologies
Directeur de l'ED: Prof. Denis Maillet, PhD
Faculté des Sciences et Technologies

Academic year 2014-2015

ISBN 978-90-8578-843-0
NUR 926
Wettelijk depot: D/2015/10.500/87

Het onderzoek voor dit doctoraat vond plaats in:
This research was performed at:

Forschungszentrum Jülich
Institute of Energy and Climate Research
Plasma Physics IEK-4
Leo-Brandt-Strasse
52428 Jülich
Germany

In samenweking met:
In collaboration with:

Dutch Institute For Fundamental Energy Research
Edisonbaan 14
3439 MN Nieuwegein
Netherlands

Ghent University
Faculty of Engineering and Architecture
Department of Applied Physics
St. Pietersnieuwstraat 41
9000 Ghent
Belgium

Lorraine University
Institute Jean Lamour
Faculty of Science, BP 70239
F-54506 Vandoeuvre-ls-Nancy Cedex
France

University of California at San Diego
Center for Energy Research
9500 Gilman Dr.
La Jolla, 92093-0417
California

Doctoral guidance committee

Supervisors:	**Prof. Dr. Bernhard Unterberg** *Ruhr-Universität Bochum, Forschungszentrum Jülich* **Dr. Gregory De Temmerman** *ITER Organization, former DIFFER institute*
Promoters:	**Prof. Dr. ir. Guido Van Oost** *Ghent University* **Prof. Dr. ir. Jean-Marie Noterdaeme** *Ghent University* **Prof. Dr. Gérard Bonhomme** *Lorraine University*

Members of the examining board

Chairman:	**Chair: Prof. Dr. Rik Van de Walle** *Ghent University* **Co-chair: Dr. Elisabeth Gautier** *Lorraine University*
Secretary:	**Prof. Dr. Kim Verbeken** *Ghent University*
Reading committee:	**Prof. Dr. Kim Verbeken** *Ghent University* **Prof. Dr. Rudolf Neu** *Technische Universität München* **Prof. Dr. Valery Kurnaev** *National Research Nuclear University MEPhI* **Prof. Dr. Bernard Unterberg** *Ruhr-Universität Bochum*
Further members of the examining board:	**Prof. Dr. ir. Jean-Marie Noterdaeme** *Ghent University* **Prof. Dr. ir. Guido Van Oost** *Ghent University* **Prof. Dr. Gérard Bonhomme** *Lorraine University* **Dr. Gregory De Temmerman** *ITER Organization* **Prof. Dr. Russell Doerner** *University of California in San Diego* **Prof. Dr. Christian Linsmeier** *Ruhr-Universität Bochum*

Table of Contents

Acknowledgments i

List of publications iii

Nederlandse samenvatting v

English summary ix

1 Introduction 1-1
References . . . 1-6

2 Basic mechanisms of plasma-material interaction 2-1
2.1 Hydrogen retention in tungsten . . . 2-2
2.1.1 Hydrogen mobility . . . 2-5
2.1.2 Trapping and surface effects . . . 2-7
2.1.3 Modeling of the thermal desorption spectroscopy data . . . 2-8
2.2 Mechanisms for blister formation . . . 2-11
2.3 Plasma loading conditions expected in the ITER divertor . . . 2-14
2.4 Plasma loading impact on surface modifications and retention . . . 2-16
2.4.1 Ion fluence and surface temperature . . . 2-16
2.4.2 Material microstructure . . . 2-19
2.4.3 Combined He/D exposure . . . 2-20
2.4.4 Transient heat and particle loads . . . 2-22
References . . . 2-24

3 Experimental setup and analysis techniques 3-1
3.1 Linear plasma devices . . . 3-1
3.1.1 Magnum/Pilot-PSI . . . 3-2
3.1.2 PSI-2 . . . 3-5
3.1.3 PISCES-A . . . 3-7
3.2 Analysis techniques . . . 3-10
3.2.1 Electron microscopy . . . 3-10
3.2.2 Profilometry . . . 3-11
3.2.3 Secondary Ion Mass Spectrometry (SIMS) . . . 3-11
3.2.4 Nuclear Reaction Analysis (NRA) . . . 3-12
3.2.5 Thermal Desorption Spectroscopy (TDS) . . . 3-14

3.3 Sample preparation 3-15
References 3-19

4 Experimental results and discussion **4-1**
4.1 Deuterium plasma exposure 4-1
4.1.1 Small Grain Tungsten (SGW) 4-2
4.1.2 Large Grain Tungsten (LGW) 4-8
4.1.3 Recrystallized Tungsten (RecW) 4-15
4.1.4 Single Crystal Tungsten (SCW) 4-20
4.1.5 Summary and modeling results 4-26
4.2 Mixed D/He plasma exposure of recrystallized tungsten 4-35
4.3 He and H transient heat and particle loads on polycrystalline tungsten 4-39
References 4-47

5 Conclusions and outlook **5-1**

A Material selection **A-1**
A.1 Chemical content and material specifications of tungsten bars . . . A-1

B D experiments **B-1**
B.1 TDS profiles of tungsten samples after exposure to pure D plasma B-1

C He/H experiments **C-1**
C.1 Surface analysis of Mo-deposited tungsten samples after exposure to H and He plasma C-1

List of Figures

1.1 Schematic view of a remotely removable cassette of the ITER divertor [2] 1-2

2.1 Main processes involved in retention and recycling of hydrogen at the wall of a fusion reactor. Hydrogen atom sites in the lattice: (a) Surface adsorption, (b) sub-surface layers adsorption, (c) Interstitial, (e, d) Vacancies, (f) Grain boundary, (g) Dislocation 2-2
2.2 Qualitative potential energy diagram of hydrogen transport in tungsten [4] 2-4
2.3 Diffusion coefficients of hydrogen in tungsten from modeling and experiments [5, 7] 2-6
2.4 Normalized permeation coefficients of hydrogen in tungsten at 300 Pa [7] 2-6
2.5 TDS simulation (without implantation) for a trapping energy of 2.2 eV without re-trapping ($\nu_{trap} = 0$). De-trapping frequency ($\nu_{de-trap}$) is varied for several cases 2-11
2.6 Overpressurized bubble growth model based on interstitial loops punching from a gas-filled cavity ([24] and references herein) . . 2-12
2.7 Stages of the inter-bubble fracture model: (a) an amount of overpressurized bubbles with the same radii, (b) crack formation due to the tensile stress exerted perpendicular to the bubble-free plan, (c) adjacent bubbles join the crack, (d) which expands further, (e) forms a lenticular crack (f) and evolves into a blister [24] 2-13
2.8 Plasma profile (temperature, density, particle and heat flux) along the inner and outer ITER divertor for a semi-detached plasma scenario (highly radiative divertor operation [28]). Low and high flux notations represent the deuterium particle fluxes selected to be studied in the experiments 2-14
2.9 Surface temperature variation along the outer target at ITER during He and DT phase of operation [30] 2-15
2.10 Total deuterium retention in polycrystalline tungsten at various ion fluences [29] 2-16
2.11 Total deuterium retention in polycrystalline tungsten as a function of exposure temperature [29] 2-17

2.12 Blister formation domain as a function of surface temperature and particle flux: Shu2009 [42], Xu2014 [43], Sharpe2009 [41], Tyburska2010 [44], Alimov2009 [32] 2-18
2.13 Surface nanostructures formation on tungsten as a function of exposure temperature and incident ion energy in He plasma performed at NAGDIS-II and PISCES-B (b) SEM images at the specific conditions corresponding (i)-(iv) [57] 2-21

3.1 Schematic overview of Pilot-PSI linear plasma device [5] 3-2
3.2 Tungsten sample and the molybdenum clamping ring used to mount the sample at Pilot and Magnum-PSI 3-3
3.3 On the left graph are plotted the electron density, temperature and ion flux profiles at Magnum-PSI taken from the Thomson scattering measurements (sample LGW/530K/HF). On the right graph is given the heat flux profiles as a function of applied discharge current and magnetic field during plasma operation at Pilot-PSI [2] . 3-4
3.4 Infrared camera temperature profile along the sample recorded on the sample exposed to Magnum-PSI 3-4
3.5 Time evolution of surface temperature recorded on the sample exposed to Magnum-PSI 3-5
3.6 Schematic overview of PSI-2 linear plasma device [11] 3-5
3.7 Sample holder with samples exposed to PSI-2. Temperature was regulated by changing the thermal contact with the cooled holder . 3-6
3.8 On the left graph is plotted the electron density, temperature and ion flux profiles at PSI-2 taken from the Langmuir probe measurements and on the right is given a picture of samples exposed at PSI-2. Temperature on the back of the sample measured by the thermocouple is around 1370 K 3-6
3.9 Schematic overview of PISCES-A linear plasma device [13] . . . 3-7
3.10 Experimental results on the relation between the ion ratio in the plasma from the intensity of the HeI and D_γ lines [18] 3-9
3.11 Spectroscopic measurements of the mixed He/D plasma at a total gas pressure $P_{D_2+He} \sim 9.6 \cdot 10^{-3}$ mbar 3-9
3.12 Comparison of the experimental data and the best fit to the depth profile from the forward calculation result, each peak corresponding to energies 0.69-4.5 MeV ('W8'-sample) 3-13
3.13 Thermal desorption spectroscopy profiles of various tungsten microstructures after exposure to high flux deuterium plasma ($\sim 10^{24} m^{-2} s^{-1}$) at about 500 K 3-15
3.14 Microstructure analysis of the targets used in the experiments performed with the Electron Backscatter Diffraction method (EBSD) to illustrate the grain size, shape and orientation of the grains of Small Grain Tungsten (SGW ~20 μm) and Large Grain Tungsten (LGW ~40 μm) 3-16

3.15 Scanning electron microscope image of the recrystallized and single crystal samples taken before the plasma exposure 3-17
3.16 Microstructure analysis of the targets used in the experiments performed with the Transmission Electron Microscope (TEM) 3-17

4.1 SEM images taken on the SGW samples after exposure to D plasma at PSI-2 (a)-(d) and Pilot-PSI (a1)-(d1) at a fluence of 10^{26} m^{-2} and incident ion energy of 40 eV. 4-3
4.2 TDS profiles of SGW samples exposed at low flux density (LF) and high flux density (HF) pure deuterium plasma 4-4
4.3 Deuterium depth distribution profiles in tungsten as measured with NRA (top) and SIMS (bottom) techniques 4-6
4.4 Total deuterium retention for SGW samples exposed to two different particle flux density ($\sim 10^{22}$ $m^{-2}s^{-1}$ and $\sim 10^{24}$ $m^{-2}s^{-1}$) at 40 eV of incident ion energy and 10^{26} m^{-2} total fluence as given from TDS and NRA measurements. 4-7
4.5 SEM images of the Large Grain Tungsten samples (LGW) after exposure at ion fluence 10^{26} m^{-2}; (a)-(d) are the low flux exposures and (a1)-(d1) are the high flux exposures at the respective surface temperatures. 4-9
4.6 (A-D) Higher magnification SEM images of samples after exposure at high flux. At 870 K, two types of blisters were present; blisters in the tens nm-range and blisters in the hundred nm-range as indicated with red circles. (B1) and (B2) are the FIB - cross sectional cut images after exposure to high particle flux at 630 K. . 4-10
4.7 Blister diameter (Φ) is given as a function of exposure temperature and incident flux density for two sets of experiments, large and small grain tungsten samples (LGW, SGW) 4-11
4.8 TDS spectra of desorbed deuterium from samples exposed to low ($\sim 10^{22} m^{-2}s^{-1}$) and high ($\sim 10^{24} m^{-2}s^{-1}$) particle flux density. 4-12
4.9 TDS and NRA results on total deuterium retention in tungsten samples as a function of surface temperature, exposed to a fluence of 10^{26} m^{-2} and various surface temperatures. The blue and red curves represent the exposures to low and high flux density respectively. 4-13
4.10 SEM images taken on the RecW samples after exposure to D plasma at PSI-2 (a)-(d) and Pilot-PSI (a1)-(d1) at a fluence of $10^{26} m^{-2}$ and incident ion energy of 40 eV. 4-15
4.11 SEM images taken on the RecW sample after the cross-sectional cutting of one of the blisters with the focused ion beam (FIB) . . . 4-16
4.12 Deuterium depth distribution profiles in recrystallized tungsten samples as measured with the NRA technique 4-16
4.13 TDS spectra of desorbed deuterium from the recrystallized tungsten samples exposed to low ($\sim 10^{22}$ $m^{-2}s^{-1}$) and high ($\sim 10^{24}$ $m^{-2}s^{-1}$) particle flux density. 4-17

4.14 NRA and TDS results on total deuterium retention on the recrystallized tungsten samples as a function of surface temperature, exposed to a fluence of 10^{26} m^{-2} and various surface temperatures. The blue and red curves represent the exposures to low and high flux density respectively. 4-19
4.15 SEM images taken on the SCW samples after exposure to D plasma at PSI-2 (a)-(c) and Pilot-PSI (a1)-(c1) at a fluence of 10^{26} m^{-2} and incident ion energy of 40 eV. 4-20
4.16 Illustration of (110) and (221) crystallographic planes in a bcc lattice and the corresponding angles forming with (111) plan and [111] direction. 4-21
4.17 Deuterium depth distribution profiles in single crystal tungsten samples as measured with the NRA technique 4-23
4.18 TDS spectra of desorbed deuterium from the single crystal tungsten samples exposed to low ($\sim 10^{22}$ $m^{-2}s^{-1}$) and high ($\sim 10^{24}$ $m^{-2}s^{-1}$) particle flux density. 4-24
4.19 TDS results on total deuterium retention on the single crystal tungsten samples as a function of surface temperature, exposed to a fluence of 10^{26} m^{-2} and various surface temperatures. The blue and red curves represent the exposures to low and high flux density respectively. 4-24
4.20 Lateral blister size is given as a function of exposure temperature and incident flux density. Empty symbols indicate the lack of blistering. The red stars (★), pentagons (⬠) and filled diamonds (◆) represent the present work results on blistering of the "as received" (LGW and SGW), RECW and SCW samples, respectively. The literature data (blue symbols) correspond to polycrystalline tungsten material [4, 10, 11, 22–24] 4-26
4.21 TDS results on total deuterium retention on the four different microstructure tungsten samples as a function of surface temperature, exposed to a fluence of $10^{26}m^{-2}$ and various surface temperatures. The blue and red curves represent the exposures to low and high flux density respectively. 4-28
4.22 CRDS simulation of ScW and RecW samples 4-33
4.23 CRDS simulation of SGW samples 4-34
4.24 Temperature evolution during exposure at Pilot-PSI used to simulate implantation and desorption 4-34
4.25 SEM images taken on the RecW samples after exposure to 5% He/D plasma at PISCES-A at a fluence of 10^{26} m^{-2} and incident ion energy of 40 eV. The surface temperature was varied from 520 to 1090 K. 4-36
4.26 SEM images taken on the sample after exposure to 5% He/D plasma at PISCES-A at a fluence of 10^{26} m^{-2} and surface temperature of 1090 K. From the cross sectional FIB cuts, the nanorods are visible at a length of above 200 nm from the surface 4-37

4.27 Deuterium depth profiles of recrystallized samples exposed to pure deuterium plasma and mixed plasma with 5% He content 4-37
4.28 Total deuterium retention as calculated from the NRA measurements for the present exposures of the recrystallized samples and previous results from polycrystalline samples [38] 4-38
4.29 Infrared camera temperature profiles during one plasma shot in He, where steady-state and transient loads were combined. The real temperature was converted from digital data and calculated assuming the temperature dependent emissivity coefficients 4-39
4.30 Tungsten samples exposed to He plasma for 100 s at 850 K (a1-a3) and 1070 K (b1-b3) at 660 and 560 plasma pulses respectively . . 4-41
4.31 Tungsten samples exposed to H plasma for 100 s at 800 K (e1, e2) and 1120 K (f1, f2) at 660 and 560 plasma pulses respectively. The relevant exposure in steady state H plasma at 770 K is given in figures m1 and m2 4-42
4.32 Tungsten samples exposed to H plasma for 100 s and 960 plasma pulses at 670 K (g1, g2) and 980 K (h1, h2). The relevant exposure in steady state H plasma at 1070 K is given in figures n1 and n2 . 4-42
4.33 ΔT is normalized over the first pulses and plotted versus exposure time for all samples exposed to He transients. On the left plot, samples were exposed to the pulsed plasma source (560, 660 pulses) and on the right one, a laser was used to get 8595 pulses . 4-43
4.34 ΔT is normalized over the first pulses and plotted versus exposure time for all samples exposed to H transients. In both cases, the pulsed plasma source was used to achieve 560 and 660 pulses (on the left) and 960 pulses (on the right plot) 4-44

C.1 SEM images on the ITER-grade tungsten samples exposed at Pilot-PSI to steady state He plasma for 100 s C-1
C.2 SEM images on the ITER-grade tungsten samples exposed at Pilot-PSI to steady state He plasma for 1000 s C-2
C.3 SEM images on the ITER-grade tungsten samples exposed at Pilot-PSI to He plasma for 1000 s and 8595 laser pulses C-2
C.4 Elemental analysis performed with EDX on the IGW3 sample after exposure to steady state He plasma for 1000 s. C-3

List of Tables

3.1 Main plasma parameters of low and high flux LPDs. SS stands for steady state operation [1–3] 3-1

4.1 Exposure conditions of SGW samples and results on the areal density of blisters and TDS peak temperature 4-5
4.2 Exposure conditions of LGW samples and results on the areal density of blisters and TDS peak temperature 4-12
4.3 Exposure conditions of RECW samples and results on the areal density of blisters and TDS peak temperature 4-18
4.4 Angles between planes of various gliding systems in a bcc lattice . 4-22
4.5 Exposure conditions of SCW samples and results on the areal density of blisters and TDS peak temperature 4-23
4.6 Main parameters included in the CRDS modeling 4-31
4.7 RECW samples exposed at PISCES-A at fluence $10^{26}\ m^{-2}$. . . . 4-35
4.8 ITER-grade tungsten samples exposed in Pilot-PSI linear plasma device to He and H plasmas, under steady-state conditions and transient heat and particle loads. The highlighted samples were deposited with Mo during the plasma exposure. 4-45
4.9 ITER-grade tungsten samples exposed in Pilot-PSI linear plasma device to He and H plasmas, under steady-state conditions and transient heat and particle loads. The highlighted samples were deposited with Mo during the plasma exposure. 4-46

A.1 Chemical composition of W bars A-1
A.2 Grain size of the W bar. Samples were cut perpendicular to the rolling direction A-1

List of Acronyms

C

CRDS	Coupled Reaction-Diffusion System

E

EBSD	Electron Backscattering Diffraction

F

FIB	Focused Ion Beam

I

ITER	International Thermonuclear Experimental Reactor

J

JET	Joint European Torus

L

LGW	Large Grain Tungsten
LPD	Linear Plasma Device

N

NRA	Nuclear Reaction Analysis

P

PFC	Plasma Facing Component
PMI	Plasma Material Interaction
PSI	Plasma Surface Interaction

R

RECW	Recrystallized Tungsten
RMS	Root Mean Squared

S

SEM	Scanning Electron Microscope
SCW	Single Crystal Tungsten
SGW	Small Grain Tungsten
SIMS	Secondary Ion Mass Spectroscopy

T

TDS	Temperature Desorption Spectroscopy
TEM	Transmission Electron Microscopy
TMAP	Tritium Migration Analysis Program

Acknowledgments

This was the most international PhD thesis I could have ever imagined, being enrolled in prestigious universities and research institutes was an exceptional experience. In the first place, I would like to thank my doctoral guidance committee for this unique opportunity and for dealing with the rather complicated administrative procedures to make this international collaboration possible. Many thanks to Kathleen Van Oost for handling the practical matters with the highest efficiency.

I would like to express my immense gratitude to my Doktorvater, Prof. Guido Van Oost for his invaluable support, encouragement and for always responding to my questions and queries so promptly. Also, I would like to sincerely thank my supervisors, Prof. Bernhard Unterberg and Dr. Greg De Temmerman, for the fruitful scientific discussions, motivation and patience. Their guidance constantly helped me throughout the research and writing of this thesis.

Many thanks also to Prof. Christian Linsmeier for his promptness in discussing my experimental results and for providing continuous motivation and new ideas. I appreciate the enormous support of Dmitry Matveev with the CRDS modeling which improved significantly the understanding of the results.

This work was done with the help of many people, who supported, welcomed me and gave access to the laboratories and research facilities. Without their precious support it would have not been possible to conduct this research.

At Forschungszentrum Jülich, I would like to thank Timo Dittmar for his wise advices and the help with NRA data. I am grateful to Michaele Freisinger, Kevin Kiss and Günter Esser for their help with the TDS measurements. Many thanks to Marcin Rasinski for assisting me with the SEM and FIB analysis. Michael Reinhart and all the technicians provided me with great help concerning PSI-2 operation. I am also very grateful to Uwe Breuer for the SIMS measurements and valuable discussions. Thanks to Maren Hellwig and Dmitry Matveev for being excellent office mates and Jorge Martin for his unconditional friendship.

Without the technical support of the very professional and talented PSI team, my work at DIFFER wouldn't have been possible. I mention here Irem Tanyeli, Sebastien Bardin, Kiril Bystrov, and Long Cheng for operating Pilot-PSI but also Hennie van der Meiden, Marc van de Pol and Richard Al for their help in solving technical problems.

At SCK · CEN lab in Mol, I would like to thank Andrey Dubinko for the TEM

analysis and Petr Grigorev and Dmitry Terentyev for the useful discussions. Also, I appreciate the help from Tom Wauters for his comments on the summary and its translation to Dutch.

I would like to thank Thomas Schwarz-Selinger for the great help with the NRA measurements and Michael Fußeder and Joachim Dorner for operating the accelerator at IPP Garching. Many thanks to Stefan Elgeti for the support with SEM analysis and Gabriele Matern for teaching me the sample polishing procedure.

One of the most remarkable visits during these three years was the PISCES lab at UCSD. I am very thankful to Russ Doerner who hosted me at the University and made my stay in San Diego pleasant and scientifically enriching.

Finally, writing my thesis at the University of Lorraine in Nancy was much easier and pleasant thanks to my friends, Andrey Shalpegin and Mikael Desecures, who shared the same stage of the PhD work.

This work was supported by the European Commission and carried out within the framework of the Erasmus Mundus International Doctoral College in Fusion Science and Engineering (FUSION-DC).

I dedicate this work to my family.
-Këtë punë ja dedikoj familjes sime-

Nancy, August 2015
Luxherta Buzi

List of publications

Publications on this topic:

1. **L. Buzi**, G. De Temmerman, B. Unterberg, M. Reinhart, A. Litnovsky, V. Philipps, G. Van Oost, S. Möller, *Influence of particle flux density and temperature on surface modifications of tungsten and deuterium retention*, Journal of Nuclear Materials 455 (2014) 316-319

2. **L. Buzi**, G. De Temmerman, B. Unterberg, M. Reinhart, T. Dittmar, D. Matveev, Ch. Linsmeier, U. Breuer, A. Kreter, G. Van Oost, *Influence of tungsten microstructure and ion flux on deuterium plasma-induced surface modifications and deuterium retention*, Journal of Nuclear Materials 2014, doi:10.1016/j.jnucmat.2014.12.006

3. M. Reinhart, A. Kreter, **L. Buzi**, M. Rasinski, A. Pospieszczyk, B. Unterberg, Ch. Linsmeier, *Influence of plasma impurities on the deuterium retention in tungsten exposed in the linear plasma generator PSI-2*, Journal of Nuclear Materials 2014, doi:10.1016/j.jnucmat.2014.11.045

4. A. Kreter, **L. Buzi**, G. De Temmerman, T. Dittmar, R.P. Doerner, Ch. Linsmeier, D. Nishijima, M. Reinhart, B. Unterberg, *Fuel Retention and Erosion of Metallic Plasma-Facing Materials under the Influence of Plasma Impurities*, Proceedings of the 25th IAEA Fusion Energy Conference, St. Petersburg, 13-18 October 2014, paper-ID EX/4-3

5. A. Kreter, B. Unterberg, D. Borodin, **L. Buzi**, A. Huber, Ch. Linsmeier, E. Marenkov, A. Pospieszczyk, M. Reinhart, G. Sergienko, I. Steudel, M. Wirtz, *Overview of recent results on plasma-material interaction studies in the linear plasma device PSI-2*, Proceedings of the 10th International Conference on Open Magnetic Systems for Plasma Confinement (OS 2014)

6. P. Grigoriev, **L. Buzi**, A. Bakaeva, D. Terentyev, G. De Temmerman, G. Van Oost, J-M. Noterdaeme, *Numerical analysis of TDS spectra under high and low flux plasma exposure conditions*, Submitted to Physica Scripta, 2015, PHYSSCR-103262

Publications on other topics:

7. A. Litnovsky, Y. Krasikov, V. Kotov, M. Matveeva, A. Panin, L. Vera, **L. Buzi**, O. Neubauer, W. Biel, D. Nicolai, Ph. Mertens, Ch. Linsmeier, *Mirror Station for studies of the protection of diagnostic mirrors from impurity contamination in ITER: Design and first results*, Fusion Engineering and Design 2015, doi:10.1016/j.fusengdes.2015.02.039

8. A. Litnovsky, M. Matveeva, **L. Buzi**, L. Vera, Y. Krasikov, V. Kotov, A. Panin, P. Wienhold, V. Philipps, D. Castano Bardawil, T. Akiyama, W. Biel, O. Neubauer, Ph. Mertens, Ch. Linsmeier, D. Reiter, P. Boerner, M. Freisinger, S. Richter, *Studies of protection and recovery techniques of diagnostic mirrors for ITER*, Nucl. Fusion 55 (2015) 093015 (9pp)

9. A. Litnovsky, M. Matveeva, A. Herrmann, V. Rohde, M. Mayer, K. Sugiyama, K. Krieger, V. Voitsenya, G. Vayakis, A.E. Costley, R. Reichle, G. De Temmerman, S. Richter, U. Breuer, **L. Buzi**, S. Moeller, V. Philipps, U. Samm, P.Wienhold and the ASDEX Upgrade Team, *First studies of ITER-diagnostic mirrors in a tokamak with an all-metal interior: results of the first mirror test in ASDEX Upgrade*, Nucl. Fusion 53 (2013) 073033 (7pp)

Nederlandse samenvatting
–Summary in Dutch–

Tungsten is geselecteerd als functioneel materiaal voor de ITER divertor voor zijn gunstige thermische en fysische eigenschappen. De oppervlakte temperatuur, de dichtheid van de deeltjesflux, en de respectievelijke energie zal variëren over verschillende grootteordes langs het divertor-oppervlak, met waarden van respectievelijk 370-1370 K, 10^{20}-10^{24} $m^{-2}s^{-1}$, en 0.1-100 eV. Wolfraam kan, blootgesteld aan dergelijke omstandigheden, erosie, scheurvorming en andere oppervlakte-modificaties ondergaan die de thermische en mechanische eigenschappen beïnvloeden. Een andere zorg is de retentie van geïmplanteerde radioactieve brandstofatomen (tritium) in het materiaaloppervlak en de verspreiding ervan doorheen de bulk. Een aanzienlijke aantal onderzoeken behandelen retentie en plasma-geïnduceerde oppervlakte-modificaties, voornamelijk met aandacht voor het effect van de ionenenergie, ionenfluentie en oppervlaktetemperatuur, terwijl zeer weinig kennis bestaat over de invloed van de plasmaflux. De resultaten zijn grotendeels onsamenhangend en tonen soms een gebrek aan consistentie.

Het doel van dit proefschrift is om een samenhangend beeld te bieden van het gedrag van wolfraam, blootgesteld aan plasmacondities die relevant zijn voor toekomstige fusiereactoren. Een systematisch onderzoek naar de impact van de plasmafluxdichtheid en blootstellingstemperatuur op de oppervlaktewijzigingen en waterstofaccumulatie in wolfraam werd uitgevoerd door middel van experimenten op de lineaire plasma-apparaten PSI-2 bij Forschungszentrum Jülich, Pilot-PSI en Magnum-PSI bij DIFFER en PISCES-A bij UCSD. De correlatie tussen de deeltjesfluxdichtheid, blootstellingstemperatuur, oppervlaktemodificaties en waterstofretentie in wolfraam werd onderzocht voor verschillende materiaalmicrostructuren. Drie soorten polykristallijne wolfraam (thermisch behandeld bij 1273 en 2273 K) en monokristallijne wolfraam-monsters (110 kristaloriëntatie) werden blootgesteld aan deuterium-plasma bij temperaturen van 530-1170 K, en twee verschillende reeksen van deuterium-ionenfluxen (lage en hoge flux: $\sim 10^{22}$ en $\sim 10^{24}$ $m^{-2}s^{-1}$). Alle blootstellingen werden uitgevoerd bij dezelfde ionenenergie van 40 eV en deeltjesfluentie van $\sim 10^{26}$ m^{-2}. De blootgestelde monsters werden post-mortem geanalyseerd met behulp van verschillende beeldvormings- en analysetechnieken voor oppervlakken (microscopie, thermische desorptie spectroscopie en ionenbundel-analyse).

Het verhogen van de deeltjesflux met twee grootte-ordes veroorzaakt vorming van waterstof blisters bij temperaturen boven 700 K, terwijl dit gewoonlijk afwezig

is onder lage ionenfluxen. Kleine waterstof blisters van enkele tientallen nanometers en maximaal 1 μm zijdelingse omvang werden respectievelijk gedetecteerd op gegloeide polykristallijne en monokristallijne wolfraam-monsters. Waterstof blisters waren evenwel afwezig op gerekristalliseerde monsters behalve in geval van lage flux en lage blootstellingstemperatuur waar grote waterstof blisters van ongeveer 10 μm en holtes langs de korrelgrenzen verschenen.

De totale deuteriumretentie werd gemeten door thermische desorptiespectroscopie (TDS). In de testen met lage blootstellingstemperaturen was de opgenomen deuteriumfractie 1-2 grootteordes hoger na blootstelling aan een lage flux in vergelijking met een hoge flux. Een tegengestelde tendens van de totale deuteriumretentie werd waargenomen bij blootstelling aan hoge temperaturen. Dit heeft tot gevolg dat het maximum van de totale waargenomen deuteriumretentie bij een hogere temperatuur ($\sim$850 K) optreedt bij een hoge invallende deeltjesflux, en voor lage temperaturen ($\sim$650 K) bij blootstelling aan lage fluxen. In het algemeen zijn deze experimentele resultaten voor deuteriumretentie gelijk voor alle onderzochte wolfraam microstructuren. De totale deuteriumretentie vermindert echter bij hoge temperaturen en de maximale retentie ligt lager bij blootstelling aan hoge flux. Door de verschuiving van de maximale retentie bij hogere temperaturen, ligt de hoeveelheid vastgehouden deuterium hoger bij hoge flux dan bij lage flux in geval van temperaturen boven 800 K, terwijl deze dan nog steeds ongeveer een grootteorde lager is dan de maximale retentie bij lage flux.

De hierboven genoemde observaties met betrekking tot deuteriumretentie in wolfraam kunnen worden toegeschreven aan het samengaan van processen die schade toedienen aan het materiaal, deuterium-uitwisseling tussen materiaal en plasma en deuteriumdiffusie dieper in de bulk. Om dezelfde totale fluentie te bekomen bij lage fluxen zijn langere blootstellingstijden nodig dan bij blootstelling aan hogere fluxen. Uitgaande van een diffusielengte-schaling met de vierkantswortel van de tijd, levert een fluxverschil van een factor 100 een verschil in diffusiediepte van een factor 10 op. De lange blootstellingstijden bij lage fluxen en hoge temperaturen bewerkstelligen dus deuteriumdiffusie in het materiaal, alsook desorptie aan het naar het plasma-gekeerde oppervlak. Bij hoge deeltjesfluxen kunnen grotere concentratiegradiënten van deuterium verwacht worden, wat potentieel leidt tot grotere materiële schade en / of snellere groei van deuterium-gevulde bellen of holtes. Tegelijkertijd maakt diffusie van deuterium diep in het materiaal deuterium-trapping mogelijk op intrinsieke roosterfouten zoals vacatures, dislocaties en korrelgrenzen bij polykristallijne monsters. Voor typische korrelgroottes van ongeveer een aantal μm tot enkele tientallen μm zorgen korte blootstellingstijden niet voor efficiënte deuteriumdiffusie door de korrelgrenzen, en wordt het dus vermoedelijk gevangen op intra-granulaire roosterdefecten. Dislocatielussen en korrelgrenzen kunnen zo optreden als snelle diffusiepaden voor deuterium, zowel in de richting van de bulk als van het oppervlak. Tegelijkertijd kunnen knikken en jogs op dislocatielijnen en onregelmatige korrelgrenzen dienen als kiemplaatsen voor deuteriumaccumulatie en groei van bellen, bijvoorbeeld door het dislocatieloop-punching-mechanisme.

Om een inzicht te krijgen in de bindingsenergieën van deuterium vastgehou-

den in wolfraam voor de experimenten beschreven in dit werk, werden simulaties van de gemeten thermische desorptie spectra uitgevoerd met behulp van de reactiesnelheidsvergelijking-benadering geïmplementeerd in de Gekoppelde Reactie Diffusie Systeem (CRDS) code. De TDS pieken kunnen redelijk goed worden gereproduceerd in de veronderstelling van één bindingsenergie van 2.2 eV voor gerekristalliseerd wolfraam, twee bindingsenergieën van 1.9 eV en 2.0 eV voor monokristallijn wolfraam en 2.0 eV en 2.3 eV voor de andere polykristallijne monsters. Vanuit fysisch oogpunt kunnen deze bindende energieën worden verklaard door holtevorming bij kiemplaatsen op dislocatielussen en korrelgrenzen. Deuterium wordt vervolgens gevangen op de binnenoppervlakken van dergelijke lege ruimtes gevormd door loop-punching of vacature-clustering. De energiebarrière voor deuterium om van het binnenoppervlak van de holte in de materiaalbulk te bewegen zou dan vergelijkbaar zijn met die van deuteriumatomen op een vrij wolfraam oppervlak, geschat op ongeveer 2 eV in de literatuur.

In ITER zal het divertorplasma een concentratie heliumionen bevatten als restproduct van de fusiereacties. Daarom werd er verder experimenteel onderzoek uitgevoerd naar het effect van He nano-bellen, gevormd aan het materiaaloppervlak van wolfraam onder gelijktijdige D/He blootstelling. De aanwezigheid van 5% He ionen in een deuteriumplasma verminderde de totale deuteriumretentie in gerekristalliseerd wolfraam en veroorzaakte vlok(fuzz)-vorming bij verhoogde temperaturen ($>$1000 K).

De blootstellingen aan ITER-relevante continue en gepulste warmte- en deeltjesfluxen, die ELMs in ITER simuleren in termen van amplitude, frequentie (10 Hz) en energiedichtheden (0.2-0.5 MJm^{-2}), werden uitgevoerd in Pilot-PSI. Hiermee werd het effect van thermische schokken op de hierboven genoemde morfologische veranderingen van wolfraam beoordeelt. De stabiele en tijdelijke deeltjes en warmtebelasting werden verkregen door middel van een gepulste plasmabron en een hoogvermogen laser (ms-pulsduur) indien een langereblootstellingstijd nodig was. Blootstelling van wolfraam specimens aan He-plasmapulsen veroorzaakte de vorming van fijne scheurnetwerken met hogere dichtheid en kleinere dieptes vergeleken met gepulste plasmabestraling met waterstof. Veranderingen van de thermische geleidbaarheid van het oppervlak en de bubbelgroeisnelheid werden onderzocht en vergeleken met de relevante blootstellingen in waterstof.

English summary

Tungsten is the selected material to be used in the ITER divertor due to its favorable thermal and physical properties. Particle flux densities and energies, and surface temperature will vary by several orders of magnitude along the divertor surface, with values in the range 10^{20}-10^{24} $m^{-2}s^{-1}$, 0.1-100 eV and 370-1370 K, respectively. Exposed to such conditions, tungsten may undergo erosion, cracking and other surface modifications affecting its thermal and mechanical properties. Another concern is the retention of implanted radioactive fuel atoms (tritium) in the material surface and their diffusion through the bulk. A considerable amount of studies have addressed retention and plasma-induced surface modifications, focusing mainly on the effect of ion energy, ion fluence and surface temperature while very little knowledge exists on the influence of the plasma flux. These results are largely scattered and occasionally bear a lack of consistency.

The aim of this thesis is to provide a coherent picture of the behavior of tungsten exposed to plasma conditions relevant for future fusion reactors. A systematic investigation assessing the impact of the plasma flux density and exposure temperature on surface modifications and hydrogen accumulation in tungsten was performed by means of experiments carried out in the linear plasma devices PSI-2 at Forschungszentrum Juelich, Pilot-PSI and Magnum-PSI at DIFFER, and PISCES-A at UCSD. The correlation between the particle flux density, exposure temperature, surface modifications and hydrogen retention in tungsten was investigated for different material microstructures. Three types of polycrystalline tungsten (thermally treated at 1273 and 2273 K) and single crystal tungsten samples (110 crystal orientation) were exposed to deuterium plasmas at surface temperatures of 530-1170 K to two different ranges of deuterium ion fluxes (low and high flux: $\sim 10^{22}$ and $\sim 10^{24}$ $m^{-2}s^{-1}$). All the exposures were performed at the same incident ion energy of 40 eV and particle fluence of $\sim 10^{26}$ m^{-2}. The exposed samples were analyzed post-mortem utilizing various surface imaging and analyses techniques (microscopy, thermal desorption spectroscopy and ion beam analysis).

Increasing the particle flux by two orders of magnitude caused blister formation at temperatures above 700 K for which blistering is usually absent under low-flux exposure conditions. Small blisters of several tens of nanometers and up to 1 μm of lateral size, were detected on the annealed polycrystalline and in single crystal tungsten samples, respectively. On the contrary, blisters were absent on the recrystallized samples except for the low flux and low temperature case where large blisters of about 10 μm and cavities along the grain boundaries appeared.

The total deuterium retention was measured by means of thermal desorption

spectroscopy (TDS). In the cases with low exposure temperatures, the retained fraction of deuterium was one to two orders of magnitude higher after exposure to the low flux compared to the high flux. On the contrary, an opposite tendency of the total deuterium retention at high exposure temperatures was observed. Hence, the maximum of the total deuterium retention was observed to occur at a higher temperature in the case of high incident particle flux ($\sim$850 K) compared to low flux exposures ($\sim$650 K). Overall, experimental results on deuterium retention were similar for all the investigated tungsten microstructures. Deuterium retention decreased at high temperatures and the maximal retention was lower for high flux exposures. However, due to the shift of the maximal retention to higher temperatures, the amount of deuterium retained at temperatures above 800 K was higher at high flux rather than at low flux, being still about one order of magnitude lower than the maximal retention at low flux.

The observations mentioned above concerning the trends of deuterium retention in tungsten can be attributed to the interplay of processes of damage creation, deuterium recycling and return back into plasma, and deuterium diffusion deeper into the bulk. For the same total fluence, a low flux exposure corresponds to a longer exposure times than a high flux exposure. Assuming the diffusion length scaling with the square root of time, a flux difference of a factor 100, yields a difference in diffusion depth of a factor 10. At low flux and high temperature, long exposure times allow for deuterium diffusion into the bulk, as well as for desorption at the plasma facing surface.

At high particle flux, larger concentration gradients of deuterium can be expected, leading potentially to stronger material damage and/or faster growth of deuterium filled bubbles or voids. At the same time, diffusion of deuterium deep into the material allows for deuterium trapping at intrinsic lattice defects, such as vacancies, dislocations and grain boundaries in case of polycrystalline samples. For typical grain sizes of about several μm to several tens of μm, short exposure times do not allow for efficient deuterium diffusion to grain boundaries, so it is then presumably trapped at intra-granular defects. Dislocation loops and grain boundaries can act as fast diffusion paths for deuterium, both towards the bulk and the surface. At the same time, kinks and jogs on dislocation lines and irregularity of grain boundaries can serve as nucleation sites for deuterium accumulation and growth of bubbles, e.g. by means of dislocation loop punching mechanism.

In order to get an insight into trapping energies of deuterium retained in tungsten after experiments described in this work, simulation of the measured thermal desorption spectra was performed using the rate equations approach implemented in the Coupled Reaction Diffusion Systems (CRDS) code. The TDS peaks could be reasonably well reproduced assuming either one trapping energy of 2.2 eV for recrystallized tungsten, two trapping energies of 1.9 eV and 2.0 eV for single crystal tungsten and 2.0 eV and 2.3 eV for other polycrystalline samples. From the physical point of view, these binding energies can be explained in the frame of void formation at nucleation sites on dislocation loops and grain boundaries. Deuterium is then trapped on the inner surfaces of such voids, which can be formed by loop punching or vacancy clustering. The energy barrier for deuterium to move

from the inner surface of the void into the material bulk should be than comparable with that for deuterium atoms on a free tungsten surface, which is estimated to be of about 2 eV in the literature.

In ITER, the divertor plasma will contain a fraction of helium ions as a product of the fusion reactions and therefore, further experimental investigations were performed to address the effect of He nano-bubble layers formed in the near surface region of tungsten under simultaneous D/He exposure. The presence of 5$\%$ He ions in deuterium plasma reduced the total deuterium retention on recrystallized tungsten and caused fuzz formation at elevated temperatures ($>$1000 K).

Exposures under ITER relevant steady state and transient heat and particle loads, simulating ITER ELMs in terms of amplitude, frequency (10 Hz) and energy densities (0.2-0.5 MJm^{-2}) were performed in the Pilot-PSI device in order to assess the effect of thermal shocks on the morphology changes of tungsten mentioned above. The steady state and transient particle and heat loads were obtained by using a pulsed plasma source and a high power laser (ms-pulse duration) in case when longer exposure time was required. Exposure to He plasma pulses caused the formation of fine cracking network on tungsten samples which occurred at a higher density and smaller depths compared to hydrogen pulsed plasma irradiation. The peak temperature, after exposure to H and He pulsed plasma at 850 K, increased with the same factor of 1.4 compared to the first plasma pulse, indicating a deterioration of the thermal conductivity.

1 Introduction

Nuclear fusion reactions occur when two light nuclei collide at high energy, overcome the repulsive Coulomb forces and become prone to strong interaction forces at short distances ($\sim 10^{-15}$ m). As a result, according to the mass and energy conservation laws, a new nuclei is formed, accompanied by a large amount of released energy. In terrestrial conditions, fusion reactions between hydrogen isotopes are easiest to achieve in terms of ignition temperature. Deuterium and tritium nuclei have the highest reaction cross-section when they collide at high energy, producing helium and an energetic neutron: $D + T = He(3.5MeV) + n(14.1MeV)$. The exploitation of fusion energy in a controlled way is considered as highly attractive since it could solve the problem of increasing energy demands on Earth [1]. Compared to other sources, nuclear fusion energy offers substantial advantages in terms of safety, environmental compatibility, long term utilization and abundance of fuel reserves.

In a fusion experiment, based either on a tokamak or stellarator concept, hot plasma is generated inside a toroidal vacuum chamber and is confined by a strong magnetic field to keep it distant from the wall. Despite the considerable success in terms of plasma physics understanding and technological progress, the energy gain factor Q=E_{out}/E_{in}, in present day tokamaks is lower than 60%, still far from being commercially profitable. The construction of a new full scale tokamak called ITER, aims at proving further scientific and technological feasibility of fusion and energy gain factor of ten. Superconducting coils and an electrical current running through the plasma will generate a strong magnetic field which is required to shape and confine the plasma. At the bottom of the vacuum vessel, a divertor will be

installed in order to remove helium ash and reduce the impurity content in the plasma. Massive amount of particles and heat loads will be exchanged and most of the plasma-material interaction processes will take place in this region (figure 1.1).

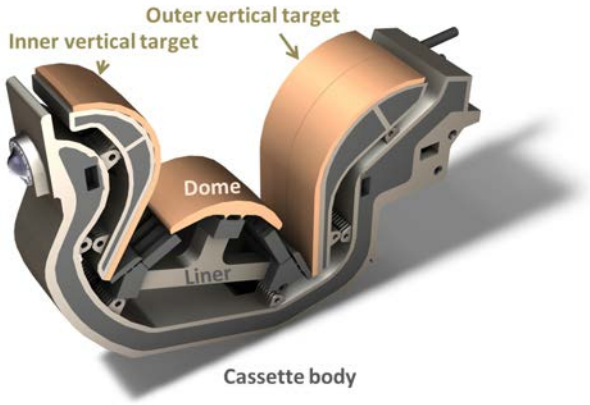

Figure 1.1: Schematic view of a remotely removable cassette of the ITER divertor [2]

A crucial issue for ITER will be to maintain a high purity core plasma and to ensure a long lifetime of the plasma facing components under extreme particle and heat loading conditions. Tungsten is the selected candidate to be used in ITER divertor as a first plasma facing material due to its favorable properties, high melting temperature and thermal conductivity, low gas inventory and low erosion yield [3, 4]. However, exposure to energetic particles such as hydrogen isotopes (D and T), He, and impurities, has an impact on gas retention and surface modifications (i.e. formation of blisters, bubbles, fuzz, cracking etc.) which may lead to an increase of the erosion yield, dust formation and deterioration of the thermal and mechanical properties of tungsten [5–7].

Numerous investigations have been performed, assessing the behavior of high-Z impurities in the plasma, erosion/deposition processes, melting, fuel retention and surface modifications. Tungsten was first used as a plasma facing material early in 1973 and 1976 at ORMAK (Oak Ridge, USA) and PLT (Princeton, USA) tokamaks [8]. At TEXTOR tokamak, tungsten was introduced as a test limiter [9]. The implementation of tungsten as a plasma facing material at ASDEX-Upgrade resulted on a good plasma performance, reduction of impurity deposition in the remote areas by a factor of ten and reduction of gas inventory [10]. Several remaining issues are being considered in the frame of ITER-like wall project at JET (Joint European Torus) where bulk tungsten tiles were introduced at the outer divertor and W-coated carbon fiber composites (CFC) were used in other areas of the divertor [11]. This project showed successful results concerning fuel retention as it

decreased by more than one order of magnitude compared to the C-wall operations. However, a decrease of divertor radiation was noticed due to the low radiation power of W compared to C. This issue might bring severe problems concerning the lifetime of target plates and thermo-mechanical fatigue [12]. Therefore, impurity seeding will be needed in the divertor region to increase the radiation power and consequently impede the localized overheating of the material [13].

Hydrogen isotopes diffusion and accumulation in tungsten and plasma induced surface modifications are still of major concern. Hydrogen inventory in the material can affect the plasma density, fueling efficiency and the accumulation of tritium above a certain level can raise safety issues. Experiments have demonstrated that the diffusion range of hydrogen ions in the material may reach up to several micrometers, even at incident energies below the sputtering threshold. After implantation, hydrogen can diffuse deeper in the metal and get trapped in the crystallographic defects. When its concentration in the implantation range is above the solubility limit and the diffusion to the bulk is low, overpressurized gas-filled cavities may form and cause material swelling due to plastic deformations of the lattice. These surface modifications are referred to as blisters, or bubbles when occurring in the bulk. Blister formation depends on the metal, the impinging ions and the metal-ion system properties.

Previous investigations have shown that the ion energy and fluence affect the penetration depth of particles and the vacancy concentration in the material [14]. Deuterium plasma exposure of polycrystalline tungsten at ion energy of 35-100 eV, ion fluence of about $10^{26}\ m^{-2}$ and particle flux $\leq 10^{22}\ m^{-2}s^{-1}$, revealed a large scattering of the data concerning lateral blister size (0.5-100 μm), shape and areal density. It was also shown that under these conditions, blisters are suppressed at exposure temperatures above $\sim$700 K [15–19]. When the ion fluence is increased, size and density of blisters increase up to several hundreds of micrometer until they burst due to the excessive gas pressure on the thin blister cap [20]. Blistering, and bursting of the blisters may degrade the thermal conductivity, cause melting and make tungsten prone to erosion and dust formation.

Investigations on the role of grain boundaries and intrinsic defects in the material such as dislocations and vacancies have confirmed that they can trap deuterium and act as centers for bubble nucleation [21–23]. Hydrogen isotope irradiation is not the only mechanism of defect formation in tungsten, other factors such as material mechanical and thermal pre-treatment, surface roughness, and material purity are also to be considered. Luo *et al.* [24] showed that the effective number of trapping sites was higher when a porous structure was formed after the manufacturing process, which led to a higher trapping rate of hydrogen in the material and increase of the total retention. The number of dislocations is considerably reduced when the material is recrystallized. Exposure of single crystal tungsten to hydrogen plasma resulted in a lower retention due to the accumulation of hydro-

gen in the near surface region which prevented deeper gas diffusion, unlike in the case of polycrystalline materials where the diffusion occurs mainly through the grain boundaries [25]. Another parameter that influences retention in tungsten is the presence of impurities which introduce additional defects and trapping sites into the lattice. Miyamoto *et al.* [26] found that blistering in tungsten depends also on the grain orientation, namely (111) orientation is more prone to blistering compared to other directions, and blisters appear in a large variety of shapes.

He effects on tungsten have to be considered in addition to hydrogen irradiation. Material damage may appear during the He campaign (non-active phase), when the ELM mitigation techniques will be carried out, as well as during the D-T phase of operation as He is a product of the fusion reactions. The material response to steady state and transient particle and heat loads during edge localized modes (ELMs) under ITER relevant conditions has to also be considered. ELMs, which are expected to occur at a frequency of several hundreds per discharge, must not increase the tungsten surface temperature beyond the melting and evaporation points [3, 27]. A combination of He bombardment effects such as nano-bubble layer formation with the transient heat loads can lower the transient damage threshold of the material and thermal shock properties.

The penetration depth of He into the material is large at high energies (nanometer range at eV energy to 1.7 μm at 1.3 MeV), therefore temperature and particle fluence have small impact on the material degradation regarding energetic ions. Fu *et al.* [14] reported material damage for 8 keV helium ions at room temperature and low particle fluence of $4 \cdot 10^{21}\ m^{-2}$. At low ion energy and surface temperature, the surface modifications are small due to the trapping of He particles in the near surface while at high surface temperature blisters start to form due to the He/vacancy diffusion into the bulk. Nishijima *et al.* [28] observed a lower limit in ion energy at about 12-18 eV influencing the bubble formation in tungsten after exposure to He plasma at surface temperature of 1850-2300 K and fluence $\sim 10^{26}\ He^{+}m^{-2}$. It was also shown that an ion energy lower than 30 eV, temperature higher than 1300 K and fluence $\sim 10^{26}\ He^{+}m^{-2}$ are required to create damages in the material such as blisters and voids [29]. He exposure at surface temperature of 1120-1320 K caused the formation of nanorods (filaments) on the surface being up to 1 μm long and 10-50 nm wide. The growth rate of the modified layer increased with exposure time and surface temperature [30, 31]. These structures which are referred to as tungsten "fuzz", generally occur at temperatures 1000-2000 K, ion energy E_{ion} $\geq$20 eV and fluence $\sim 10^{25}\ m^{-2}$ [32].

Plasma facing materials in ITER will have to perform under the impact of particle flux densities that vary by several orders of magnitude (10^{20}-$10^{24}\ m^{-2}s^{-1}$), surface temperature (370-1370 K) and ion energy (0.1-100 eV) [4]. Systematic experimental investigations addressing the particle flux impact are scarce while there is a large scattering of the data regarding temperature, ion energy and fluence

effects. The aim of this work is to systematically study the impact of particle flux, surface temperature, material microstructure, He impurities and transient heat and particle loads on plasma induced surface modifications and gas accumulation on tungsten in order to understand how such a material would perform in a fusion reactor. The impact of incident particle flux and exposure temperature on deuterium retention and on surface modifications in tungsten is the main focus of this thesis. To define the particle flux and surface temperature influence on tungsten, samples were exposed to plasma fluxes varying by two orders of magnitude (10^{22} and 10^{24} $m^{-2}s^{-1}$) at a surface temperature range 520-1170 K at the same ion fluence 10^{26} m^{-2} and energy 40 eV.

Material microstructure is another parameter to be investigated in terms of the dependence between the gas retention - surface morphology and particle flux - surface temperature. The aim is to separate the effects of grain boundaries and intrinsic crystallographic defects of the material in deuterium trapping and total inventory. For this reason, polycrystalline tungsten, single crystal and recrystallized samples were investigated. On one hand, single crystal tungsten has a low dislocation density and grain boundaries are not present. On the other hand, recrystallization at high temperatures decreases the dislocation density to negligible levels allowing identifying the role of grain boundaries in deuterium trapping and diffusion. Surface morphology changes and deuterium retention were studied on the recrystallized tungsten samples also when 5$\%$He impurities were present in deuterium plasma.

A last set of experiments was carried out addressing the effect of He nanobubble layer formed in the near surface region of tungsten under ITER relevant steady state and transient heat and particle loads, simulating ITER ELMs in terms of amplitude, frequency and flux densities [33]. The changes on the surface thermal conductivity and the bubble growth rate were investigated and compared with the relevant exposures in hydrogen. The same exposures were repeated in H as a reference for He damage threshold in terms of transient energy densities.

In this thesis, experiments were carried out in several linear plasma devices which fulfill the experimental requirements in terms of particle flux, fluence, ion energy, plasma species and sample temperature. Electron microscopy was used to investigate the surface modifications while D/He depth distribution and total inventory were studied with ion beam analysis and thermal desorption spectroscopy.

In chapter 2, a more extended overview on the theory of plasma-material interaction is given, with an emphasis on the hydrogen diffusion and plasma induced surface morphology. In the second part of the chapter, the conditions expected in ITER divertor are discussed. Detailed description of the sample preparation, experimental setup and analysis methods are given in chapter 3. Results on deuterium retention and surface modifications are included in chapter 4.

References

[1] B. L. Cohen. *The nuclear energy option*. Plenum Press, New York and London, 1990.

[2] http://www.iter.org/.

[3] A. Loarte. *Chapter 4: Power and particle control*. Nuclear Fusion, 47(S203S263), 2007.

[4] R. Pitts. *et al. A full tungsten divertor for ITER: Physics issues and design status*. Journal of Nuclear Materials, 438(S48S56), 2013.

[5] M. Baldwin. *et al. The effects of high fluence mixed-species (deuterium, helium, beryllium) plasma interactions with tungsten*. Journal of Nuclear Materials, 390391:886890, 2009.

[6] M. Miyamoto. *et al. Microscopic damage of tungsten exposed to deuterium-helium mixture plasma in PISCES and its impacts on retention property*. Journal of Nuclear Materials, 415:S657S660, 2011.

[7] M. Rieth. *et al. Recent progress in research on tungsten materials for nuclear fusion applications in Europe*. Journal of Nuclear Materials, 432:482500, 2013.

[8] G. Federici. *et al. Plasma-material interactions in current tokamaks and their implications for next step fusion reactors*. Nuclear Fusion, 41(12R), 2001.

[9] V. Philipps. *et al. Experiments with tungsten limiters in TEXTOR-94*. Journal of Nuclear Materials, 858-864:258–263, 1998.

[10] A. Kallenbach. *et al. Optimized tokamak power exhaust with double radiative feedback in ASDEX Upgrade*. Nuclear Fusion, 52:122003, 2012.

[11] S. Brezinsek. *et al. Overview of experimental preparation for the ITER-Like Wall at JET*. Journal of Nuclear Materials, 415(S936S942), 2011.

[12] A. Huber. *et al. Investigation of the impact of transient heat loads applied by laser irradiation on ITER-grade tungsten*. Journal of Nuclear Materials, 438:S139S147, 2013.

[13] A. Kallenbach. *Impurity seeding for tokamak power exhaust: from present devices via ITER to DEMO*. Plasma Physics and Controlled Fusion, 55(124041), 2013.

[14] Zhang Fu. *et al. Thermal desorption and surface modification of He+ implanted into tungsten*. Journal of Nuclear Materials, 329333:692–696, 2004.

[15] W. M. Shu. *et al. Recent findings on blistering and deuterium retention in tungsten exposed to high-fluence deuterium plasma*. Journal of Nuclear Materials, 386-388(C):356–359, 2009.

[16] H. Y. Xu. *et al. Deuterium-induced nanostructure formation on tungsten exposed to high-flux plasma*. Journal of Nuclear Materials, 2014.

[17] J. P. Sharpe. *et al. Retention behavior in tungsten and molybdenum exposed to high fluences of deuterium ions in TPE*. Journal of Nuclear Materials, 390391:709712, 2009.

[18] B. Tyburska. *Deuterium Retention in Carbonand Self-Implanted Tungsten*. PhD thesis, Marie Curie-Sklodowska University, Lublin, Poland, 2010.

[19] V. Alimov. *et al. Surface morphology and deuterium retention in tungsten exposed to low-energy, high flux pure and helium-seeded deuterium plasmas*. Physica Scripta, T138:014048, 2009.

[20] G. Luo. *et al. Incident energy dependence of blistering at tungsten irradiated by low energy high flux deuterium plasma beams*. Journal of Nuclear Materials, 347:111117, 2005.

[21] A. A. Haasz. *et al. Deuterium retention in single crystal tungsten*. Journal of Nuclear Materials, 290-293:85–88, 2001.

[22] O. Ogorodnikova. *et al. Pre-implantation and pre-annealing effects on deuterium retention in tungsten*. Journal of Nuclear Materials, 373:254–258, 2008.

[23] Hong-Bo Zhou. *et al. Investigating behaviours of hydrogen in a tungsten grain boundary by first principles: from dissolution and diffusion to a trapping mechanism*. Nuclear Fusion, 50:025016, 2010.

[24] G. Luo. *et al. Behavior of tungsten with exposure to deuterium plasmas*. Nuclear Instruments and Methods in Physics Research, 267(18):3041–3045, 2009.

[25] G. Pintsuk. *Tungsten as a Plasma-Facing Material*. Comprehensive Nuclear Materials Konings,R.J.M., Ed.; Elsevier: Amsterdam, The Netherland, page 551581, 2012.

[26] M. Miyamoto. *et al. Observations of suppressed retention and blistering for tungsten exposed to deuterium-helium mixture plasmas*. Nuclear Fusion, 49(6), 2009.

[27] G. Federici. *et al. Assessment of erosion of the ITER divertor targets during type I ELMs*. Plasma Physics and Controlled Fusion, 45:15231547, 2013.

[28] D. Nishijima. *et al. Incident ion energy dependence of bubble formation on tungsten surface with low energy and high flux helium plasma irradiation*. Journal of Nuclear Materials, 313316:97101, 2003.

[29] Y. Ishijima. *et al. Current status of ductile tungsten alloy development by mechanical alloying*. Journal of Nuclear Materials, 329-333:775–779, 2004.

[30] M. J. Baldwin and R. P. Doerner. *Helium induced nanoscopic morphology on tungsten under fusion relevant plasma conditions*. Nuclear Fusion, 48:035001 (5pp), 2008.

[31] G. De Temmerman. *et al. Nanostructuring of molybdenum and tungsten surfaces by low-energy helium ions*. Journal of Vacuum Science and Technology, A 30(041306), 2012.

[32] S. Kajita. *et al. Formation process of tungsten nanostructure by the exposure to helium plasma under fusion relevant plasma conditions*. Nuclear Fusion, 49(6pp):095005, 2009.

[33] R. Pitts. *Response of tungsten surfaces to helium plasma exposure under ITER relevant steady state and repetitive (sub-melting threshold) transient conditions. Technical Specifications*. https://user.iter.org/?uid=NEAK42, 2014.

2

Basic mechanisms of plasma-material interaction

Enormous amount of energetic particles will impinge on the reactor wall during the plasma operation. As a consequence, plasma facing components will degrade and part of the impinging plasma species will recycle in the wall material. The evaluation of hydrogen inventory in the reactor is crucial because it may affect the plasma density, fueling efficiency and particularly in ITER, the co-deposition or implantation of tritium in the vacuum chamber, must not exceed the total amount of 1 kg due to safety issues. Therefore, profound knowledge on the plasma parameters at the plasma edge and the impact on the plasma-material interaction is required. The first half of the chapter will consider in more details the hydrogen retention mechanisms in tungsten, trapping and diffusion processes, and modeling specifics of thermal desorption spectroscopy data. Temperature and plasma parameter profiles along the ITER divertor, as calculated from various codes, together with the argumentation and motivation for the parameter selection in the present experiments, will be included in the second half of the chapter. Moreover, an overview of previous investigations concerning the impact of plasma fluence and ion energy, surface temperature, material microstructure, plasma impurity and transients on hydrogen retention and plasma induced surface morphology will be discussed.

2.1 Hydrogen retention in tungsten

The experimental database concerning hydrogen retention in tungsten is rather extended as well as the scattering of the results. However, calculation of the hydrogen inventory which is expected to accumulate in a reactor wall must be based on a good understanding of the physical processes governing hydrogen diffusion, trapping mechanisms and its release from the material. The aim of this section is to provide an introduction to the fundamental processes involved and existing experimental data on diffusion, permeation and solubility, and trapping of hydrogen in tungsten.

In figure 2.1, the main processes involved in recycling of hydrogen at the wall of a fusion device, are schematically depicted. Hydrogen atoms may get adsorbed in surface and sub-surface layers and subsequently get trapped in vacancies, grain boundaries, dislocations or interstitial sites.

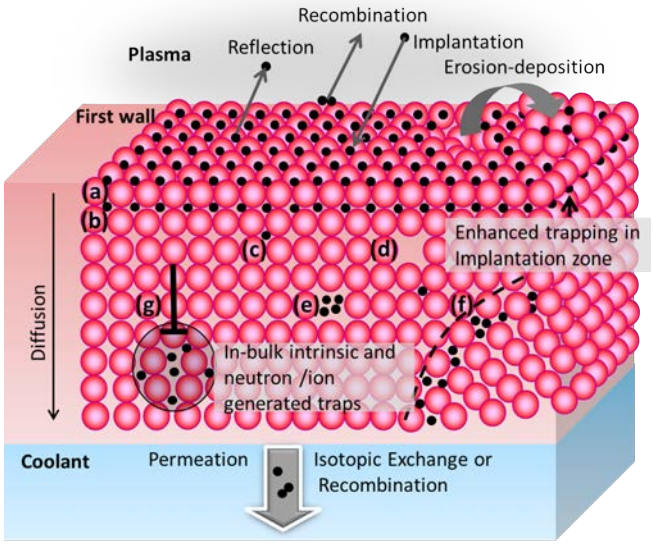

Figure 2.1: Main processes involved in retention and recycling of hydrogen at the wall of a fusion reactor. Hydrogen atom sites in the lattice: (a) Surface adsorption, (b) sub-surface layers adsorption, (c) Interstitial, (e, d) Vacancies, (f) Grain boundary, (g) Dislocation

The exhaust of high heat and particle fluxes to the plasma wetted areas erodes the material via sputtering or may cause material loss due to sublimation or melting. A fraction of the eroded particles, after being ejected from the wall, may become ionized, enter the plasma and return back to the wall along the magnetic field lines, enabling the recycling process. In general, the particle bombardment

process may bring along various scenarios [1]. The impinging particles can be backscattered after the collision to the surface or implanted near the surface and released as thermal particles (usually at relatively low surface binding energy). If their energy is relatively high, they may implant deeper in the material and get released at a later time. Alternatively, they can get either deposited on the surface or eroded.

Physical sputtering occurs when energetic projectiles bombard the target and eject atoms by momentum transfer. The impinging particles transfer a fraction of their energy to the lattice, causing a collision cascade. If the recoil energy is higher than the surface binding energy, atoms may get ejected from the solid. The main parameter characterizing the physical sputtering is the sputtering yield which represents the number of sputtered particles per incident projectile. The process employs a "threshold energy" above which, sputtering is feasible: $E_{th} = E_s/\gamma(1-\gamma)$. E_s is the surface binding energy and γ is the fraction of energy transferred to the lattice after the collision. The factor γ depends on the mass ratio of the target m_2 and projectile m_1 as: $\gamma = 4m_1m_2/(m_1+m_2)^2$ [1]. It is evident that the sputtering yield is related to the mass ratio of the target and projectile; it reaches its maximum for alike particle collisions for which the energy transfer is most efficient. For light impinging elements where the mass ratio of target atom to projectile ion is very high, the energy transfer is less efficient, leading to a reflection of the particle from the surface. Hydrogen sputtering of tungsten has a high threshold energy due to the large mass difference ($\sim$1 u vs. $\sim$184 u). The γ factor calculated for hydrogen and its isotopes, yields: $\gamma_{(H\rightarrow W)} = 0.022$, $\gamma_{(D\rightarrow W)} = 0.043$, $\gamma_{(T\rightarrow W)} = 0.063$. Hence, the sputtering threshold energy of i.e deuterium on tungsten is about 200 eV up to keV energy, well above the energy range expected in the divertor region [1].

A fraction of the incident particles will be reflected from the surface back into the plasma depending on their energy and type of material. The fraction of particles which enter the implantation zone can get trapped in the crystallographic defects which are either intrinsic or generated from the neutron or other plasma species irradiation. Once the solubility limit is reached, trapped particles may either recombine and leave the surface or diffuse further in the bulk material, fill the existing traps and even diffuse deeper to the cooling structure. Hydrogen will reach either of the surfaces and recombine if the temperature or the recombination rate coefficient are sufficiently high.

Adsorption (on-surface) and *absorption* (in-bulk) are the principal states of hydrogen in the solid matter. When the diatomic H_2 molecule gets in contact with the surface of a transition metal, it has the tendency to dissociate and create strong atomic-surface interaction. Energetically, this occurs when the binding energy of atomic hydrogen with the surface is higher than the dissociation heat of the molecule. Adsorption is strongly affected by the presence of impurities and

adatoms (loosely bound atoms to the metal surface) on the surface as they may alter the adsorption conditions or interfere with the dissociation sites [2].

Hydrogen diffuses from the implantation region to the bulk and occupies different sites in the lattice, typically at the grain boundaries, vacancies, interstitial sites and dislocations, as depicted schematically in figure 2.1. In tungsten, which has a body-centered cubic lattice (bcc), interstitial hydrogen favors the tetrahedric sites with a jumping activation energy 0.4 eV between the two sites [3].

In figure 2.2, a qualitative diagram of potential energy of hydrogen transport in tungsten is given, which is an endothermic material for hydrogen intake. From this diagram can be seen that once the H_2 molecule dissociates at the surface, it goes through an energy barrier E_{S-B} to enter the bulk material. Energetic particles however, don't account on the implantation profile [4]. Thermal diffusion of "free" hydrogen in tungsten is often described by the relation: $D \sim 10^{-7} exp(-E_{diff}/k_B T)$ $(m^2 s^{-1})$ where E_{diff} is the diffusion activation energy and T is the temperature. Traps are generated by lattice imperfections, impurities, grain boundaries and hydrogen atoms can get released from such traps if they overcome the E_{tr} energy barrier (de-trapping rate: $\gamma_{dt} \sim 10^{13} exp(-E_{tr}/k_B T)$ (s^{-1})).

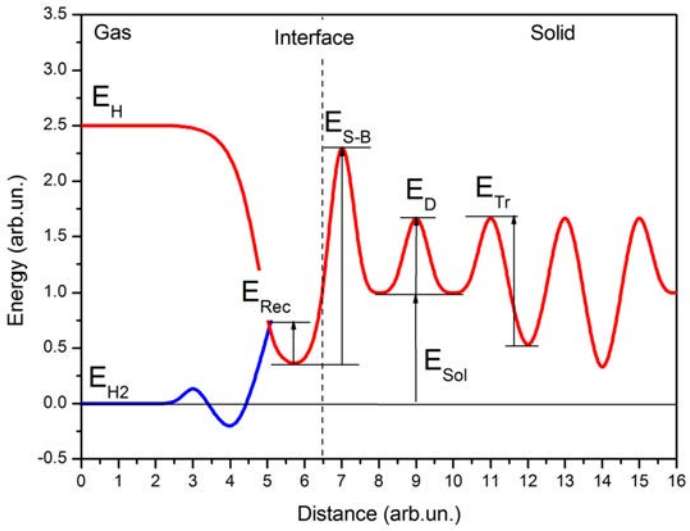

Figure 2.2: Qualitative potential energy diagram of hydrogen transport in tungsten [4]

Hydrogen leaves the tungsten surface after recombination into H_2 molecule. Associative (recombinative) desorption rate of hydrogen from tungsten at the surface is defined from the concentration of hydrogen at the near surface region $[H]_s$

and the recombination rate coefficient K_{rec}:

$$\Gamma_{des} = [H]_s^2 K_{rec}(atoms \cdot m^{-2}s^{-1}) \tag{2.1}$$

Where $K_{rec} \sim 10^{-3}exp(-2E_{rec}/k_BT)$. E_{rec} is the recombination energy barrier and T is the surface temperature. Recombination rate decreases when solubility and the amount of the impurities in the material is high. However, under fusion relevant conditions where high temperature and fluxes are expected, trapping-detrapping rate and diffusion to the surface are processes which will have the largest influence on the release rate, while recombination at the surface might have a negligible effect [4].

2.1.1 Hydrogen mobility

Hydrogen diffuses very fast in tungsten and it desorbs even at room temperature from the metal. Diffusion rate coefficients have been derived from various experiments and modeling but they are largely scattered and the most reliable to be used are the Frauenfelder's results [3]. He measured the desorption rate of hydrogen from loaded tungsten wires at temperatures 1200-2400 K and proposed the diffusion coefficient: $D = 4.1 \cdot 10^{-7}exp(-0.39eV/k_BT)\ m^2s^{-1}$. At such high temperature, diffusion is not affected by trapping and surface recombination is insignificant. Causey [5] recommends using the activation energy -0.39 eV and pre-exponential factor $4.1 \cdot 10^{-7}\ m^2s^{-1}$ [3] for the diffusion coefficient. However, density functional theory (DFT) calculations suggest faster diffusion with an activation energy of 0.2 eV and pre-exponential factor $1.9 \cdot 10^{-7}\ m^2s^{-1}$ [6].

The extrapolation of Frauenfelder's data have been used at lower temperatures. In his review on hydrogen retention in tungsten, Tanabe [7] adds the recent results on tritium tracer technique from Ikeda *et al.* [8] which fall on Frauenfelder's extrapolation to lower temperatures (see figure 2.3). They suggested an upper limit for the diffusion, relevant in the temperature range 250-2500 K: $D = (3.8 \pm 0.4) \cdot 10^{-7}exp(-0.4 \pm 0.015eV/k_BT)\ m^2s^{-1}$. The fact that hydrogen diffuses out of tungsten at any temperature, starting from the room temperature, indicates that the experimental data on tungsten mobility could be strongly affected by the sample treatment and time lag between the loading and desorption processes.

In figure 2.4, permeation rate coefficients for hydrogen in tungsten, are plotted ([7] and references herein). The suggested activation energy for permeation from Ikeda *et al.* [8], derived from the tritium tracer technique, is 65 kJ/mol ($\sim$0.67 eV) and the pre-exponential factor is $(1.21 \pm 0.24) \cdot 10^{-5}\ molm^{-1}s^{-1}$. This value is in a good agreement with Frauenfelder's data when extrapolated to higher temperatures. Frauenfelder's data for permeation suggest an activation energy of 1-1.4 eV in the high temperature range but it is not relevant when extrapolated to lower temperatures where trapping and surface effects become dominant.

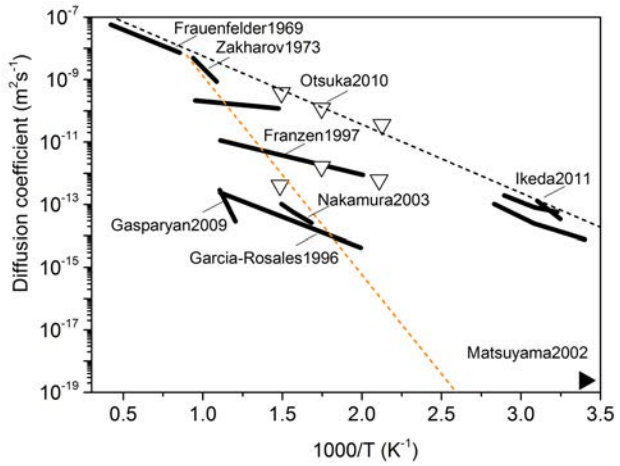

Figure 2.3: Diffusion coefficients of hydrogen in tungsten from modeling and experiments [5, 7]

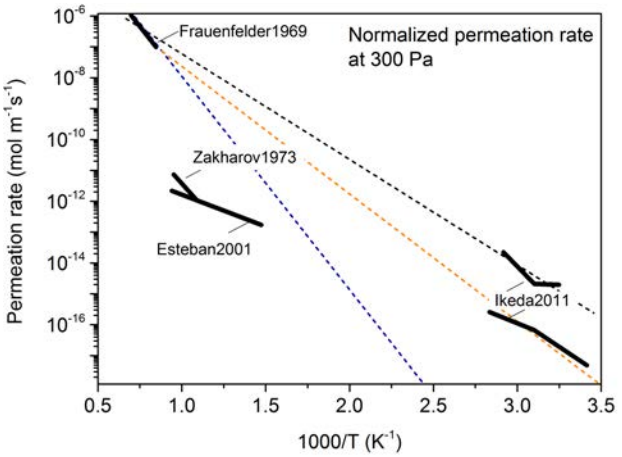

Figure 2.4: Normalized permeation coefficients of hydrogen in tungsten at 300 Pa [7]

The concentration of hydrogen near the surface is determined by the solubility S and pressure p of the gas: $[H] = S \cdot p^{0.5}$ (Sievert's law). When permeability measurements are done at steady state, permeability is given as a product of diffusivity and solubility: $P = D \cdot S$ [7]. Hydrogen solution in an ideal tungsten lattice has a rather low solubility ($10^{-8} - 10^{-6} at.\%$) which indicates the fact that retention in tungsten is governed by the trapping in defects [3]. The low values of solubility make it rather difficult to measure experimentally therefore, the existing database is scarce. Frauenfelder measured hydrogen solubility in his

tungsten samples in the temperature range 1100-2400 K and suggested the relation: $S = 9 \cdot 10^{-3} exp(-1.04/k_B T)\ H/Watm^{0.5}$ [3]. Solubility is important to be investigated in terms of blister/bubble formation and in estimating the recombination rate coefficient. Recombination rate of hydrogen at the surface is significant at relatively low temperatures. Causey [5] recommends using the recombination rate derived from steady state permeation studies done by Anderl *et al.* [9]: $K_{rec} = 3.2 \cdot 10^{-15} exp(-1.16/k_B T)\ (m^4 s^{-1})$. He fitted the permeation data for high purity tungsten loaded with 3 keV D_3^+ ions at 690-825 K.

2.1.2 Trapping and surface effects

Trapping of hydrogen in tungsten above room temperature occurs generally at the crystallographic defects of the metal such as grain boundaries, dislocations, vacancies and vacancy clusters. These defects can be intrinsically formed during the material production or generated by the impact of energetic incident particles and impurities. Natural intrinsic trap densities in bulk tungsten is about $10^{-4} at.\%$, not counting for the generated traps from plasma species, impurities and fast neutrons $D(T,n)\alpha$ [4].

The calculation of the trap activation energy is generally done by fitting the thermal desorption spectroscopy data (see next section). Detailed description of these investigations is given in recent hydrogen retention publications [4, 5, 7], where it was observed a rather broad range of release temperature distribution, occurring in a range of 350-1100 K at 15 different peak temperatures. The release temperature however, depends on the desorption conditions, sample preparation and level of impurities, loading conditions etc. Modeling of the thermal desorption spectroscopy data for deuterium loaded polycrystalline tungsten from Ogorodnikova [10] yield an activation energy of 0.85 eV and 1.45 eV which was associated to the lower energy traps such as dislocations, impurities, grain boundaries and higher energy traps such as ion-induced defects and voids.

The amount of intrinsic traps can be decreased if the metal is thermally treated. When tungsten is recrystallized, grains become larger and trapping in the grain boundaries is lower. However, a straightforward comparison can be done by studying the deuterium retention in a polycrystalline and single crystal tungsten. From previous investigations it has been observed that deuterium diffuses deeper in the polycrystalline material and above 400 K it is trapped in the bulk traps, reaching a concentration of about $\sim 10^{-4}$ to $\sim 3 \cdot 10^{-3}\ at.\%$ in single crystal and polycrystalline tungsten respectively. The authors attribute the difference to the presence of the grain boundaries [4, 11, 12].

The pre-irradiation of single crystal tungsten with 2-10 keV He ions at 295 K and 820 K led to hydrogen saturation in the metal. From the study, it was inferred that the presence of surface modifications and micro-structural changes increased

the dissociative adsorption of hydrogen in the near surface region, consequently leading to hydrogen trapping in the implantation zone [13]. Meanwhile, a percentage of 2.35 carbon in the hydrogen beam led to a carbide layer formation on the tungsten surface which prevented the blister formation [14]. Alimov noticed a shift from 500 K to 600 K for the maximum of total deuterium retention in polycrystalline tungsten during carbon-seeded deuterium plasma exposure. The formation of tungsten carbide on the surface might have served as a barrier for the outward diffusion of hydrogen, thus increasing the total retention [15].

2.1.3 Modeling of the thermal desorption spectroscopy data

Thermal desorption spectroscopy (TDS) is a commonly used method to evaluate the total gas retention in a metal, as well as desorption activation energies. Typically, the sample is heated in vacuum at a certain temperature ramp rate, and the released gas is detected by a mass-spectrometer. Before gas atoms are detected by the mass-spectrometer, they must overcome the de-trapping energy barrier in the metal, diffuse to the surface and possibly get re-trapped on the way out, and finally leave the surface after recombining to molecules. The measured desorption flux is usually plotted either as a function of time or as a function of the sample temperature. The shape, position and number of peaks of such a TDS profile depend on the interplay of all above-listed process and only in rare cases can be deduced, based solely on the knowledge of the dominant process.

De-trapping of hydrogen atoms from trapping sites in a metal is a thermally activated process, so the de-trapping rate is typically described by an Arrhenius type equation, e.g. as a product of a temperature independent pre-exponential factor, often referred as the attempt frequency, and the Boltzmann factor $exp(-E_a/k_BT)$, with an activation energy E_a. In the publication from A.M. de Jong and J.W. Niemantsverdriet [16] it is demonstrated that the derivation of the activation energy and the pre-exponential factor based on the analysis of the peak temperature, peak width and shape for a single TDS profile, performs poorly. The reason for this is the release of hydrogen from the depth of the material and its diffusion and re-trapping during desorption. More reliable data on the activation energy and pre-exponential factor may be derived from the shift of the TDS peak temperature, when several desorption measurements on equal samples are performed at different heating rates ($T(t) = T_0 + \beta t$). Considering a linear heating ramp with T_{max} at maximal desorption and the Arrhenius relation for the desorption flux, implying that desorption is limited by de-trapping, yields: $ln(\beta/T_{max}^2) = ln(k_BA/E_a) - E_a/k_BT_{max}$. E_a is the activation energy and A is the pre-exponential factor. The activation energy would therefore be the slope of the graph β/T_{max}^2 plotted as a function of $1/T_{max}$ in a semi-log scale [17]. Also in this case, the applicability of the method is limited as it depends on the surface

recombination and re-trapping processes [18]. The relevance of such measurements is, however, the generation of additional data for modeling and reduction of the number of the free parameters.

In order to simulate the implantation and desorption processes, diffusion and trapping of hydrogen in tungsten are usually described with a set of 1D rate equations [19]. One partial differential equation that describes the time evolution of the solute hydrogen concentration in tungsten is given in 2.2, as a combination of a diffusion term, an implantation source and trapping-detrapping reactions:

$$\frac{\partial \rho_{sol}(x,t)}{\partial t} = \frac{\partial}{\partial x}\left(D(T)\frac{\partial \rho_{sol}(x,t)}{\partial x}\right) - \sum_{i=1}^{N}\frac{\partial \rho_i^{trapped}(x,t)}{\partial t} + \Gamma_{source}(x,t) \tag{2.2}$$

The diffusion coefficient is given by $D(T) = D_0 exp(-E_{diff}/k_B T)\ (m^2 s^{-1})$, where E_{diff} is the diffusion activation energy. ρ_{sol} is the mobile deuterium concentration, $\rho_i^{trapped}$ is the concentration of trapped deuterium in traps of type i, and N is the total number of traps. $\Gamma_{source}(x,t)\ (s^{-1})$ is the hydrogen implantation source, which has to be corrected due to the reflection of incident particles. The reflection coefficient of 40 eV incident deuterium ions is about 66% according to SDTrimSP calculations, which are based on the binary collisions approximation [20].

$$\frac{\partial \rho_i^{trapped}(x,t)}{\partial t} = \alpha(T)\rho_{sol}(x,t)\left(\xi_i(x,t) - \rho_i^{trapped}(x,t)\right) - \gamma_i(T)\rho_i^{trapped}(x,t) \tag{2.3}$$

In equation 2.3, the time evolution of the trapped hydrogen density is given as a combination of processes of jumping of mobile hydrogen into unoccupied traps (first term) and out of occupied traps back into the solute state (second term). The trapping rate is given by: $\alpha(T) = D(T)/a^2\delta$, where a is the lattice parameter and δ is the atomic density of the material. This expression assumes the trapping rate to be governed by diffusion (no extra trapping barrier). The detrapping rate of hydrogen, as already mentioned, depends on the material temperature with $\gamma_i(T) = \nu_i^{detrap} exp(-E_T/k_B T)$. ν_i^{detrap} being the de-trapping frequency. $\xi_i(x,t)$ is the trap concentration profile for type i traps. The boundary conditions for this problem are set such that the surface recombination flux at both surfaces of the sample (front and back side) is the same as the diffusion flux from the bulk:

$$\left(K_r\rho^2 = D\frac{\partial \rho}{\partial x}\right)_{x=0} \quad \text{and} \quad \left(K_r\rho^2 = -D\frac{\partial \rho}{\partial x}\right)_{x=d} \tag{2.4}$$

$K_r\ (m^4 s^{-1})$ is the recombination coefficient and d is the sample thickness. The hydrogen solute partial differential equation and ordinary differential equa-

tions that describe the trapping and de-trapping processes, are implemented in the TMAP code [21]. TMAP deals with three different traps and up to 10 diffusing elements, which are generally reduced to 3 (D, T and H) for fusion applications. The trapping of diffusion species is determined by their mobility and the implemented spatial distribution of traps. A detailed description of the TMAP code is given in reference [21]. The main difficulty in modeling the hydrogen implantation relies on the fact that even at low incident ion energies, deuterium can create surface modifications such as bubbles and blisters during the plasma exposure. TMAP cannot deal with the dynamical formation, migration and evolution of these defects. Therefore, modeling of the implantation stage bears uncertainties.

Similar rate equations approach is implemented in the Coupled Reaction Diffusion Systems (CRDS) code, which describes the diffusion of all species, including traps via partial differential equations, coupling the local densities of all present species by formation and dissociation reactions (second term in equation 2.5). The local reactions are given in the form of activated Arrhenius terms. The CRDS code is written in Mathematica® with 1D and 2D implementations, which numerically solve the system of equations described above. Potentially, it is possible to take into consideration the dynamics of defect formation, their migration and evolution. However, in order to solve the equations, initial assumptions must be made, related especially to trap sites densities, formation and dissociation reactions to be included, trapping and de-trapping activation energies and jump frequencies.

$$\frac{\partial \rho_i(x,t)}{\partial t} = \frac{\partial}{\partial x}\left(D_i(T)\frac{\partial \rho_i(x,t)}{\partial x}\right) + \sum_{j,k=1}^{N} \gamma_{j,k}(T(t))\rho_j^a(x,t)\rho_k^b(x,t) + \Gamma_s(x,t) \tag{2.5}$$

Interpretation of TDS profiles in terms of shape, peak position and number of peaks is dependent on several factors such as the de-trapping energy and frequency, temperature ramp, trap concentration and depth distribution, diffusion coefficient, surface recombination, desorption from the backside of the sample, and re-trapping. Many parameters usually bear significant uncertainties, therefore interpretation of TDS spectra based only on measured desorption profiles is ambiguous and prone to simple fitting to one or another observation without consistent explanation of the mechanisms involved.

Multiple peaks may indicate presence of trap sites with different de-trapping energies. However, multiple peaks also may appear either due to a deeper diffusion range in the bulk with a large density of trapped hydrogen near the surface and lower density over a thicker bulk layer, or it can result from the presence of empty traps that may cause deuterium to be re-trapped several times before it desorbs, also on the way into the deeper bulk [22, 23]. Increasing the trapping energy, the TDS peak shifts to higher temperatures and becomes broader. A similar effect is attributed to decreasing the de-trapping frequency, as plotted in figure 2.5. The

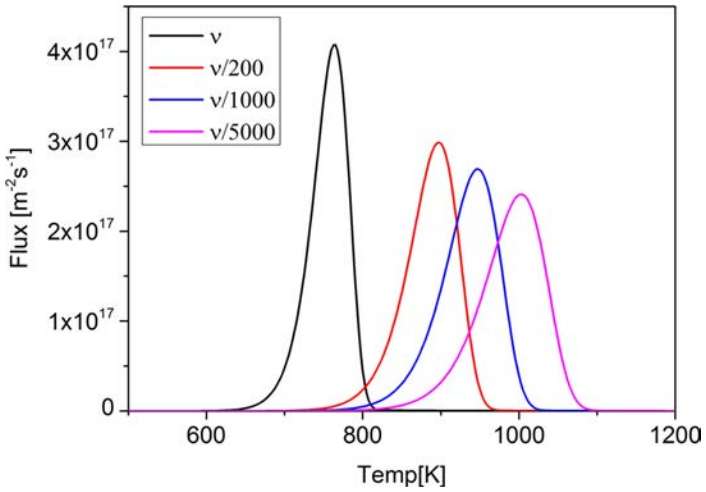

Figure 2.5: TDS simulation (without implantation) for a trapping energy of 2.2 eV without re-trapping ($\nu_{trap} = 0$). De-trapping frequency ($\nu_{de-trap}$) is varied for several cases

shape of the TDS profiles may change due to the assumptions related to trapping and de-trapping frequencies (pre-exponential factors). If no re-trapping is assumed during the desorption ($\nu_{trap} = 0$), the simulated TDS profiles become narrower. Considering all the factors and the uncertainties concerning trap formation and evolution during implantation, only desorption phase was simulated in the present work.

2.2 Mechanisms for blister formation

A critical gas concentration at the near surface region of the metal should be reached in order to initiate the blister formation. Blistering depends particularly on the target (surface temperature and roughness, material composition, microstructure, mechanical properties), incident ion parameters (ion species, flux, fluence, incidence angle, energy) and gas-metal system (diffusivity, solubility, phase state).

Particle flux density impact on the surface modifications is especially significant in the analysis of the present work. It influences the development of structures on the metal surface in two ways; Firstly, higher particle flux density irradiation may cause a temperature rise in the implanted layer due to the lack of efficiency in heat dissipation. Secondly, particle flux density and diffusion of the gas to the bulk and to the surface where it gets recombined, determines the amount of gas in the implantation zone. With increasing flux, for the same particle fluence, the concentration of deuterium in the implantation zone is higher. In case the concentration grows beyond the solubility limit, overpressurized bubbles may form which can

lead to blistering and additional defect formation [24]. *Das and Kaminsky* [25] observed the increase of the blister density in V and Nb after He irradiation at 1173 K. In addition, flaking of the blister cap was detected after He exposure of Nb at temperature above 1300 K due to the worsening of the thermal conductivity. Hydrogen irradiation of Mo caused a decrease of the critical fluence for blister formation with increasing particle flux density.

Blistering occurs in metals with low diffusivity of the gas and solubility far beyond the limit. Current models on blister formation are based on the gas filled cavity pressure on the metal and lateral compressive stresses due to the gas implantation which leads to material swelling. The first phase of blister formation comprises the development of a loosely-bound layer to the bulk and continues with the deformation of this layer. The formation of the loosely-bound layer (*Initial Phase*) can in principle explain the experimental observations concerning the blister formation dependence on the critical value of the particle flux, fluence, energy and surface temperature. While the deformation of this layer (*Surface Deformation*) holds for the observed results on various blister size and shape, crack formation, flakes etc [24].

There are several models which attempt to describe the mechanisms involved in bubble growth, as an initial phase of blister formation. The mechanism of bubble growth is generally associated to the conversion of single vacancies populated by a certain number of gas atoms, to vacancy clusters filled with gas. The *Thermal Equilibrium* model assumes the equilibrium pressure gas in the bubble to be proportional to the surface free energy. Small bubbles coalesce together by conserving the total bubble surface area. This model holds for high temperatures where the thermal vacancies are present in the metal. At lower temperatures, bubble growth can be attributed to the presence of thermal vacancies formed due to the damaging irradiation or *Interstitial Loop Punching* mechanism. Punching of the interstitial loops happens due to the gas filled cavity pressure (see figure 2.6).

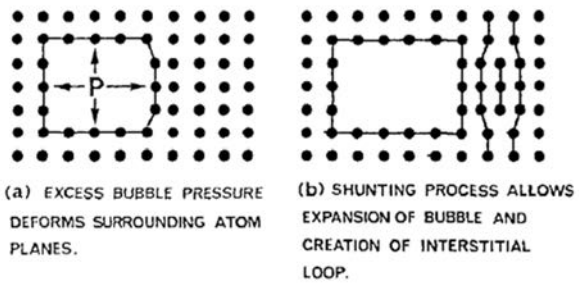

Figure 2.6: Overpressurized bubble growth model based on interstitial loops punching from a gas-filled cavity ([24] and references herein)

In addition to the *loop punching model*, *inter-bubble fracture model* refers to the *Initial Phase* of blister formation. This model was revised by *Evans* [26] who tried to explain the experimentally observed disagreement between the blister-cover thickness and ion implantation range in the metal, the latter being smaller than the former. According to *Evans*, the tensile stress exerted perpendicularly on the bubble-free plan, initiates a crack (2.7. b). Subsequently, the small over-pressurized bubbles in the metal, join (2.7. c) and expand the crack (2.7. d) which evolves to a blister (2.7. f). The tensile stress occurs typically due to the high pressure of the bubbles.

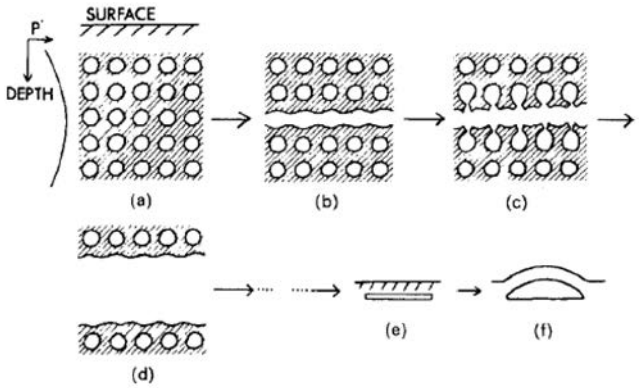

Figure 2.7: Stages of the inter-bubble fracture model: (a) an amount of over-pressurized bubbles with the same radii, (b) crack formation due to the tensile stress exerted perpendicular to the bubble-free plan, (c) adjacent bubbles join the crack, (d) which expands further, (e) forms a lenticular crack (f) and evolves into a blister [24]

The tensile stress applied on the interconnecting layer is caused by the bubble pressure, size and growth mechanism but it is not necessarily related to the ion implantation range. *Evans* considered the bubble coalescence and loop punching mechanisms as competitive for bubble growth. In later publications, the loop punching mechanism solely was considered on the bubble growth which resulted on the fracture occurring close to the ion implantation range [24].

After the detached layer is formed in the material, the next phase leading to the blister formation is the *Surface Deformation*, mainly due to the lateral compressive stresses and gas pressure applied on this layer. *Primak and Luthra* [27] proposed the *Spherical shell model* which was based on the similarity of a blister to a spherical shell with a flat bottom. The large expansion of the blister cap was attributed to the plastic deformation of the material.

2.3 Plasma loading conditions expected in the ITER divertor

In ITER, the divertor plasma will contain large amounts of hydrogen isotopes (D, T), He and impurities with flux densities and energies, varying by several orders of magnitude along the divertor surface. Exposed to such conditions, tungsten may undergo erosion, cracking and other surface modifications affecting its thermal and mechanical properties. Another concern is the retention of implanted radioactive fuel atoms (tritium) in the material surface and their diffusion through the bulk. Therefore, detailed knowledge on the plasma parameters at the plasma edge and the impact on the plasma-material interaction is required.

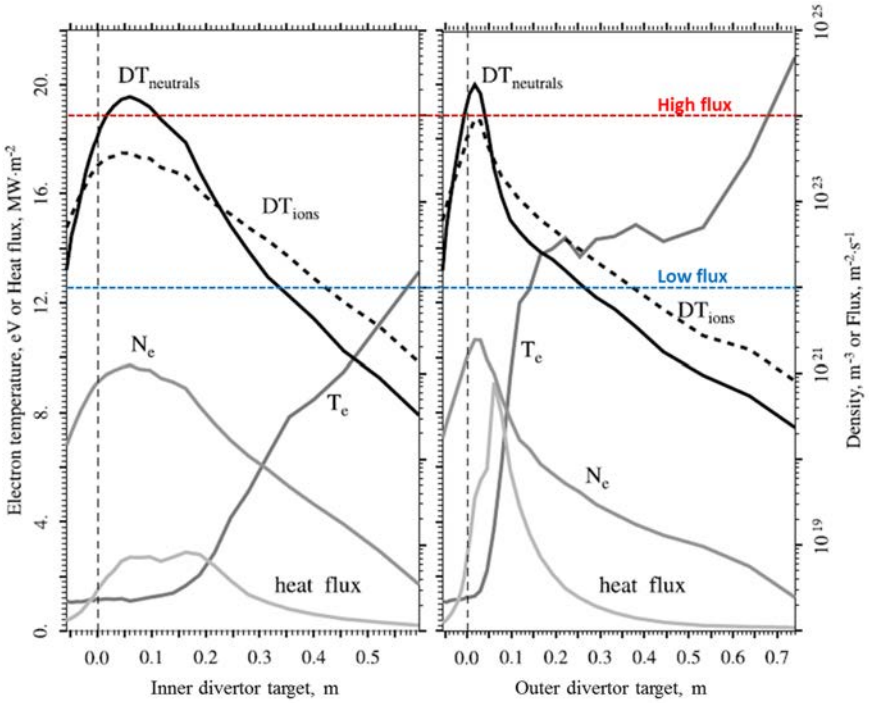

Figure 2.8: Plasma profile (temperature, density, particle and heat flux) along the inner and outer ITER divertor for a semi-detached plasma scenario (highly radiative divertor operation [28]). Low and high flux notations represent the deuterium particle fluxes selected to be studied in the experiments

Plasma parameters as modeled with B2-EIRENE code on the ITER divertor, where the particle and heat fluxes are expected to be critical for the plasma facing components, are plotted in figure 2.8. Electron temperature, density, particle and heat fluxes along the inner and outer ITER divertor are simulated for a semi-

detached plasma scenario with 100 MW power entering the scrape-of-layer [28]. As seen from the graph, the particle fluxes will vary by several orders of magnitude, reaching up to $\sim 10^{24}\ m^{-2}s^{-1}$. The question raised, after a large amount of investigations on the deuterium retention, is related to its impact on the particle flux and temperature. It was found that the total deuterium retention has a maximum in the temperature range 400-600 K at fluxes above $\sim 10^{21}\ m^{-2}s^{-1}$ [29] (see figure 2.11). The aim of the present work is to distinguish the role of the particle flux on deuterium retention and surface morphology on tungsten when the fluence is kept constant. In the figure 2.8, low and high flux notations represent the deuterium particle fluxes which are selected to be studied in the experiments, namely 10^{21} and $10^{24}\ m^{-2}s^{-1}$. The selected ion fluence to be studied is $10^{26}\ m^{-2}$ due to the large existing database and possibility of comparing the results and the relevance to the fluence accumulated after one ITER plasma discharge. Another reason is the feasibility to achieve this fluence in a linear plasma device from the technical point of view.

Simulations based on the thermo-hydraulic calculations (RACLETTE code) for He and DT plasma operations [30], predict a temperature range 600-1000 K for major part of the profiles along the outer divertor, coinciding with the temperature of bubble layer formation. In figure 2.9 the surface temperature variation along the outer target at ITER divertor during He and DT phase of operation, is plotted. In addition to the surface modifications, also deuterium retention has a strong dependence on the exposure temperature therefore the selected temperature range in the present experiments is 500-1170 K.

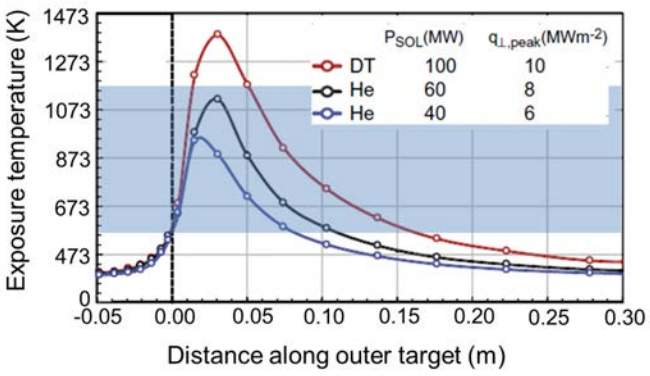

Figure 2.9: Surface temperature variation along the outer target at ITER during He and DT phase of operation [30]

2.4 Plasma loading impact on surface modifications and retention

2.4.1 Ion fluence and surface temperature

A broad database has been already established, addressing mainly the ion fluence impact on the total deuterium retention and depth distribution in the material, investigated with thermal desorption spectroscopy and ion beam analysis methods [4, 31–33]. In figure 2.10, deuterium retention data are taken from several experiments performed at ion fluence lower than $10^{27}\ m^{-2}$ and surface temperature about 500 K on polycrystalline tungsten samples [29]. The ion energy was varied in a broad range of 38-500 eV and the flux in these experiments was kept below $10^{22}\ m^{-2}s^{-1}$. These data are taken from laboratory and tokamak experiments. Their distribution indicates a saturation of the total deuterium retention with fluence. The general dependence of the deuterium retention can be described as its variation with fluence to the power of 0.5-0.7.

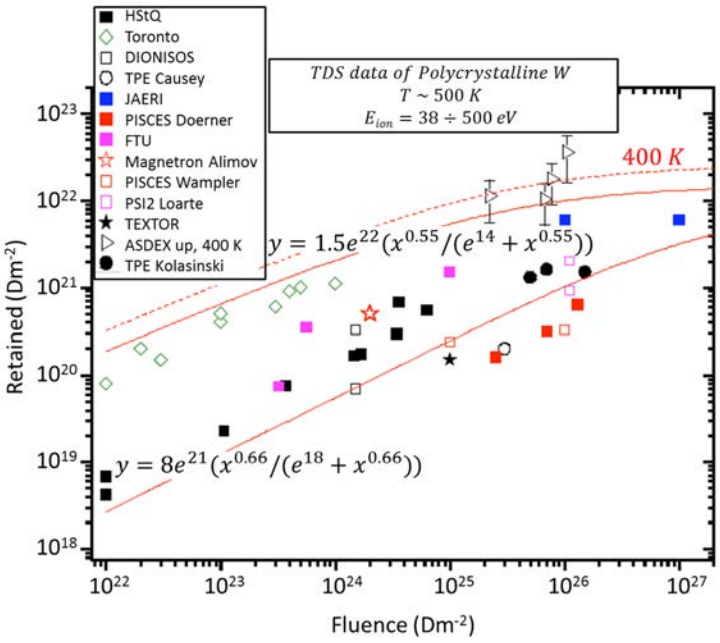

Figure 2.10: Total deuterium retention in polycrystalline tungsten at various ion fluences [29]

However, recent experiments performed at PISCES-B, show no clear saturation when fluence is increased up to $\sim 10^{28}\ m^{-2}$ at higher particle flux larger than $10^{23}\ m^{-2}s^{-1}$ (at 643 K) [34]. Instead, the total retention scaled with time to the

power 0.5 (diffusion scaling). The lack of saturation could be an effect of the higher flux which imposes less time to reach the nominal fluence. Therefore, the generation of additional defects during high flux exposure and non-saturation of existing ones, leads to higher retention with increasing fluence. As a conclusion on the fluence dependence, the experimental data show that above 500 K, deuterium retention in tungsten increases with fluence to the power 0.5-1, indicating a clear dependence on the particle flux [4, 29, 33, 34].

Alimov *et al.* [35] exposed polycrystalline tungsten to deuterium fluence 10^{26} m^{-2} and 10^{27} m^{-2}, flux $10^{22} m^{-2} s^{-1}$, ion energy 38 eV at various surface temperatures. It was shown that the TDS profiles shape and desorption peak changed with exposure temperature and ion fluence. Desorption temperature increased for higher exposure temperatures and fluence, indicating their impact on the deuterium depth distribution and trapping energies of deuterium in tungsten. Furthermore, a discrepancy between the D retention determined from ion beam analyses and TDS was observed, possibly due to diffusion of D deeper than the information depth given from the ion beam analyses.

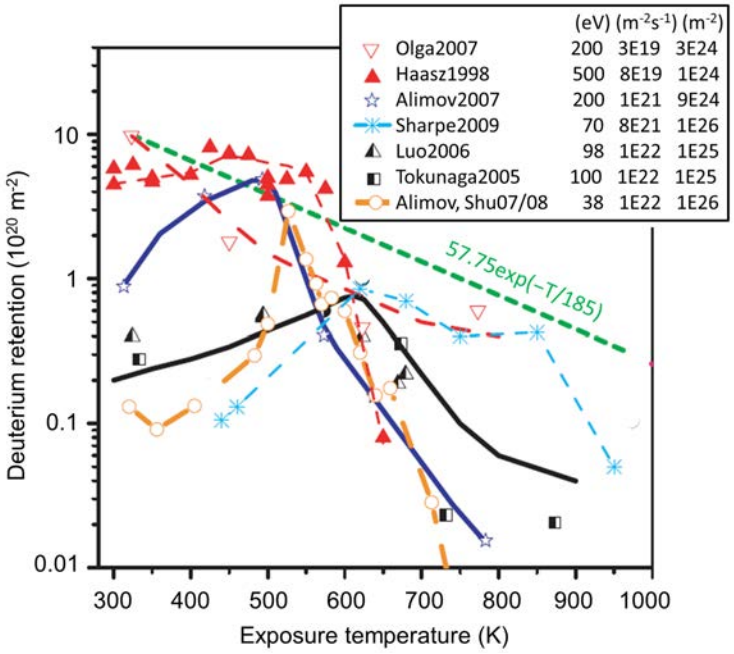

Figure 2.11: Total deuterium retention in polycrystalline tungsten as a function of exposure temperature [29]

The total hydrogen retention dependence on fluence, as plotted in figure 2.10, is given at one particular temperature (∼500 K). Experiments have shown that

hydrogen inventory and blistering are dependent on surface temperature during exposure [15, 36–41]. Lipschultz *et al.* [29], plotted hydrogen retention data from various experiments in the temperature range 300-1000 K, ion energy 38-500 eV, flux $\sim 10^{19}$-10^{22} $m^{-2}s^{-1}$ assuming that the total retention scales as fluence to the power 0.66 (see figure 2.11). All the separated curves connecting the single points correspond to experiments done at the same ion flux. From these data it is evident that the deuterium retention shows a maximum around 400-600 K, possibly due to the thermally activated trapping and de-trapping processes and diffusion. Considering the temperatures where deuterium retention is maximum, the temperature dependence was fitted to 57.75exp(-T/185). For temperatures above 500 K the total hydrogen retention decreases.

Comparing Alimov *et al.* [15] and Tokunaga *et al.* [40] experiments which were performed at ion energy 200 and 100 eV, deuterium flux 10^{21} and 10^{22} $m^{-2}s^{-1}$, fluence $9 \cdot 10^{24}$ and 10^{25} m^{-2}, the maximum of deuterium retention occurs at a higher temperature and the total retention decreases when the flux increases. The impact of the ion energy is negligible under these conditions [33], based also on the data from O. Ogorodnikova *et al.* [36] and V. Alimov *et al.* [15]. In both studies, tungsten was exposed to the same ion energy (200 eV) and nearly to the same fluence ($\sim 10^{24}$ m^{-2}). The maximum of deuterium retention exposed at lower particle flux ($3 \cdot 10^{19}$ $m^{-2}s^{-1}$) occurs at a lower exposure temperature $\sim$300 K while it occurs at $\sim$500 K when the exposure flux increased about two orders of magnitude (10^{21} $m^{-2}s^{-1}$).

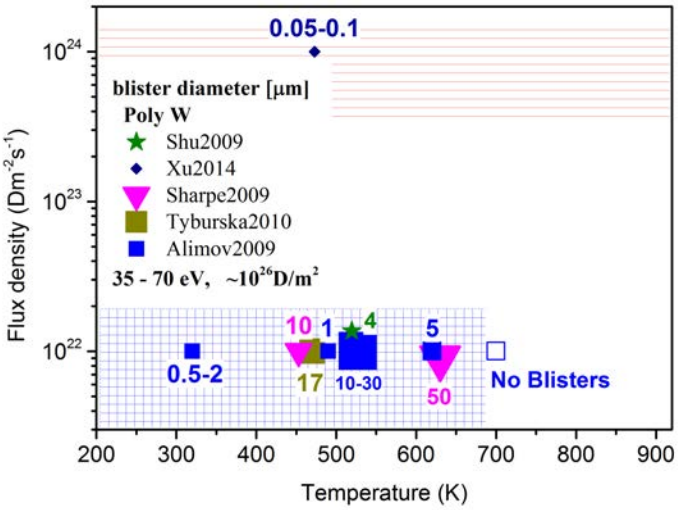

Figure 2.12: Blister formation domain as a function of surface temperature and particle flux: Shu2009 [42], Xu2014 [43], Sharpe2009 [41], Tyburska2010 [44], Alimov2009 [32]

Exposure of tungsten to deuterium plasma makes the surface prone to morphology changes as a result of blister formation. To summarize the visual observations with the electron microscope from the literature, in figure 2.12, the blister formation domain and size distribution relation to surface temperature and ion flux density is plotted.

The total ion fluence in all cases is of the same order of magnitude ($\sim 10^{26}$ m^{-2}), surface temperature is in the range 300-870 K and ion energy varies from 35 to 70 eV. Besides the symbols, in the graph is given the diameter of blisters in micrometer. The graph is sectioned in arbitrary regions in order to point out the blister diameter distribution. In the blue squared region are included exposures done at low flux and temperature where a considerable variety of blister diameters can be noticed. At 700 K no blisters were observed [32] while at high flux exposure, different from expected, Xu *et al.* [43], found blistering to persist on the tungsten surface at about 500 K. These findings demonstrate a clear dependence of surface morphology changes of tungsten under deuterium particle impact on surface temperature and particle flux density.

Systematic studies are however scarce and the large scattering of the data is usually attributed to the different level of impurities and trapping sites in tungsten, sample preparation and experimental loading conditions discrepancies which lead to rather non-trivial conclusions.

2.4.2 Material microstructure

Irradiation from energetic particles is not the only mechanism of defect formation in tungsten, other factors such as mechanical and thermal pre-treatment, surface roughness and material purity are essential. Diffusion of hydrogen in tungsten occurs mainly along the grain boundaries and dislocation sites which are basically formed due to the thermo-mechanical treatment during the manufacturing process. Investigations on the deuterium retention and blistering on various tungsten grades showed a direct correlation between surface modification, retention and material production process, thermal pre-treatment and surface finishing [40]. The effective number of trapping sites is higher in porous tungsten, leading to deeper diffusion of hydrogen into the material and increasing the total retention. Other studies revealed the highest trapping energies in tungsten are associated with grain boundaries and dislocations, vacancies and pores [45]. The presence of impurities in the material has a strong impact on the hydrogen retention due to the additional introduced defects and trapping sites in the lattice [46].

In addition to hydrogen retention, blistering depends strongly on material microstructure. Specifically, it was shown that blistering can be reduced when the tungsten surface is not polished to a mirror finish but it contains scratches which might play the role of additional grain boundaries [47, 48]. Exposure of poly-

crystalline tungsten at 520 K to deuterium plasma showed that grains with lattice orientation (111) perpendicular to the plasma beam, are more prone to blister formation, while on the other grains with orientation (101) or close, larger blisters appeared at a lower areal density. This phenomena could be attributed to the plastic deformations as a consequence of high local stresses [49].

The dislocation density in the material can be reduced when it undergoes thermal treatment. Depending on the heating temperature, tungsten can be recrystallized, leading to different grain size and amount of intrinsic defects namely grain boundaries, dislocations, pores [50]. Y. Ueda *et al.* [46] observed complex plateau-like shapes and cracking on the recrystallized tungsten samples (rec. at 1573 K) after the hydrogen exposure. Reduced blistering was reported from W. M. Shu *et al.* [51] on the recrystallized samples (rec. at 1473 K and 2073 K), albeit the vacancy concentration in the near surface region increased, as indicated from positron annihilation spectroscopy measurements. In general, these experiments have shown that deuterium retention is lower in the recrystallized tungsten, suggesting that grain boundaries and intrinsic defect play a dominant role in hydrogen trapping.

In order to separate the effects of grain boundaries and intrinsic crystallographic defects in the material, single crystal tungsten has been investigated due to a low dislocation density and lack of grain boundaries. The results have shown that the hydrogen diffusion rate decreases further in single crystal compared to polycrystalline tungsten. Exposure of single crystal tungsten to deuterium plasma has resulted in a lower retention due to the accumulation of hydrogen in the near surface region which prevents the deeper gas diffusion [11, 52]. This leads to a saturation of the retention at lower fluences in single crystal compared to polycrystalline tungsten. The different behavior can be attributed to the hydrogen diffusion which occurs mainly through the grain boundaries [53, 54].

2.4.3 Combined He/D exposure

Numerous investigations have been performed assessing the influence of helium irradiation on tungsten, as one of the plasma species in a fusion reactor. He bombardment produces surface morphology changes on tungsten such as cracking, bubble formation and nanostructure growth on the surface, referred to as fuzz [55–60].

The penetration depth of He into the material is large for higher energies, therefore the temperature and particle fluence have small impact on the material degradation concerning energetic ions. Blisters have been observed at high incident He ions (8 keV) at room temperature and low fluence ($\sim 10^{21}\ He^{+}m^{-2}$) [60]. The ion energy influences blister formation by increasing the penetration depth from nm range (eV energy) to 1.7 μm (1.3 MeV). It has been shown that a local

atomic percentage of He might cause either blistering (4 $at\%$) or exfoliation (20-40 $at\%$) [61]. It was also shown that ion energy lower than 30 eV, temperature higher than 1300 K and fluence $\sim 10^{26} He^{+} m^{-2}$ are required to create damages in the material such as blisters and voids [62]. He exposure at surface temperature 1120-1320 K caused the formation of nanorods (filaments) on the surface being up to 1 micrometer long and 10-50 nm wide. The growth rate of the modified layer increased with exposure time and surface temperature [58, 63]. These structures which are refereed to as tungsten "fuzz", generally occur at temperatures 1000-2000 K, ion energy E_{ion} $\geq$20 eV and fluence $\sim 10^{25}$ m^{-2} [57] (figure 2.13).

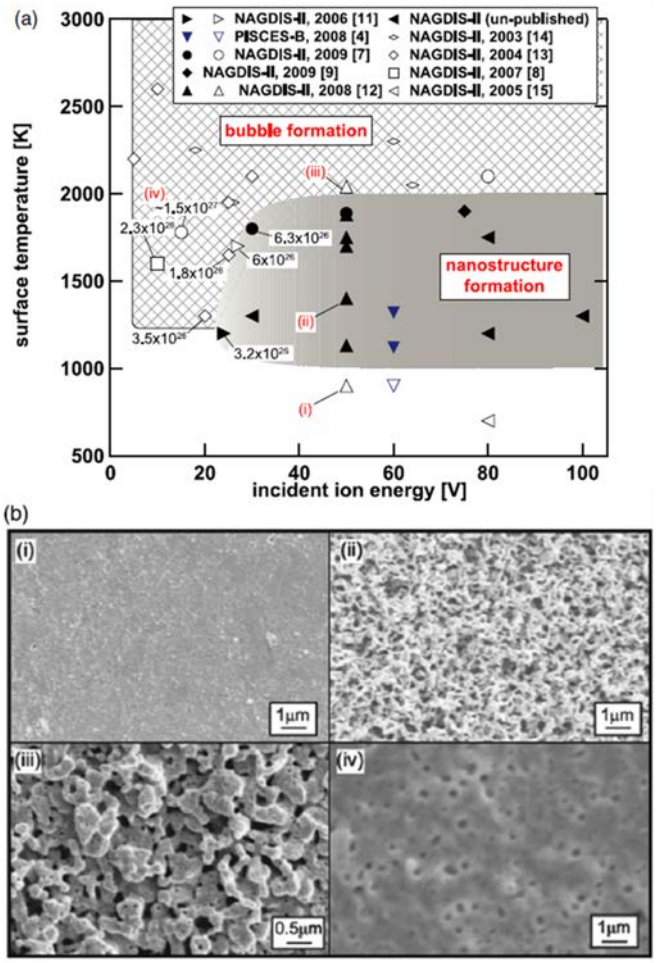

Figure 2.13: Surface nanostructures formation on tungsten as a function of exposure temperature and incident ion energy in He plasma performed at NAGDIS-II and PISCES-B (b) SEM images at the specific conditions corresponding (i)-(iv) [57]

However, D. Nishijima *et al.* [48] has shown that deuterium retention and blistering is suppressed when tungsten samples were pre-exposed to He plasma at 700 K and polished to a mirror finish. This observation was confirmed later on from Alimov *et al.* [32] where besides blister suppression beyond 700 K, they reported a decrease in the total amount of deuterium inventory occurring at temperatures higher than 400 K. The authors explained the formation of vacancies and vacancy clusters as a plastic deformation of the lattice as a response to high stresses exerted from the supersaturation of local concentration of deuterium in the lattice which exceeds the solubility limit. The argument of deuterium intake suppression after exposure to helium seeded plasmas is based on the He bubble formation in the implantation zone where D is trapped [64]. This bubble layer serves as a damper for deuterium to diffuse deeper and in addition it dissipates the stresses formed by the local supersaturation of deuterium.

2.4.4 Transient heat and particle loads

Under ITER-like operation conditions, plasma facing material components (first wall and divertor components) will have to withstand a high level of heat loads. During normal plasma operation, the first wall in ITER is expected to handle thermal loads up to 1 MW/m^2. Tungsten bulk as an armor material in the divertor is foreseen to stand steady state heat loads up to 10 MW/m^2 in case of water cooled components. However, a concern related to the behavior of PFC during transient events are edge localized modes (ELMs), where tens of MJ/m^2 will be deposited in small areas of the divertor during millisecond pulse duration. In ITER, ELMs have to be avoided or mitigated below the damage threshold of the material otherwise local melting, evaporation, particle emission, thermal shock induced crack formation may occur [65].

Many high heat flux (HHF) test facilities have been built worldwide in order to test the performance of PFC under high heat loads, simulating ITER conditions during normal operation and disruptions. These devices provide high thermal loads (energetic electron or hydrogen beams) varying from MW/m^2 to several GW/m^2, on a time frame from several hundreds of microseconds to steady state operation [66]. Transient heat loads have been simulated by either electron beam or laser pulses but there is a fundamental difference which consists on the interaction between the electrons and photons with the substrate and energy deposition leading to a different penetration depth. However, results in terms of heat loads and simulated ELMs parameters are very similar [67].

The second goal of the present study is to address the effect of He nano-bubble layer formed in the near surface region of tungsten under ITER relevant steady state and transient heat and particle loads, simulating ITER ELMs in terms of amplitude, frequency and flux densities [68]. The changes on the surface thermal

conductivity and the bubble growth rate are investigated and compared with the relevant exposures in hydrogen.

References

[1] P. C. Stangeby. *The Plasma Boundary of Magnetic Fusion Devices*. IOP Publishing Ltd., 2000.

[2] K. Christmann. *Interaction of Hydrogen with solid surfaces*. Surface Science Reports, 9:1–163, 1988.

[3] R. Frauenfelder. *Solution and Diffusion of Hydrogen in Tungsten*. Journal of Vacuum Science and Technology, 6:388, 1969.

[4] J. Roth and K. Schmid. *Hydrogen in tungsten as plasma-facing material*. Physica Scripta, T145(014031), 2011.

[5] R. A. Causey. *Hydrogen isotope retention and recycling in fusion reactor plasma-facing components*. Journal of Nuclear Materials, 300:91–117, 2002.

[6] N. Fernandez, Y. Ferroa, and D. Katob. *Hydrogen diffusion and vacancies formation in tungsten: Density Functional Theory calculations and statistical models*. Acta Materialia, 94(2):307318, August 2015.

[7] T. Tanabe. *Review of hydrogen retention in tungsten*. Physica Scripta, T159:014044, 2014.

[8] T. Ikeda, T. Otsuka., and T. Tanabe. *Application of tritium tracer technique to determination of hydrogen diffusion coefficients and permeation rate near room temperature for tungsten*. Fusion Science and Technology, 60:1463, 2011.

[9] R. A. Anderl. *et al. Deuterium transport and trapping in polycrystalline tungsten*. Fusion technology, 21:745 –752, 1992.

[10] O. Ogorodnikova, J. Roth, and M. Mayer. *Deuterium retention in tungsten in dependence of the surface conditions*. Journal of Nuclear Materials, 313-316:469–477, 2003.

[11] A. A. Haasz. *et al. Deuterium retention in single crystal tungsten*. Journal of Nuclear Materials, 290-293:85–88, 2001.

[12] V. Alimov. *et al. Differential cross-section of the D(3He,p)4He nuclear reaction and depth profiling of deuterium up to large depths*. Nuclear Instruments and Methods in Physics, 234:169175, 2005.

[13] S. Nagata. *et al. Helium and hydrogen trapping in W and Mo single-crystals irradiated by He ions*. Journal of Nuclear Materials, 307311:15131516, 2002.

[14] T. Shimada. *et al. Blister formation in tungsten by hydrogen and carbon mixed ion beam irradiation*. Journal of Nuclear Materials, 313-316:204–208, 2003.

[15] V. Alimov. *et al. Deuterium retention in tungsten exposed to low-energy, high-flux clean and carbon-seeded deuterium plasmas*. Journal of Nuclear Materials, 375:192201, 2008.

[16] A. M. de Jong and J. W. Niemantsverdriet. *Thermal desorption analysis: comparative test of ten commonly applied procedures*. Surface Science, 233:355–365, 1990.

[17] J. L. Falconer and R. J. Madix. *Flash desorption activation energies: DCOOH decomposition and CO desorption from Ni (110)*. Surface Science, 48:393–405, 1975.

[18] Y. Gasparyan. *On determination of binding energies for hydrogen with radiation defects in tungsten from thermal desorption measurements*. A119. P-95 PFMC15.

[19] A. H. M. Krom and A. Bakker. *Hydrogen trapping models in steel*. METALLURGICAL AND MATERIALS TRANSACTIONS B, 31B:1482, December 2000.

[20] A. Mutzke, R. Schneider, W. Eckstein, and R. Dohmen. *SDTrimSP Version 5.00*. Technical report, IPP 12/8, 2011.

[21] Glen R. Longhurst. *TMAP7 Manual*. Technical report, Idaho National Laboratory Idaho Falls, Idaho 83415-3860, INEEL/EXT-04-02352 Rev. 1.

[22] M. Poon, A.A. Haasz, and J.W. Davis. *Modelling deuterium release during thermal desorption of D+-irradiated tungsten*. Journal of Nuclear Materials, 374:390402, 2008.

[23] T. Venhaus. *et al. Behavior of tungsten exposed to high fluences of low energy hydrogen isotopes*. Journal of Nuclear Materials, 290-293(505-508), 2001.

[24] B. M. U. Scherzer. *Development of surface topography due to gas implantation*. Springer-Verlag, 1983.

[25] S.K. Das and M. Kaminsky. *Blistering in helium-ion-implanted (111) niobium monocrystals*. Journal of Applied Physics, 44(6):2520–2529, 1973. cited By (since 1996)0.

[26] J. H. Evans. Journal of Nuclear Materials, 68:129, 1977.

[27] W. Primak and J. Luthra. *Radiation blistering: Interferometric and microscopic observations of oxides, silicon, and metals*. Journal of Applied Physics, 37(6):2287–2294, 1966. cited By (since 1996)8.

[28] G. Federici. *et al. Key ITER plasma edge and plasma-material interaction issues*. Journal of Nuclear Materials, 313-316:11–22, 2003.

[29] B. Lipschultz. *et al. An Assessment of the Current Data Affecting Tritium Retention and its Use to Project Towards T Retention in ITER*. Plasma Science and Fusion Center Massachusetts Institute of Technology Cambridge MA 02139 USA, PSFC/RR-10-4, 2010.

[30] R. Pitts. *et al. A full tungsten divertor for ITER: Physics issues and design status*. Journal of Nuclear Materials, 438(S48S56), 2013.

[31] O. Ogorodnikova. *et al. Pre-implantation and pre-annealing effects on deuterium retention in tungsten*. Journal of Nuclear Materials, 373:254–258, 2008.

[32] V. Alimov. *et al. Surface morphology and deuterium retention in tungsten exposed to low-energy, high flux pure and helium-seeded deuterium plasmas*. Physica Scripta, T138:014048, 2009.

[33] Z. Tian. *et al. Deuterium retention in tungsten at fluences of up to* 10^{26} D^+/m^2 *using* D^+ *ion beams*. Journal of Nuclear Materials, 399:101–107, 2010.

[34] R. Doerner. *Private communication*.

[35] V. Alimov. *et al. Temperature dependence of surface morphology and deuterium retention in polycrystalline ITER-grade tungsten exposed to low-energy, high-flux D plasma*. Journal of Nuclear Materials, 420:519–524, 2012.

[36] O. Ogorodnikova. *et al. Ion-driven deuterium retention in tungsten*. Journal of applied physics, 103:034902, 2008.

[37] G. N. Luo. *et al. Influence of blistering on deuterium retention in tungsten irradiated by high flux deuterium 10-100 eV plasmas*. Fusion Engineering and Design, 81:957962, 2006.

[38] A. A. Haasz. *et al. Deuterium retention in tungsten for fusion use*. Journal of Nuclear Materials, 258-263:889895, 1998.

[39] W. Shu. *et al. Temperature dependence of blistering and deuterium retention in tungsten exposed to high-flux and low-energy deuterium plasma*. Fusion Engineering and Design, 83:10441048, 2008.

[40] K. Tokunaga. *et al. Blister formation and deuterium retention on tungsten exposed to low energy and high flux deuterium plasma*. Journal of Nuclear Materials, 337339:887891, 2005.

[41] J. P. Sharpe. *et al. Retention behavior in tungsten and molybdenum exposed to high fluences of deuterium ions in TPE*. Journal of Nuclear Materials, 390391:709712, 2009.

[42] W. M. Shu. *et al. Recent findings on blistering and deuterium retention in tungsten exposed to high-fluence deuterium plasma*. Journal of Nuclear Materials, 386-388(C):356–359, 2009.

[43] H. Y. Xu. *et al. Deuterium-induced nanostructure formation on tungsten exposed to high-flux plasma*. Journal of Nuclear Materials, 2014.

[44] B. Tyburska. *Deuterium Retention in Carbonand Self-Implanted Tungsten*. PhD thesis, Marie Curie-Sklodowska University, Lublin, Poland, 2010.

[45] O. Ogorodnikova. *et al. Deuterium retention in different tungsten grades*. Physica Scripta, T138:014053 (5pp), 2009.

[46] Y. Ueda. *et al. Hydrogen blister formation and cracking behavior for various tungsten materials*. Journal of Nuclear Materials, 337-339:1010–1014, 2005.

[47] G. Luo. *et al. Behavior of tungsten with exposure to deuterium plasmas*. Nuclear Instruments and Methods in Physics Research, 267(18):3041–3045, 2009.

[48] D. Nishijima. *et al. Suppression of blister formation and deuterium retention on tungsten surface due to mechanical polishing and helium pre-exposure*. Nuclear Fusion, 45(7):669–674, 2005.

[49] W. M. Shu. *et al. Microstructure dependence of deuterium retention and blistering in the near-surface region of tungsten exposed to high flux deuterium plasmas of 38 eV at 315K*. Physica Scripta . Scr. T128 (2007) 9699, 2007.

[50] A. Manhard. *Deuterium Inventory in Tungsten After Plasma Exposure: A Microstructural Survey*. PhD thesis, Universitat Augsburg, 2011.

[51] W. M. Shu. *et al. Mechanisms of retention and blistering in near-surface region of tungsten exposed to high flux deuterium plasmas of tens of eV*. Journal of Nuclear Materials, 367-370 B:1463–1467, 2007.

[52] M. Poon. *et al. Impurity effects and temperature dependence of D retention in single crystal tungsten*. Journal of Nuclear Materials, 313316:199203, 2003.

[53] V. Alimov. *et al. Depth distribution of deuterium in single- and polycrystalline tungsten up to depths of several micrometers*. Journal of Nuclear Materials, 337339:619623, 2005.

[54] J. P. Roszell. *et al. Deuterium retention in single-crystal tungsten irradiated with 10500 eV/D+*. Journal of Nuclear Materials, 438:S1084S1087, 2013.

[55] B. Cipiti and G.L. Kulcinski. *Helium and deuterium implantation in tungsten at elevated temperatures*. Journal of Nuclear Materials, 347:298306, 2005.

[56] M. Baldwin. *et al. The effects of high fluence mixed-species (deuterium, helium, beryllium) plasma interactions with tungsten*. Journal of Nuclear Materials, 390391:886890, 2009.

[57] S. Kajita. *et al. Formation process of tungsten nanostructure by the exposure to helium plasma under fusion relevant plasma conditions*. Nuclear Fusion, 49(6pp):095005, 2009.

[58] G. De Temmerman. *et al. Nanostructuring of molybdenum and tungsten surfaces by low-energy helium ions*. Journal of Vacuum Science and Technology, A 30(041306), 2012.

[59] M. Li. *et al. Radiation damage of tungsten surfaces by low energy helium atom bombardment A molecular dynamics study*. Journal of Nuclear Materials, 433:1722, 2013.

[60] Zhang Fu. *et al. Thermal desorption and surface modification of He+ implanted into tungsten*. Journal of Nuclear Materials, 329333:692–696, 2004.

[61] S. Gilliam. *et al. Retention and surface blistering of helium irradiated tungsten as a first wall material*. Journal of Nuclear Materials, 347:289297, 2005.

[62] Y. Ishijima. *et al. Current status of ductile tungsten alloy development by mechanical alloying*. Journal of Nuclear Materials, 329-333:775–779, 2004.

[63] M. J. Baldwin and R. P. Doerner. *Helium induced nanoscopic morphology on tungsten under fusion relevant plasma conditions*. Nuclear Fusion, 48:035001 (5pp), 2008.

[64] M. Reinhart. *Influence of impurities on the fuel retention in fusion reactors*. PhD thesis, Fakultat fuer Physik und Astronomie der Ruhr-Universitat Bochum, 2015.

[65] D. Maisonnier. *et al. Power plant conceptual studies in Europe*. Nuclear Fusion, 47:15241532, 2007.

[66] T. Hirai. Materials Transactions, 46(3):412, 2005.

[67] M. Wirtz. *et al. Comparison of thermal shock damages induced by different simulation methods on tungsten*. Journal of Nuclear Materials, 438:S833S836, 2013.

[68] R. Pitts. *Response of tungsten surfaces to helium plasma exposure under ITER relevant steady state and repetitive (sub-melting threshold) transient conditions. Technical Specifications*. https://user.iter.org/?uid=NEAK42, 2014.

3

Experimental setup and analysis techniques

3.1 Linear plasma devices

Experiments were carried out in linear plasma devices (LPD) due to the possibility of generating high particle fluences and fluxes, according to specific experimental requirements. In addition, it is more feasible to control the exposure conditions such as sample temperature, plasma species and ion energy than in more complex and less accessible devices such as tokamaks. For the work in this thesis, three different linear plasma devices were used, Magnum/Pilot-PSI, PSI-2 and Pisces-A [1–3]. In table 3.1 is given a summary of the main plasma parameters in linear

Linear Plasma Devices	Magnum/Pilot-PSI	PSI-2	PISCES-A
Ion flux density$(m^{-2}s^{-1})$	$10^{23} - 10^{25}$	$10^{21} - 10^{23}$	$10^{21} - 10^{23}$
Electron temperature (eV)	$0.1 - 10$	$1 - 20$	$5 - 20$
Electron density (m^{-3})	$10^{19} - 10^{21}$	$10^{17} - 10^{19}$	$10^{18} - 10^{19}$
Power density (MW/m^2)	≥ 10	≤ 1	$0.5 - 1.25$
Magnetic field (T)	$0.4 - 1.6$	0.1	$0.2 - 0.4$
Pulse length	10 s to SS	SS	SS

Table 3.1: Main plasma parameters of low and high flux LPDs. SS stands for steady state operation [1–3]

devices which are relevant for the present study. A broader overview of the operational principle and detailed description of the experiments is presented in the following sections.

3.1.1 Magnum/Pilot-PSI

The high particle flux density experiments were performed in Magnum and Pilot-PSI linear plasma devices which are situated at DIFFER [4]. Pilot-PSI is a pilot experiment, forerunner of Magnum-PSI which was built to validate different techniques before applying them at Magnum-PSI. In figure 3.1, an overview of the Pilot-PSI design is given and in figure 3.3, the heat flux profiles as a function of applied discharge current and magnetic field under steady-state plasma operation, are plotted [2]. The plasma beam is generated by a cascaded arc source. Depending on the strength of the axial confining magnetic field (0.4-1.6 T), it operates under either steady-state or pulsed mode [5]. The working gas is injected at the source and the plasma beam spreads in a nearly 1 m long vacuum vessel with a neutral background density lower than 0.01 mbar.

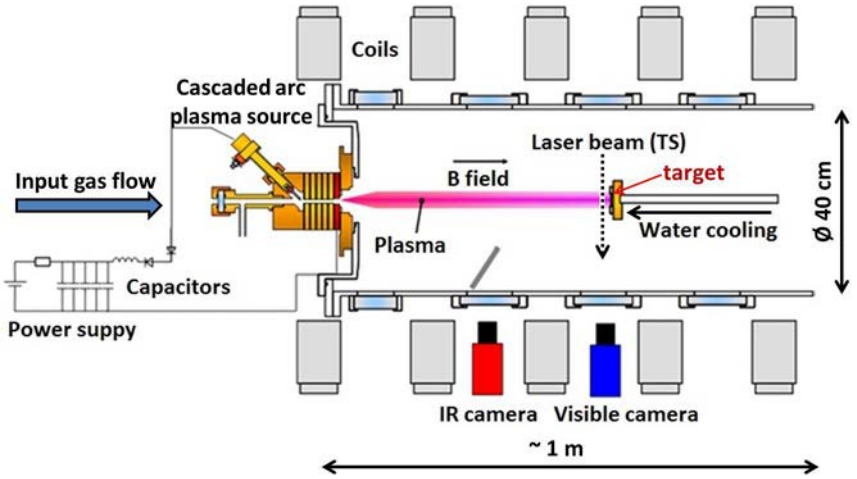

Figure 3.1: Schematic overview of Pilot-PSI linear plasma device [5]

A particular feature of Pilot-PSI device is the high particle flux and power density plasmas which can be generated under steady state and transient operation using a pulsed plasma source. In this case, a DC power supply (100-200 A) is connected in parallel with a capacitor bank which allows superimposing the transient input power generating plasma pulses with a duration up to 1.5 ms [6]. In He/H experiments, the simulated ELM duration was 1 ms, produced at a frequency of 10 Hz while the capacitor bank transient voltage was varied in the range 1200-1800

V. In case of longer exposure time (1000 s), a laser (FLS352N 307) was used to generate high transient heat loads combined with the plasma exposure which is limited to 10 s duration at the highest magnetic field setting.

Plasma electron density and temperature were measured using a Thompson scattering setup [7] by firing a Nd:YAG laser beam of 532 nm, 25 mm in front of the target. Particle flux was calculated by the formula: $\Phi = (n_e/2)(2k_B T_e/m_D)^{0.5}$. In these experiments, plasma consisted mainly of singly ionized ions and the ion energy was calculated from the empirical formula $E_{ion} = U_{bias} - 2kT_e$ [8]. An accelerating negative voltage of -50 V was applied on the target, which yield the desired ion energy of 40 eV while the influence of the plasma potential was negligible. Due to the necessity of producing high particle flux plasmas, Pilot-PSI was operated in a pulsed mode with pulse lengths limited by the capabilities to cool the magnets; hereby the total fluence of 10^{26} m^{-2} was accumulated in several consecutive discharges.

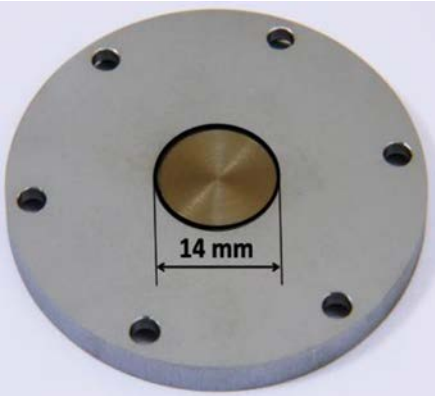

Figure 3.2: Tungsten sample and the molybdenum clamping ring used to mount the sample at Pilot and Magnum-PSI

In figure 3.2, a tungsten sample with a molybdenum clamping ring is shown, which was used to mount it at Pilot-PSI linear plasma device. They were clamped in an water-cooled holder (295 K) and aligned properly with the maximum of the plasma temperature and density profile (see figure 3.3). The surface temperature variation on the tungsten samples was achieved by varying the magnetic field strength and the physical contact of the sample with the water-cooled holder. A fast infrared camera (FLIR SC5500MB) and a spectral pyrometer were used to measure the temperature evolution. The high enough spatial (24 μm/pixel) and time ($\sim$270 μs) resolution of the IR camera allows the detection of simulated transient heat and particle loads.

In the figure 3.4, the temperature profile along the sample diameter is given. Due to the plasma profile, the temperature varies within 50 K from the center

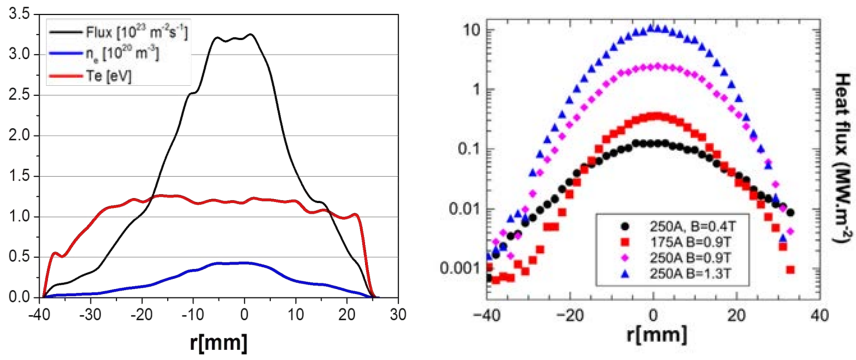

Figure 3.3: On the left graph are plotted the electron density, temperature and ion flux profiles at Magnum-PSI taken from the Thomson scattering measurements (sample LGW/530K/HF). On the right graph is given the heat flux profiles as a function of applied discharge current and magnetic field during plasma operation at Pilot-PSI [2]

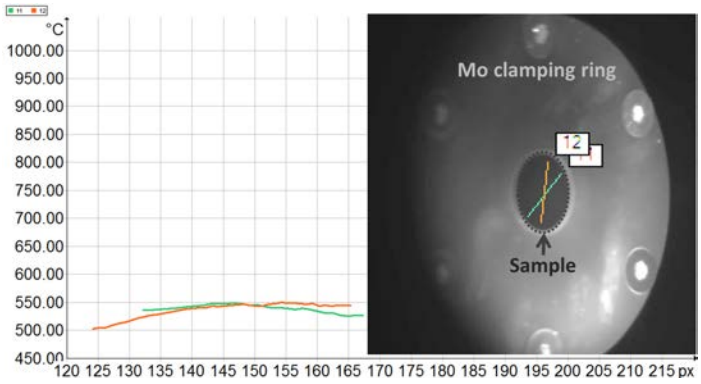

Figure 3.4: Infrared camera temperature profile along the sample recorded on the sample exposed to Magnum-PSI

to the sample edge. The time evolution of the temperature is plotted in figure 3.5 for a 12 s long plasma pulse duration. A seen from the plot, in the first 2 s, after the magnetic field is switched on, the sample has reached $\sim$80% of the maximum temperature and the maximum temperature is rather flat in the last 5 s of the plasma exposure. Immediately after the magnetic field is switched off, the sample is cooled down to room temperature. This is an example of the most critical case concerning the temperature space-and-time evolution. The sample was exposed to high temperature and the magnetic field was highest, therefore the plasma pulse was limited to only 12 s. The pulse-to-pulse reproducibility was achieved within an accuracy of about 10%. Simulations with the CRDS code of the

ion implantation and desorption, showed that the real pulsed temperature profile has no effect on the deuterium desorption process (see chapter 4).

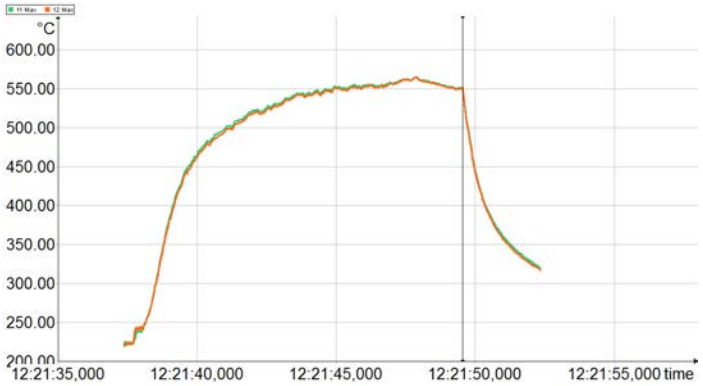

Figure 3.5: Time evolution of surface temperature recorded on the sample exposed to Magnum-PSI

3.1.2 PSI-2

Lower particle flux density experiments were carried out at PSI-2 linear plasma device which is operated at Forschungszentrum Jülich [9]. The plasma at PSI-2 is generated by an arc discharge, using a cylindrical LaB_6 heated cathode and a *Mo* hollow anode [1, 10].

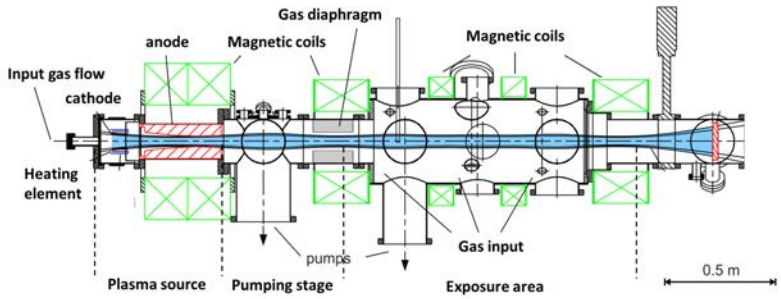

Figure 3.6: Schematic overview of PSI-2 linear plasma device [11]

The plasma column has a hollow density and temperature profile with a diameter of 5-15 cm confined by a 0.1 T axial magnetic field at the exposure position. A quadrupole mass spectrometer and optical emission spectroscopy are used to monitor the level of impurities in the plasma. In figure 3.6, an overview scheme

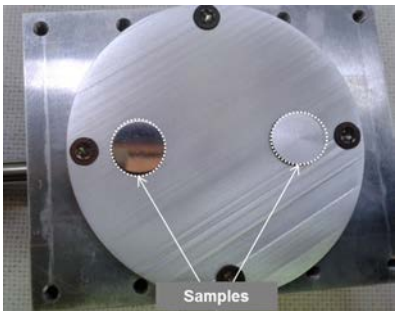

Figure 3.7: Sample holder with samples exposed to PSI-2. Temperature was regulated by changing the thermal contact with the cooled holder

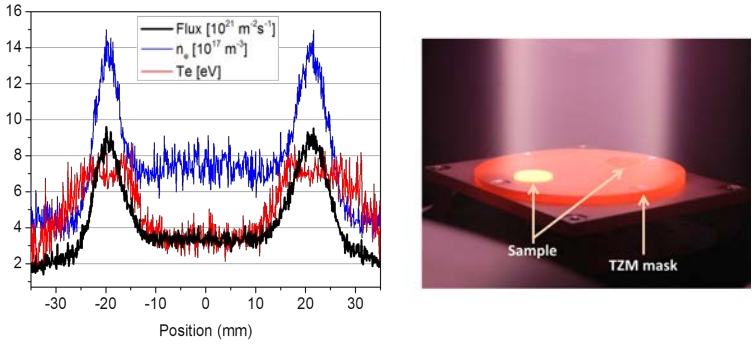

Figure 3.8: On the left graph is plotted the electron density, temperature and ion flux profiles at PSI-2 taken from the Langmuir probe measurements and on the right is given a picture of samples exposed at PSI-2. Temperature on the back of the sample measured by the thermocouple is around 1370 K

of PSI-2 and its main diagnostic systems are given. Plasma parameters, n_e and T_e, were deduced from the I-V characteristic measured with a double Langmuir probe and the particle flux was calculated in the same way as in Pilot-PSI case. In figure 3.8 the electron density and temperature profiles are plotted, measured with the Langmuir probe. Also in the case of PSI-2, targets were clamped on a water cooled holder and aligned properly with the maximum of the plasma profile. The effects of the radial distribution of plasma parameters were taken into account when calculating the total deuterium desorption while the surface modifications were investigated in the center of the sample which corresponds to the maximum of the plasma parameters.

Depending on the applied clamping force of the sample on the cooling structure, it was feasible to vary the temperature of the sample during the plasma exposure. A fast infrared camera (FLIR SC5500MB) was used also in this case to

measure the temperature and in addition a thermocouple was mounted on the back of the sample. The nominal temperature was typically reached in a few minutes and the profile along the sample surface was rather homogeneous. PSI-2 is operated under steady-state conditions therefore the required particle fluence (10^{26} m^{-2}) was accumulated in a single plasma exposure. In all experiments, deuterium plasma consisted mainly of singly ionized ions (D^+). An external biasing of the target to -60 V was applied, which yield the desired ion energy at 40 eV.

3.1.3 PISCES-A

PISCES-A is a linear plasma device situated at the University of California in San Diego and it is exploited in the frame of plasma material interaction research program. Its identical twin device, PISCES-B which is located in the same laboratory in a hot cell, is dedicated mainly to plasma material interaction experiments including toxic materials such as beryllium [12]. The flat plasma profile is generated from a reflex arc discharge between a disc LaB_6 cathode and a cylindrical *Cu* anode with a plasma column diameter of 5-10 cm. It is confined by a magnetic field 0.2-0.4 T in a 2.5 m long and 0.2 m in diameter vacuum chamber [3]. A schematic overview of the device is given in figure 3.9. PISCES and PSI-2 and are very similar in terms of plasma parameters (table 3.1). Particle flux reaches $10^{21} - 10^{23}$ $m^{-2}s^{-1}$ with an electron temperature 5-20 eV and density $\sim 10^{18} - 10^{19}$ m^{-3}.

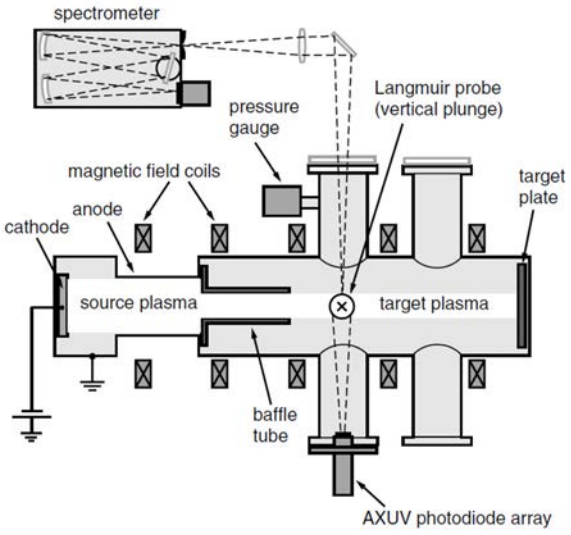

Figure 3.9: Schematic overview of PISCES-A linear plasma device [13]

Both, air and water cooling could be applied on the back of the sample in order to control the temperature. In the present experiments, the aimed temperature

range was 520-1090 K therefore air cooling resulted to be the most efficient. The sample was clamped on the holder with a *Mo* cap, a grafoil was placed for a better thermal contact with the holder and a thermocouple was mounted on the back of the sample to measure the temperature. Like in the previous experiments, during the plasma exposure, samples were externally biased to -50 V.

The main objective of PISCES experiments was the investigation of the role of particle flux on deuterium retention and surface modifications when He impurities are present in the plasma. Recrystallized tungsten samples were exposed to He/D plasma mixtures with 5%He content. PISCES provides a well-developed spectroscopic diagnostic system (USB4000) which allows the determination of the ion ratio in the plasma based on the measurement of HeI (447.1 nm) line intensity. The quantitative data are useful in order to better understand the exposure effects in the material as well as an input for the modeling of the TDS profiles.

Due to the low electron temperature in the plasma ($T_e < 10$ eV), helium is mainly singly ionized He^+ therefore the density of doubly ionized helium $n_{He^{+2}}$ is negligible. According to the conventional spectroscopic method, the density of He^+ ions (n_{He+}) is obtained from the absolute intensity of HeII line (λ = 468,6 nm):

$$I_{HeII} = \frac{L}{4\pi} < \sigma\nu >_{HeII} n_e n_{He+} \left[\frac{photons}{m^2 ssr}\right] \tag{3.1}$$

where L is the path length at the line-of-sight and $< \sigma\nu >_{HeII}$ is the photon emissivity coefficient as a function of n_e and T_e. In the electron temperature range $T_e < 10$ eV, the photon emissivity coefficient (as specified in ADAS database) decreases rapidly, generating large errors in estimating n_{He+}. In addition, HeII line (λ = 468,6 nm) is difficult to detect in D plasma with low concentration of He. Therefore, a new method which relies in the determination of n_{He+} from the intensity of HeI (λ = 447.1 nm) line was developed and applied at PISCES from Nishijima *et al.* [14]. The main idea of the method relies on obtaining the ionization flux of neutral He^0 to He^+ ($\Gamma_{He^0 \rightarrow He^+}$) from the product of the ionization event per photon (S/XB) of the helium neutral line intensity (I_{HeI}) with the intensity of the HeI line (λ = 447.1 nm).

Applying a 0-D continuity equation for He^+ ions in equilibrium between the ionization source and radial transport loss, yields the density of He^+ ions as follows:

$$n_{He+} = \frac{\tau_{He^+}^{perp} \Gamma_{He^0 \rightarrow He^+}}{L} = \frac{\tau_{He^+}^{perp} 4\pi I_{HeI}}{L} \frac{S}{XB} \tag{3.2}$$

$\tau_{He^+}^{perp}$ is the radial confinement time of He^+ ions in the plasma which is calculated by assuming the Bohm diffusion coefficient. The ionization event per photon (S/XB) for the HeI line was calculated with the collision-radiative model, taking

into account the He^+ losses due to radiation trapping. In a D_2/He mixed plasma, the He^+ losses due to molecular assisted recombination are more significant for deuterium pressure $P_{D_2} > 4 \cdot 10^{-3}$ mbar while losses due to molecular assisted dissociation processes are considerable at any P_{D_2} [13–17].

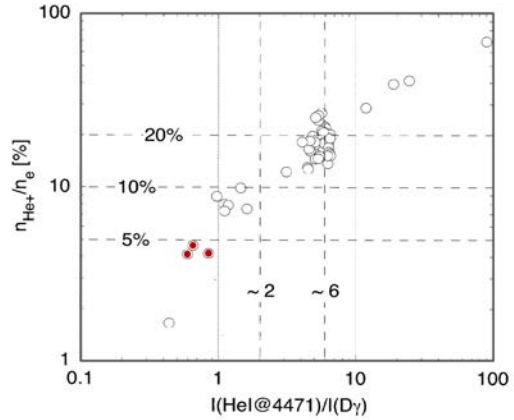

Figure 3.10: Experimental results on the relation between the ion ratio in the plasma from the intensity of the HeI and D_γ lines [18]

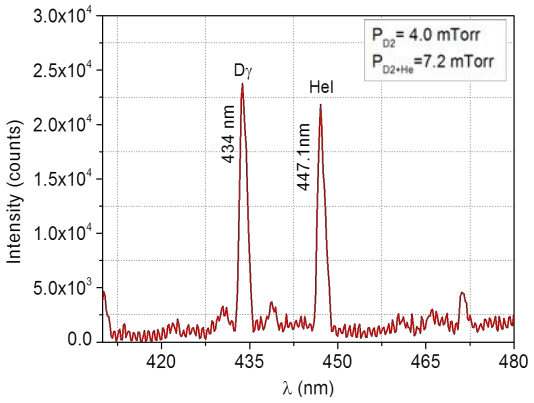

Figure 3.11: Spectroscopic measurements of the mixed He/D plasma at a total gas pressure $P_{D_2+He} \sim 9.6 \cdot 10^{-3}$ mbar

In the figure 3.10, the experimental result of HeI and D_γ line intensity measurements in the He/D mixed plasma are plotted. In the graph, it is indicated the ratio of line intensities which should be in the range 0.8-0.9 in order to have 5% of He ions in the plasma. First D plasma was generated keeping a gas pressure at about $P_{D_2} \sim 5.3 \cdot 10^{-3} mbar$ and then He was added into the chamber until the pressure reached $P_{D_2+He} \sim 9.6 \cdot 10^{-3}$ mbar. While He was added to the chamber,

special care was taken in keeping the intensities of HeI line (λ=447.1 nm) and D_γ (λ=434 nm) at around 0.8-0.9 (figure 3.11).

3.2 Analysis techniques

Post mortem analysis of the plasma exposed samples required the utilization of various analysis techniques. Scanning and transmission electron microscopy (SEM/TEM), electron backscattering diffraction (EBSD) and energy dispersive X-ray spectroscopy technique (EDX) were used to study the surface modifications, material microstructure and surface elemental composition. Roughness measurements were done using a DEKTAK stylus profilometer and confocal microscope. Thermal desorption spectroscopy (TDS), secondary ion mass spectroscopy (SIMS) and nuclear reaction analysis (NRA) were used to investigate the total deuterium retention and deuterium depth distribution. A more detailed insight on the different methods and principles of operation is given in the following sections.

3.2.1 Electron microscopy

Surface morphology of the samples was investigated with a scanning electron microscope (SEM) which is based on the interaction of a finely focused monochromatic electron beam with the material [19, 20]. A crucial advantage of the electron microscope is the wavelength of the imaging source which can be reduced by increasing the accelerating voltage, typically from 8.58 pm (20 kV) to 2.5 pm (200 kV). Depending on the accelerating voltage and material density, the volume of the material which is excited by the incident electron beam produces a signal which is captured by the detectors, amplified, digitalized and sent to a viewing screen where the image is developed. Part of the signal are the secondary, backscattered and Auger electrons as well as continuous, characteristic and fluorescent X-rays. Capturing and analyzing the secondary electrons (SE), which have low energy as they are excited from the first few nanometer of the material, generates high resolution images. Valuable information on the topography and composition of the material can be acquired by analyzing the backscattered electrons (BSE). Both SE and BSE detectors were used for the imaging of the samples with an accelerating voltage varying from 5 kV to 20 kV, depending on the specific task.

When the electron beam passes though very thin specimen placed between electromagnetic lenses of an electron microscope, the transmitted electrons (TEM), after interacting with the material atoms, are projected in a fluorescent screen, revealing information about the size distribution, shape and area density of structural defects.

Information related to the symmetry of the crystal, orientation and angular relationship of the crystallographic planes is acquired by using the electron backscatter

diffraction (EBSD). Tilting the polished sample to a small angle with the incident electron beam (usually 20^o), the low energy back scattered electrons will form diffraction patterns on a screen placed on their path. Constructive and destructive interference occur due to the path differences when the electron beam with a given wavelength interacts with the crystal lattice as described in Bragg's equation $\lambda = 2dsin\theta$. EBSD data processing software can generate 2D maps of the grain size, shape and orientation. Inverse pole figure colored map assigns full red, blue and green to the cubic phases which normal direction is parallel to the [001], [111] and [101] axes respectively [21, 22]. Microscopy analysis were performed at Forschungszentrum Jülich.

3.2.2 Profilometry

Roughness measurements were done using a DEKTAK stylus profilometer which scans the surface by electromechanical means, situated at the MirrorLab in Forschungszentrum Jülich. This device is equipped with a diamond stylus (radius: 12.5 μm) which is mechanically connected to the Linear Variable Differential Transformer (LVDT). As the stylus height changes during scanning, the LVDT core moves according to the scan, producing electrical signals with amplitude which corresponds vertical displacements of the stylus. After being converted, the signal is transmitted to the computer. The roughness is determined from the root mean square (RMS) of the arithmetic average deviation from the mean line. In the present analysis, typically a scanning length of 200 μm and 3 mg stylus force was applied on the sample surface.

3.2.3 Secondary Ion Mass Spectrometry (SIMS)

Deuterium depth profiling in tungsten samples was probed with secondary ion mass spectrometry (SIMS) technique. SIMS is a destructive method used to investigate the elemental composition of surface and thin layers by sputtering the material with heavy ions (primary beam: O_2^+, O^-, Cs^+, Ar^+ or neutrals). Secondary ions are ejected from the material surface because of the primary ion beam bombardment. In addition, singular atoms or molecules are sputtered from the target surface which are subsequently ionized with different efficiencies [23, 24]. The sputtering rate varies with the incident ion energy, current, sample material composition and crystal orientation. After being produced, the secondary ion beam is extracted from the sample surface and transferred to a time-of-flight mass-spectrometer by an electrostatic lens. The generated signal is then recorded by a collecting detector.

Recent studies have demonstrated positive results in terms of the SIMS technique reliability, showing compatible results with ion beam analysis (NRA) in case of deuterium depth profiling in pure tungsten where no matrix effect is present

[25–27]. SIMS measurements were carried out at the ZEA-3 institute [9] with a Cs^+ primary beam of 2 keV which was used for the sputtering of an area $300 \times 300\mu m^2$ in the center of the target. D^+ ions were analyzed with a detection limit in the range $5.6 \cdot 10{-}4$ at.fr and 'nm' depth resolution. The large depth resolution in the near surface region is specifically advantageous and complementary to the quantitative nuclear reaction analysis data which have a better detection limit, namely 10^{-5} at.fr [28].

3.2.4 Nuclear Reaction Analysis (NRA)

Quantitative deuterium depth profiles on the tungsten samples were investigated with nuclear reaction analysis (NRA) at the 3 MV tandem accelerator situated at IPP-Garching, Germany. A ^3He ion beam was used to bombard the tungsten sample and probe the deuterium content by detecting and analyzing the products of the nuclear reaction $D(^3He, p)\alpha$ [29]. This is an exothermic reaction with a Q=18.35 MeV, resulting proton energy in the range 11-14 MeV and a full width half maximum (FWHM) resonant cross-section at 730 keV of incident projectile energy. The differential cross-sections are taken from Alimov *et al.* [30] measurements which were done at a laboratory angle of 135^o.

After the nuclear reaction is initialized, the reaction products (p, α) are captured from detectors and their energy distribution and scatter cross-sections give information on the depth profile of deuterium in the investigated layer. The depth resolution δ is defined as the ratio of energy range of the detected particles generated at a depth 'x' (at FWHM) with the effective stopping power [31]:

$$\delta_x = \frac{\Delta E_d(x)}{E_{eff}} \tag{3.3}$$

E_{eff} indicates the stopping power or the effective energy loss of the incoming incident particles and outgoing nuclear reaction products per unit length in the substrate:

$$E_{eff} = \frac{\partial E_d(x)}{\partial x} \tag{3.4}$$

Considering the high stopping power of tungsten, at 6 MeV beam energy of the ^3He ion beam, about 12 μm depth can be probed with a sensitivity in the 'ppm' range. By varying the energy of the incident beam, the energy profile of the outgoing particles (p, α) will change accordingly, therefore more information can be acquired on the deuterium depth distribution. Proton spectra recorded for the nuclear reaction $D(^3He, p)\alpha$ yield a depth resolution of $\sim$150 nm in the near surface region (at about 200 nm) for 0.5 MeV of incident ^3He ion beam and $\sim$1.5 μm at a depth $\sim$12 μm at 4 MeV of incident ^3He ion beam [28]. Whereas the low energy α- particle profiles can be used to acquire a better depth resolution in the near surface region at lower incident $^3He^+$ energies. During the measurements,

the proton and alpha detectors were set in 135^o and 102^o angle respectively and the beam spot was about 1 mm^2. The ^3He ion beam energy was varied in the range 0.5-6 MeV. In order to fully stop the high energy generated protons it was required a thick detector with a depletion depth of 2 mm.

The calculation and deconvolution of the experimental proton and alpha particle energy profiles, recorded at various incident ^3He ion energies, were done using the SIMNRA [32] and NRADC [33] programs. The reconstruction of the deuterium concentration depth profile is done by slicing the depth profile into layers with constant deuterium concentration and finding the optimal number, thickness and deuterium content for each layer. For the analysis is needed a SIMNRA template file in which is specified the setup of the experiment (detectors, foil, etc.) and the target which consists of tungsten, deuterium and a thin layer of carbon (typically 1 monolayer), necessary for the energy calibration. The regions of interest are selected from the measured data (α and p profiles) and an initial layout is created by choosing a number of sublayers per each layer (usually 4 sublayers) which is then optimized by the program. After providing this input, NRADC program builds up a linear system based on the assumption that for lower deuterium concentrations in tungsten, the stopping power of incident and outgoing particles depends on tungsten only. Therefore, the measured intensity of protons/alphas of a certain channel is a product of the deuterium concentration from a specific sublayer multiplied by a coefficient.

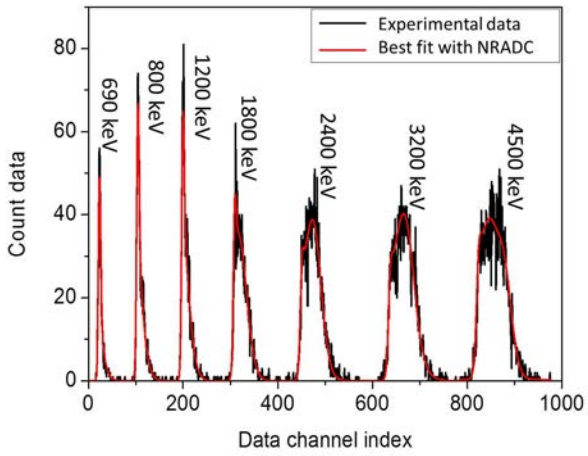

Figure 3.12: Comparison of the experimental data and the best fit to the depth profile from the forward calculation result, each peak corresponding to energies 0.69-4.5 MeV ('W8'-sample)

The measured intensity for all channels is a data vector which is specified as an integral of all deuterium content of separate sublayers according to the coeffi-

cients in the design matrix. The design matrix is generated by attributing a certain deuterium content to the sublayers with SIMNRA and trying to fit it to the experimentally measured profiles. After the calculation of the design matrix, the most probable layout number and optimization of the concentration and layout are found.

In figure 3.12, the experimental proton spectra for sample 'W8' measured with ^3He ion energies in the range 0.69-4.5 MeV, are plotted. All the profiles are plotted versus the data vector index similarly to how it is used during the deconvolution process. From the comparison it is observed a good fit between the experimental data and forward calculation results. The final reconstruction of the deuterium depth profile is done based on these data (see chapter 4). The statistical errors during the NRADC deconvolution are implemented as error bars in the concentration [33].

3.2.5 Thermal Desorption Spectroscopy (TDS)

Thermal desorption spectroscopy (TDS) method is used to estimate the total amount of gas retained in tungsten samples. In principle, the loaded sample is heated up in a vacuum chamber at a certain rate and the released gas is monitored by a mass spectrometer. During the heating process, deuterium atoms gain enough energy to get de-trapped, diffuse in the lattice until they reach the substrate surface where they recombine and are released as molecules. In addition to estimating the total amount of retained gas in the material, the TDS spectra can be used to acquire information on the trapping energy and desorption mechanisms using the release profiles and the relation between the heating temperature ramp and release rate [34]. However, the interpretation of the TDS profiles can be rather challenging due to the uncertainty on the trapping-detrapping mechanisms and diffusion in tungsten (see chapter 2). In figure 4.21, an example of TDS profiles of various tungsten microstructures (SGW, LGW, RECW, SCW[1]) after exposure to high flux deuterium plasma ($\sim 10^{24} m^{-2} s^{-1}$) at about 500 K, is given.

All the samples were heated up in a Carbolite-HST (Horizontal Single Zone Split Tube Furnace) from room temperature to 1273 K (heating ramp ~0.35 K/s)) under vacuum. Due to technical issues, in case of SGW samples it was applied a different temperature ramp ($\sim 0.2 K/s$) but rather linear in the region 300-900 K. A thermocouple was placed in the vicinity of the sample (with no direct contact) inside the quartz tube to monitor the temperature during desorption. The desorbed deuterium was measured with a quadrupole mass spectrometer (Pfeiffer) monitoring the masses 1-50 amu. The contribution of masses 3 (HD), 19 (HDO) and 20 (D_2O) were below 10% of the D_2 peak therefore the mass 4 (D_2) was considered only in the calculations of the total deuterium retention. The calibration of

[1] Small Grain Tungsten, Large Grain Tungsten, Recrystallized Tungsten, Single Crystal Tungsten

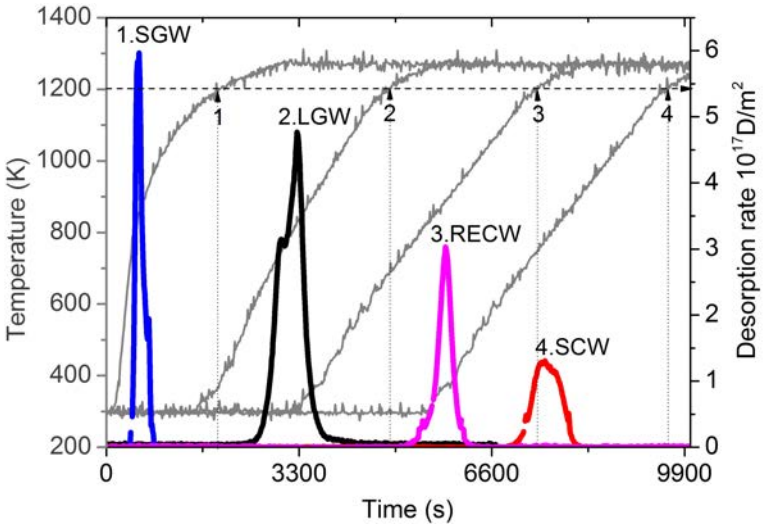

Figure 3.13: Thermal desorption spectroscopy profiles of various tungsten microstructures after exposure to high flux deuterium plasma ($\sim 10^{24} m^{-2} s^{-1}$) at about 500 K

the mass spectrometer was done by measuring the signal of a deuterium leak with a previously known leak rate. The natural background signal of deuterium was measured at room temperature while the sample was in the furnace. This signal was then subtracted from the measured data during the thermal desorption while the background pressure of the TDS setup was kept at $3 \cdot 10^{-8}$ mbar. TDS results of the samples which showed no release peak, were analyzed and their desorption fluence was of the order of 10^{15} D/m^2. This amount of released deuterium was considered as detection limit (no deuterium content) for the present work measurements. It is appropriate to be noted at this point that, after exposure, samples were stored in air for a few weeks, before TDS measurements were done. Therefore, release over several weeks of air storage can be as large as $\sim$65% of the initial deuterium retention [35].

3.3 Sample preparation

Tungsten with four different microstructures was used in the experiments to investigate the role of grain boundaries and intrinsic defects on surface modifications and deuterium retention. The two first set of samples, polycrystalline SGW-small grain tungsten and LGW-large grain tungsten, were exposed to the plasma "as received" from the manufacturer. Tungsten grade used in the experiments was chosen according to the specifications approved for the ITER material selection [36]. Polycrystalline samples were supplied by Negele Hartmetall GmbH [37]. They

were cut in discs with a diameter of 14 mm and 4 mm thickness. Prior to cutting, tungsten of a purity of 99.94% was rolled in rods of 20 mm in diameter with grains elongated parallel to the plasma exposed surface to insure a better heat transport and prevent delamination [38]. A more detailed description of the material chemical composition and physical properties is included in appendix A.1.

In order to ensure consistent and comparable results in terms of surface analysis techniques and gas retention in the material, all tungsten samples were mechanically polished on the surface to a mirror finish (RMS $\leq$40 nm). Afterwards they were ultrasonically cleaned in alcohol and acetone to remove the polishing impurities and subsequently outgassed at $\sim 10^{-6}$ mbar at 1273 K for one hour.

Electron Backscatter Diffraction analysis (EBSD) was performed on the SGW and LGW sample surface to investigate the microstructure, namely the grain size, shape and orientation. In figure 3.14, an EBSD map for two types of samples is given. The difference in grain size originates from the production history of the material and the rolling process. The grains were stretched to a maximum width of about 20 μm and 40 μm respectively, and a length of 200-300 μm. The elongated grains were produced by forging (hammering) the tungsten rods after sintering. The forging of the SGW samples, done at a higher hammering force, produced smaller grains which were distributed more homogeneously. Linear intercept method was used to evaluate the average grain size.

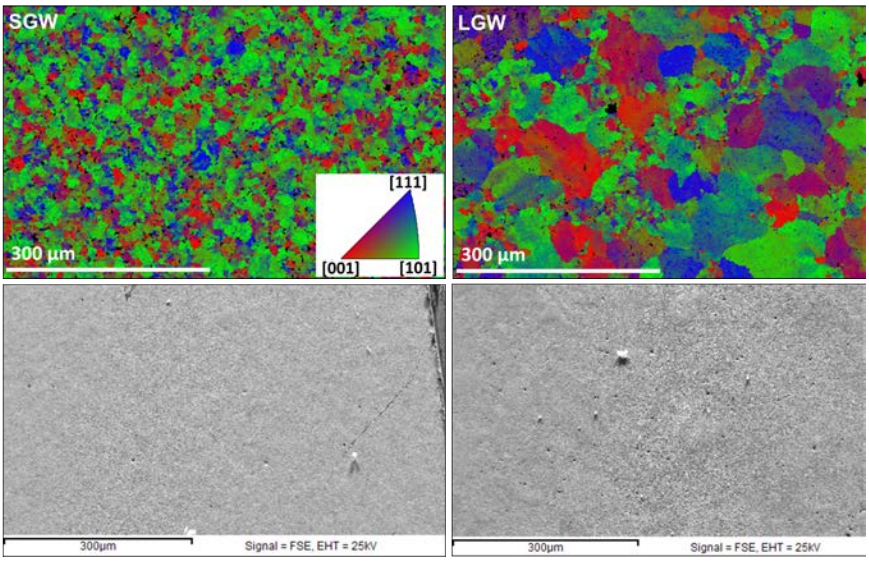

Figure 3.14: Microstructure analysis of the targets used in the experiments performed with the Electron Backscatter Diffraction method (EBSD) to illustrate the grain size, shape and orientation of the grains of Small Grain Tungsten (SGW ∼20 μm) and Large Grain Tungsten (LGW ∼40 μm)

The third set of samples (RECW) was recrystallized at 2273 K for 30 min and resulted in the formation of grains with an average size of $\sim$50 μm in the parallel plane to the plasma exposed surface. The last set consisted of single crystal samples (SCW) which were supplied by Mateck GmbH [39]. They were cut and prepared in a similar way as the other sets of samples. The purity of the material was 99.999% and the crystal orientation (110) had an accuracy of $\leq 0.1^o$. The images of the samples on the surface before the plasma exposure taken with the electron microscope, are given in figure 3.15.

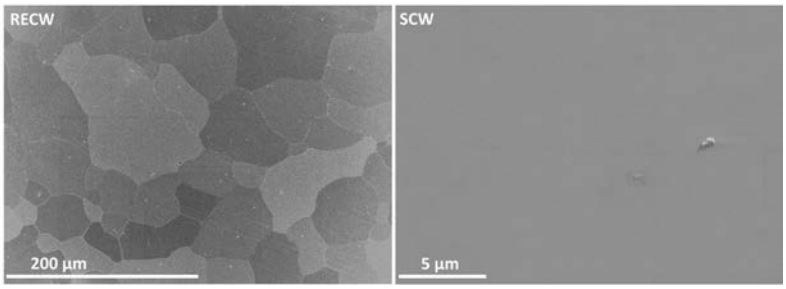

Figure 3.15: Scanning electron microscope image of the recrystallized and single crystal samples taken before the plasma exposure

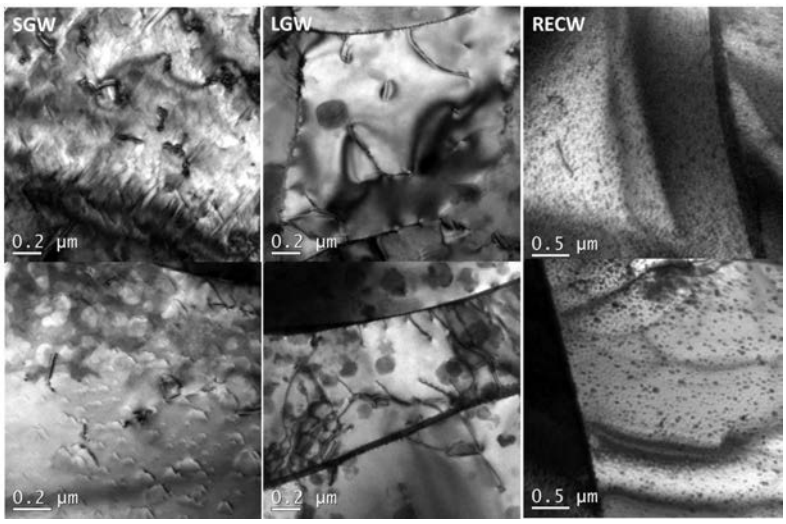

Figure 3.16: Microstructure analysis of the targets used in the experiments performed with the Transmission Electron Microscope (TEM)

An evaluation of the dislocation density and types of defects in the material was done by investigating 1 mm thin polished lamellas with a transmission elec-

tron microscope (JEOL 3010 TEM). This analysis was performed at SCK · CEN lab in Mol. The specimens were cut perpendicular to the exposed surface, mechanically and electrochemically polished using 0.15 wt% $NaOH/H_2O$ at 30 V. Representative TEM images are given in figure 3.16 for LGW, SGW and RECW samples.

TEM analysis on the SGW samples revealed the presence of a random grain size in the range 2-12 μm and average dislocation density $1,28 \cdot 10^{13} m^{-2}$ whereas in case of the LGW samples the observed grain size varied from 0.8 to 10 μm and dislocation density was $2.5 \cdot 10^{13} m^{-2}$. From the TEM analysis it was observed a larger amount of subgrain boundaries in the LGW samples compared to SGW samples. The similar results in terms of dislocation density and grain size for both LGW and SGW samples could originate from the non-homogeneous grain distribution as seen from the EBSD analysis (figure 3.14). However, regarding the recrystallized samples, it was noticed the presence of $\sim$27 μm long visible grain boundaries while the subgrain boundaries were not observed. Dislocations, mainly along the grain boundaries amounting at an average of $\leq 5 \cdot 10^{11} m^{-2}$, were detected.

References

[1] A. Kreter. *et al. Linear Plasma Device PSI-2 for Plasma-Material Interaction Studies*. Fusion Science and Technology, 68(1):8–14, 2015.

[2] G. De Temmerman. *et al. High heat flux capabilities of the Magnum-PSI linear plasma device*. Fusion Engineering and Design, 88:483, 2013.

[3] D.M. Goebel, G. Campbell, and R.W. Conn. *Plasma Surface Interaction experimental facility (PISCES) for materials and edge physics studies*. Journal of Nuclear Materials, 121:277–282, 1984.

[4] Dutch Institute For Fundamental Energy Research The Netherlands. *https://www.differ.nl/*.

[5] W. J. Goedheer. *et al. Magnum-PSI, a Plasma Generator for Plasma-Surface Interaction Research in ITER-like Conditions*. FT/P7-21.

[6] T. Morgan. *et al. A high-repetition rate edge localised mode replication system for the Magnum-PSI and Pilot-PSI linear devices*. Plasma Physics and Controlled Fusion, 56(10pp):095004, 2014.

[7] H. van der Meiden. *et al. Advanced Thomson scattering system for high-flux linear plasma generator*. Review of scientific instruments, 83(123505), 2012.

[8] B. LaBombard. *et al. Presheath profiles in simulated tokamak edge plasmas*. Journal of Nuclear Materials, 162-164:314–321, 1989.

[9] Forschungszentrum Jülich GmbH Germany. *www.fz-juelich.de/*.

[10] B. Unterberg. *et al. New linear plasma devices in the trilateral euregio cluster for an integrated approach to plasma surface interactions in fusion reactors*. Fusion Engineering and Design, 86:17971800, 2011.

[11] O. Waldmann. *Untersuchung der Transportphnomene magnetisierter Plasmen in der Umgebung materieller Limiter*. PhD thesis, Humboldt-University, 2009.

[12] PISCES lab at the University of California in San Diego. *http://www.pisces.ucsd.edu/pisces/*.

[13] D. Nishijima and E. M. Hollmann. *Determination of the optical escape factor in the He I line intensity ratio technique applied for weakly ionized plasmas*. Plasma Physics and Controlled Fusion, 49:791802, 2007.

[14] D. Nishijima, R.P. Doerner, M.J. Baldwin, E.M. Hollmann, R.P. Seraydarian, and Y. Ueda. *Spectroscopic determination of the singly ionized helium density in low electron temperature plasmas mixed with helium in a linear divertor plasma simulator*. Physics of Plasmas, 14(10), 2007. cited By (since 1996)11.

[15] O. Schmitz. *et al. Status of electron temperature and density measurement with beam emission spectroscopy on thermal helium at TEXTOR*. Plasma Physics and Controlled Fusion, 50(115004 (23pp)), 2008.

[16] A. Pospieszczyk. *et al. Helium line emission measurements in PISCES-B as a tool for Te profile determinations in tokamak boundary plasmas*. Nuclear Instruments and Methods in Physics Research, B72:207–223, 1992.

[17] B. Schweer. *et al. Electron temperature and electron density profiles measured with a thermal He-beam in the plasma boundary of {TEXTOR}*. Journal of Nuclear Materials, 196-198:174 – 178, 1992.

[18] R. Doerner. *Private communication*.

[19] W. Zhou. *et al. Fundamentals of Scanning Electron Microscopy*.

[20] A. Bogner. *et al. A history of scanning electron microscopy developments: Towards "wet-STEM" imaging*. Micron, 38:390–401, 2007.

[21] F. J. Humphreys. *Review Grain and subgrain characterisation by electron backscatter diffraction*. Journal of material science, 36:3833 3854, 2001.

[22] T. Maitland. *et al. Electron Backscatter Diffraction (EBSD) Technique and Materials Characterization Examples*.

[23] P. Williams. *Secondary Ion Mass Spectrometry*. Annual Review of Materials Science, 15:517–548, August 1985.

[24] H. W. Werner. *Acoanalysis of SIMS with other ttechnique based on ion-beam solid Interactions*. Vacuum, 34(1-2):83–101, 1984.

[25] F. Ghezzi. *et al. Deuterium depth profile quantification in a ASDEX Upgrade divertor tile using secondary ion mass spectrometry*. Applied Surface Science, 315:459466, 2014.

[26] H. W. Werner. *Theoretical and experimental aspects of Secondary ion mass spectrometry*. Philips Research Laboratories, Eindhoven, The Netherlands.

[27] P. C. Zalm. *Secondary ion mass spectrometry*. Vacuum, 45(6-7):753–772, 1994.

[28] M. Mayer. *et al. Quantitative depth profiling of deuterium up to very large depths*. Nuclear Instruments and Methods in Physics Research B, 267:506512, 2009.

[29] L. G. Earwaker. *Rutherford bacbackscatter and nuclear reaction analysis*. Vacuum, 45(6-7):783–803, 1994.

[30] V. Alimov. *et al. Differential cross-section of the D(3He,p)4He nuclear reaction and depth profiling of deuterium up to large depths*. Nuclear Instruments and Methods in Physics, 234:169175, 2005.

[31] E. Szilagyi. *et al. Theoretical approximations for depth resolution calculations in IBA methods*. Nuclear Instruments & Methods in Physics Research B, 100:103–121, 1995.

[32] M. Mayer. *SIMNRA User's Guide, IPP Report 9/113*. Max-Planck-Institut fuer Plasmaphysik - Garching, Germany,, 1997.

[33] K. Schmid and U. von Toussaint. *Statistically sound evaluation of trace element depth profiles by ion beam analysis*. Nuclear Instruments and Methods in Physics Research B, 281:6471, 2012.

[34] E. Kautto. *et al. Analysing Methods for Thermal Desorption Spectra*. Physica Scripta, 55:628–633, 1997.

[35] K. A. Moshkunov. *et al. Air exposure and sample storage time influence on hydrogen release from tungsten*. Journal of Nuclear Materials, 404:174–177, 2010.

[36] Material Specification for the Supply of Tungsten Bars for the ITER Divertor. *IDM Number: ITER_D_2X38PN v. 1.0*. 2010.

[37] Negele Hartmetall GmbH. *http://www.negele-hartmetall.de/*.

[38] G. Pintsuk. *Tungsten as a Plasma-Facing Material*. Comprehensive Nuclear Materials Konings,R.J.M., Ed.; Elsevier: Amsterdam, The Netherland, page 551581, 2012.

[39] MaTecK Material-Technologie & Kristalle GmbH. *http://www.mateck.de*.

4

Experimental results and discussion

4.1 Deuterium plasma exposure

Four sets of experiments were performed in order to assess the impact of material microstructure on the correlation between particle flux, exposure temperature, surface modifications and deuterium retention in tungsten. The aim of the experiments was to separate the effects of grain boundaries and intrinsic crystallographic defects of the material in deuterium trapping and total inventory. For this reason, single crystal tungsten (SCW, crystal orientation 110), recrystallized (RECW) and "as received" polycrystalline tungsten samples with a grain size of $\sim$20 μm (SGW) and $\sim$40 μm (LGW) were exposed to D plasma in Pilot-PSI and PSI-2 linear plasma devices (see appendix A for W specifications [1]). On one hand, single crystal tungsten has a low dislocation density and grain boundaries are not present. On the other hand, recrystallization at high temperatures causes grain growth and decreases the dislocation density to negligible levels allowing identifying the role of grain boundaries in deuterium trapping and diffusion. Investigated surface temperature was in the range 510-1170 K and deuterium ion fluxes varied within two orders of magnitude (low flux: $10^{22}\ m^{-2}s^{-1}$, high flux: $10^{24}\ m^{-2}s^{-1}$). Ion energy of 40 eV (below the physical sputtering threshold), and particle fluence of $10^{26}\ m^{-2}$, were kept constant in all the experiments. Experimental data will be discussed separately for each type of material and in the last section, a discussion of the results based on the CRDS modeling, will be included.

4.1.1 Small Grain Tungsten (SGW)

After exposure to deuterium plasma, surface modifications were investigated with an electron microscope at the center of the sample, which coincides with the maximum of plasma flux density. After low flux density exposures at 510 K, the blister size amounted to 1-2 μm with areal density $\sigma_A \sim 10^{12}\ m^{-2}$ while at 670 K blisters were smaller than 0.5 μm and the corresponding density was higher $\sigma_A \sim 4 \cdot 10^{12}\ m^{-2}$. At 870 K stratified layers were found, the direction of which depends on the grain orientation. Similar structures were observed from Balden *et al.* [2] after exposure of tungsten to deuterium plasma at an ion flux of $10^{20}\ m^{-2}s^{-1}$ at 500 K surface temperature. The authors speculated for a possible sputtering process from the impurities present in the plasma. Meanwhile, at 1070 K, no blisters were detected (see figure 4.1).

Three types of surface modifications were detected on the SGW sample, exposed to high flux density at 510 K (4.1.a1): porous structures (1), ripples (2) and blisters only at the grain boundaries (3). At 670 K blisters with a diameter smaller than 0.5 μm ($\sigma_A \sim 3 \cdot 10^{12}\ m^{-2}$) appeared. At 870 K larger blisters were detected with a size of 0.05-1.5 μm ($\sigma_A \sim 10^{12}\ m^{-2}$), decreasing in size to 0.05-0.5 μm at 1170 K ($\sigma_A \sim 4 \cdot 10^{12}\ m^{-2}$). From the literature it is known that blistering is suppressed at higher temperatures than 700 K, therefore, blister formation in this case was not expected. Xu *et al.* [3, 4] found similar blisters which were formed on their tungsten samples after exposure to deuterium plasma in Pilot-PSI at high flux ($\sim 10^{24}\ m^{-2}s^{-1}$) and surface temperature in the range ~470-520 K. The authors attributed the formation of similar structures to the extreme plasma loading conditions in terms of particle flux and ion energy.

It has been proposed that blisters are formed from specific kind of defects in the material such as vacancies, interstitials, and dislocations which act as traps for deuterium [5]. The binding energies of deuterium in these traps and the total deuterium retention can be calculated by analyzing the shape and peak temperature of the TDS spectra [6]. To illustrate, in figure 4.2 desorption data of deuterium during the heating up of the tungsten samples are shown. Desorption flux of $10^{15}\ Dm^{-2}$ is considered as a detection limit. The TDS measurements of all samples were performed at similar heating rate. Deuterium desorption profiles from time and the temperature ramp are plotted in appendix B.1.

After exposure to low flux density deuterium plasma, a desorption peak was observed at low exposure temperature $(510K, 670K)_{LF}$ while at higher exposure temperature $(870K, 1070K)_{LF}$ the deuterium release was negligible (4.2, SGW LF). Desorption started at around 650-700 K for the samples exposed at 510 K and 670 K, and had a single peak at 963 K and 965 K respectively, with a broader shoulder at higher temperature in the latter case.

Heating of the SGW samples, exposed at high flux density deuterium plasma, showed desorption peaks, independently of the exposure temperatures (4.2, SGW

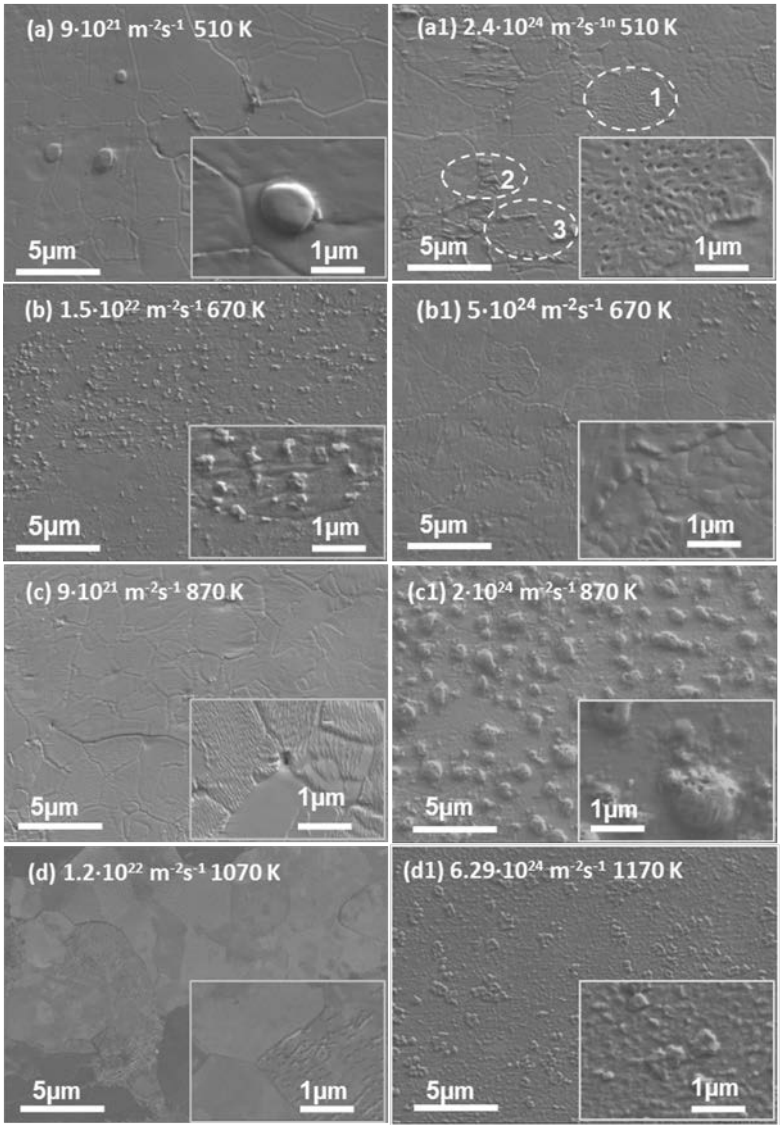

Figure 4.1: SEM images taken on the SGW samples after exposure to D plasma at PSI-2 (a)-(d) and Pilot-PSI (a1)-(d1) at a fluence of $10^{26}\ m^{-2}$ *and incident ion energy of 40 eV.*

HF). Deuterium desorption of the samples $(510K, 670K)_{HF}$ started at similar heating temperature as in the low flux case, at 650-700 K and had two similar peaks, at around 850 and 930 K.

The peak height in the high flux case was about two orders of magnitude lower compared to the low flux exposures. SGW sample exposed at $(870K)_{HF}$ revealed

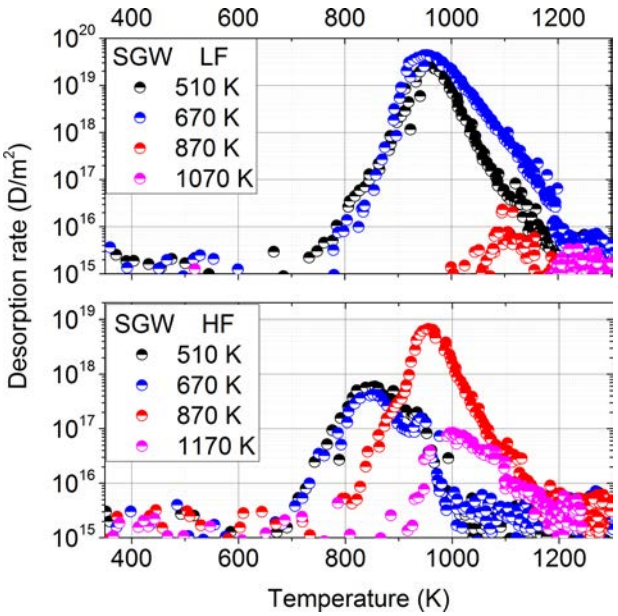

Figure 4.2: TDS profiles of SGW samples exposed at low flux density (LF) and high flux density (HF) pure deuterium plasma

a peak at 965 K and a shoulder at around 850 K while the sample exposed at a higher temperature $(1170K)_{HF}$, showed two release peaks, at 1005 K and 1100 K.

From the TDS graphs, a similar effect in terms of peak height and number of peaks when considering $(510K, 670K)_{HF}$, $(510K, 670K)_{LF}$ (black and blue curves) and $(870K)_{HF}$, $(1170K)_{HF}$ (red and magenta curves) is observed. Increasing the particle flux $[(510K, 670K), LF \rightarrow HF]$ and increasing the exposure temperature $[870K \rightarrow 1170K, HF]$ produced two peaks instead of one with a two orders of magnitude lower peak height. The number of peaks and their shape is generally related to the number of trapping sites with various activation energies, depth distribution of traps, diffusion of released deuterium and re-trapping in the bulk as well as the desorption from the back side of the sample. A summary of the exposure conditions and TDS peak temperatures is given in table 4.1.

Deuterium depth profiles were measured on the SGW samples with SIMS (4.3, top left and right graphs) and NRA (4.3, bottom left and right graphs). From SIMS measurements it was observed that the samples exposed at high flux density $(870K, 1170K)_{HF}$ had a relatively steep profile of deuterium concentration in the first 200-300 nm as opposed to the low flux density $(870K, 1070K)_{LF}$ where the deuterium profile was more flat. This was confirmed also from the NRA measurements where a flat profile of deuterium was observed in case of low flux exposures.

Sample name	Surface T (K)	Ion flux $(m^{-2}s^{-1})$	Exposure time (s)	T_{peak} (K)
SGW (PSI-2)				
W8	510	9E21	11111	963
W1	670	1.5E22	6667	965
W9	870	9E21	11111	-
SGW24	1070	1.2E22	8334	-
SGW (Pilot-PSI)				
W10	510	2.4E24	42	852, 930
W11	670	5E24	20	850, 925
W12	870	2E24	50	965
W22	1170	6.29E24	16	1005, 1100

Table 4.1: Exposure conditions of SGW samples and results on the areal density of blisters and TDS peak temperature

Deuterium retention dropped from 10^{-2} to 10^{-3} at.fr in the first $\sim$0.5 μm in both cases corresponding to high and low particle flux density. While for the samples $(510K, 670K)_{LF}$, deuterium concentration remained at a value of $\sim 10^{-3}$ at.fr at a depth $>1\mu$m, it decreased further down to $\sim 10^{-4}$ at.fr at a depth up to 3 μm for samples $(510K, 670K)_{HF}$. Deuterium depth profile of the sample $(870K)_{LF}$ was similar to the implantation profile at low particle flux density exposure, in addition to the resemblance of the TDS profile. In the high flux density and high exposure temperature case, deuterium diffused deeper into the material and could be trapped in the defects which become mobile at high temperatures.

At this point, it is pertinent to remind that, in order to accumulate the required ion fluence of 10^{26} m^{-2}, samples were exposed to low flux density for approximately 3 hours. At temperatures up to 670 K, deuterium diffused deeper in the material due to the longer exposure time compared to the high flux density case $(10^{24}m^{-2}s^{-1})$, where the exposure time was shorter than 50 s. This leads to a larger amount of solute deuterium retained in the sample which could be trapped in the defects and initiate blister formation. Furthermore, the exposure of tungsten to high particle fluxes creates additional defects in the near surface region. This was confirmed by positron annihilation spectroscopy measurements on Pilot-PSI samples from Xu *et al.* [4]. The population of those plasma induced defects, can increase the amount of deuterium in the first 200 nm, as indicated from the SIMS measurements.

The total amount of retained deuterium from the NRA and TDS measurements, as a function of exposure temperature and particle flux density, is plotted in figure 4.4. The discrepancy between the NRA and TDS results originates from the limitations of the ion beam analysis to probe at larger depths. As seen from figure 4.3, the NRA measurements were limited at a depth of about 9 μm while deuterium

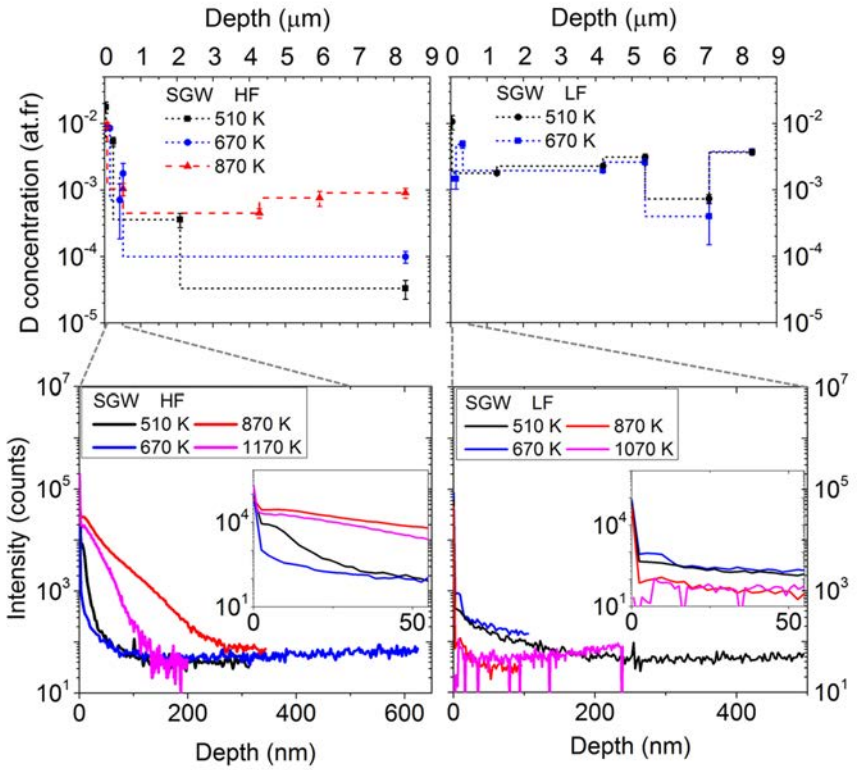

Figure 4.3: Deuterium depth distribution profiles in tungsten as measured with NRA (top) and SIMS (bottom) techniques

could diffuse deeper. This results in larger amount of total deuterium in tungsten detected from TDS. However, at high flux density exposures it is not always the case, namely, at low temperatures, NRA measurements show larger amount of deuterium than TDS. This could come from the fact that NRA measurements were done at a location with higher deuterium content, and the integral over the whole sample yields an overestimated value. Alternatively, the time lag of a few months between NRA and TDS measurements, considering the highest deuterium concentration at the near surface region, could have allowed deuterium to desorb at room temperature. The total retention at low temperatures and flux $(510K, 670K)_{LF}$, was up to two orders of magnitude higher compared to high flux exposure while a reversed situation was observed at higher temperatures. Very low amount of deuterium, nearly at the limit of the TDS detection ($\sim 10^{18}\ m^{-2}$) were measured at higher temperatures at low flux $(870K, 1070K)_{LF}$.

The total deuterium retention at low flux density exposure at ~500 K was com-

parable to previous data from Alimov *et al.* [7] while at higher temperatures the retention was higher in the present experiments. The discrepancy could be a result of the differences in sample preparation and production history of tungsten samples [8]. The maximum of retention for low flux was at an exposure temperature of ∼630 K and for high flux was at ∼870 K which means that the exposure temperature at which the retention is maximal increases for higher fluxes. Previous investigations at even lower flux density ($\sim 10^{20}\ m^{-2}s^{-1}$) confirmed the same behavior with a temperature corresponding to the maximum retention at ∼400 K [9].

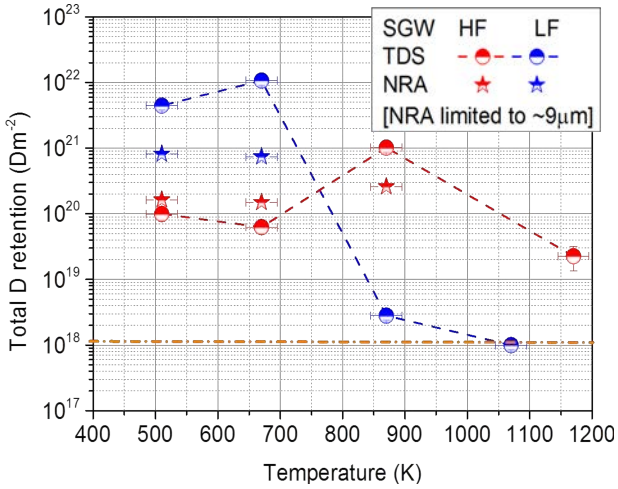

Figure 4.4: Total deuterium retention for SGW samples exposed to two different particle flux density ($\sim 10^{22}\ m^{-2}s^{-1}$ *and* $\sim 10^{24}\ m^{-2}s^{-1}$*) at 40 eV of incident ion energy and* $10^{26}\ m^{-2}$ *total fluence as given from TDS and NRA measurements.*

Summarizing the experimental observations for SGW samples, at the given plasma fluence, deuterium retention and blister formation in tungsten were strongly depending on the plasma flux density and the surface temperature during exposure. At low temperatures, deuterium retention was higher at low flux density because the exposure time was longer and the temperature gradient perpendicular to the surface was smaller which leads to deeper diffusion of deuterium. The deeper diffusion was confirmed by a shift of the TDS peak towards higher temperatures and with the longer desorption time, in addition to the depth profiles. At high temperature, results showed deuterium retention to be higher at high flux density due to implantation of deuterium at the induced traps, compared to low flux density where deuterium is thermally desorbed during irradiation.

4.1.2 Large Grain Tungsten (LGW)

Similar to previous results, in terms of surface modifications, were observed on the LGW samples. Scanning electron microscope imaging, on the samples exposed to low particle flux densities at 530 K, revealed blisters of a few micrometer which were present at a lower concentration ($\sigma_A \sim 4 \cdot 10^8\ m^{-2}$) compared to the high flux exposure (figure 4.5.a). These structures were rarely distributed on the surface and their flat-top shape has been reported previously [10]. On the sample exposed to 630 K at low flux (figure 4.5.b), the presence of two types of blisters was detected $\sim$2 μm and $\sim$40-100 nm, whereas at 870 K and 1140 K the surface was not modified (figure 4.5.c and d).

In case of exposure to high particle flux densities, two types of blisters were observed. At 530 K, small nanostructures of 20-30 nm diameter (figure 4.5.a1) and large ones of $\sim$0.1-1 μm ($\sigma_A \sim 10^{13}\ m^{-2}$) were detected. A clear dependence of blister distribution on grain orientation was observed on the modified surface which could be attributed to the plastic deformations as a consequence of high local stresses [3]. With surface temperature increasing to 630 K, the density of large blisters decreased ($\sigma_A \sim 5 \cdot 10^{12}\ m^{-2}$) and the size of small blisters increased to $\sim$40 nm (figure 4.5.b1). A cross-sectional cut using focused ion beam (FIB) showed the presence of voids a few tens to hundreds of nanometers below the surface (figure 4.6.B1 and B2). The high particle flux density exposure at 870 K and 1170 K (figure 4.5.c1 and d1) revealed only small blisters of up to a few hundreds of nanometers. The blister size increased to about 200 μm at 1170 K and density amounted up to $\sigma_A \sim 2 \cdot 10^{12}\ m^{-2}$.

In figure 4.6, higher resolution SEM images of samples exposed to high particle flux density are given in order to show more clearly the presence of the nanostructures. The grain marked by a 'x' sign in the figure (figure 4.5.a1) and (figure 4.6.A) was modified by the presence of very small nanostructures of the order of a few tens of nanometer, resembling a spongy structure. At 630 K (figure 4.6.B), the small nanostructures became more visible as their size increased whereas density decreased. At 870 K (figure 4.6.C) two types of blisters were observed, blisters in the tens nm-range and blisters in the hundred nm-range as indicated with the red circles [3]. Their density decreased and the size increased to about $\sim$50 nm with increasing temperature. Only one type of blisters were observed at 1170 K at high particle flux. Their size reached up to a couple of hundreds of micrometers and the shape was rather flat at the top.

The blister diameter as a function of exposure temperature and incident flux density is depicted in figure 4.7, showing consistent results for both sets of experiments (LGW and SGW). At low exposure temperature (i.e. up to 700 K), the blister diameter decreased with increasing flux density while at high exposure temperature blisters were absent at low flux density and they were present at high flux density. Based on previous investigations performed at low particle flux (up to

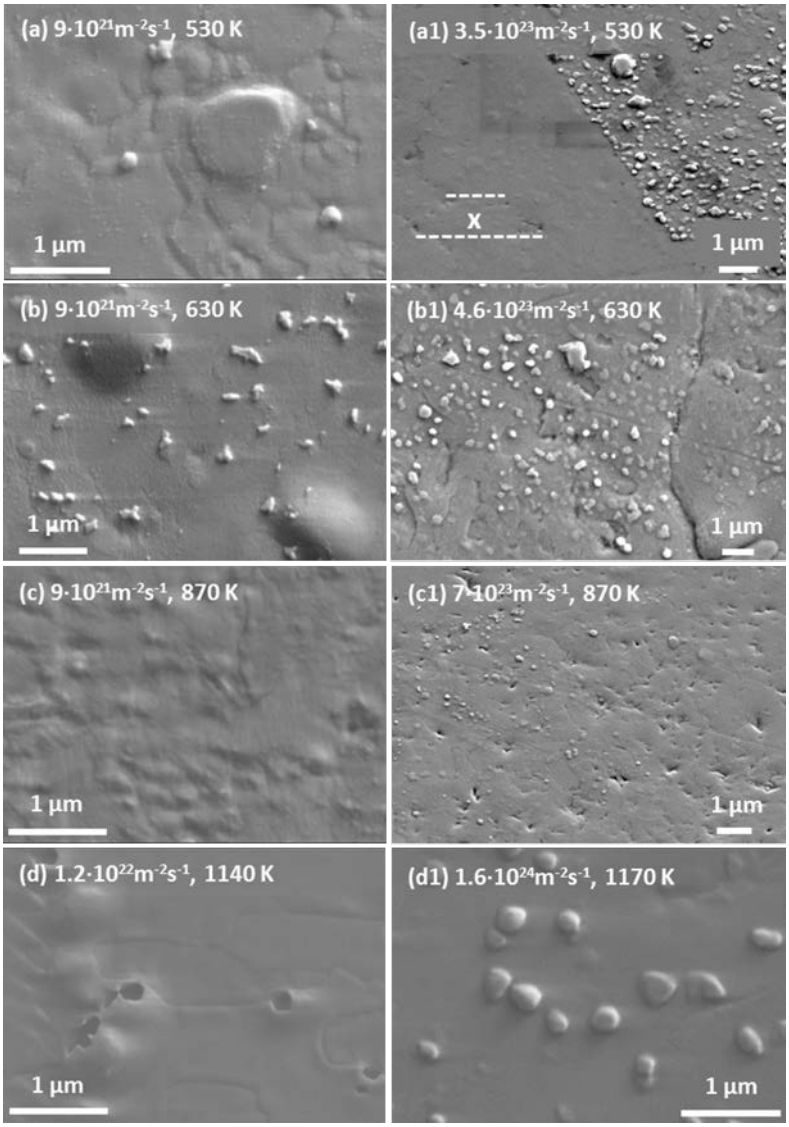

Figure 4.5: SEM images of the Large Grain Tungsten samples (LGW) after exposure at ion fluence $10^{26}\ m^{-2}$; (a)-(d) are the low flux exposures and (a1)-(d1) are the high flux exposures at the respective surface temperatures.

$10^{22}\ m^{-2}s^{-1}$) [11–13], neither surface modifications nor deuterium retention are expected at high temperatures. SEM and TDS results (figure 4.1 and 4.2) showed that the presence of blisters at low ion flux exposure ($10^{22}\ m^{-2}s^{-1}$) was correlated to the deuterium retention meaning that the blisters were present when a

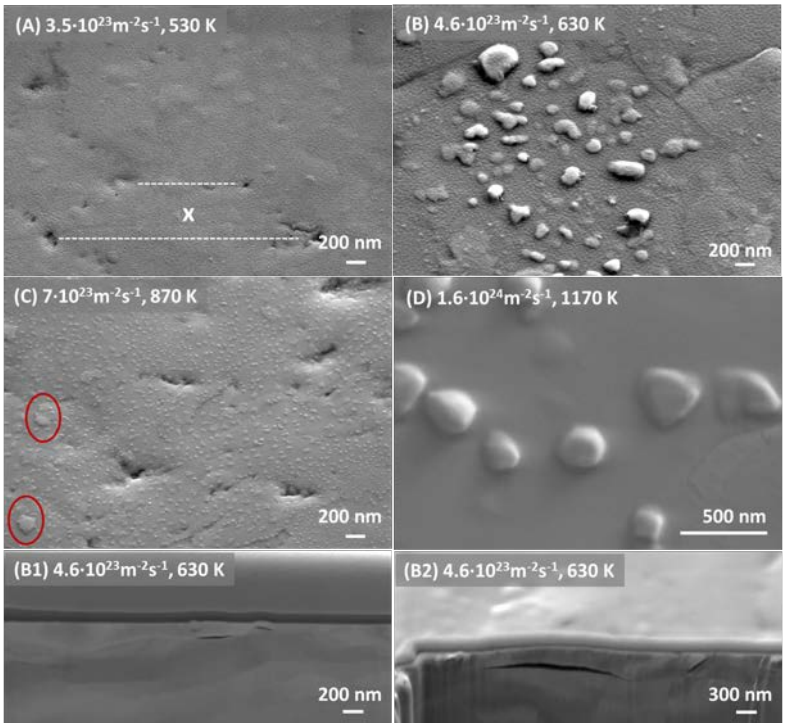

Figure 4.6: (A-D) Higher magnification SEM images of samples after exposure at high flux. At 870 K, two types of blisters were present; blisters in the tens nm-range and blisters in the hundred nm-range as indicated with red circles. (B1) and (B2) are the FIB - cross sectional cut images after exposure to high particle flux at 630 K.

higher amount of the deuterium retention was measured and were missing when the retention was low.

As seen from the graph 2.12, no surface changes are expected for temperatures higher than 700 K. In the present experiments, it is important to be emphasized the presence of small blisters (40-50 nm) at elevated particle flux densities and temperatures. These nanostructures were first observed by H.Y. Xu *et al.* [4] at low temperatures and recently confirmed also by Y.Z. Jia *et al.* [14]. These findings demonstrate a clear dependence of surface morphology changes of tungsten under deuterium particle impact on surface temperature and particle flux density.

Deuterium content in the samples was measured with thermal desorption spectroscopy (TDS) technique. In figure 4.8, the TDS spectra of LGW samples as a function of the desorption temperature are given.

The TDS spectrum of samples exposed at 530 K at high particle flux density had a peak at 840 K and a shoulder at 730 K (figure 4.8). This indicates the presence of more than one type of traps with different binding energies. On the other

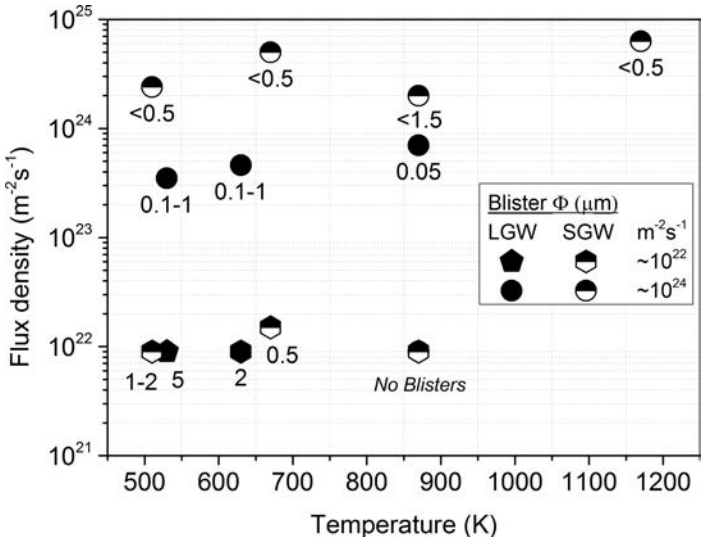

Figure 4.7: Blister diameter (Φ) is given as a function of exposure temperature and incident flux density for two sets of experiments, large and small grain tungsten samples (LGW, SGW)

hand, the deuterium desorption from the sample exposed at 530 K at lower flux density had a single peak temperature at around 875 K. The desorption profile of deuterium from the sample exposed to high particle flux density at 630 K resembled the variations of the temperature profile which was not entirely linear in the range 600-800 K as a result of a failure of the TDS setup during the measurements. The largest amount of deuterium from the sample exposed at high particle flux at 870 K was released at around 865 K in a single peak whereas, deuterium retention at 870 K was insignificant for the exposure at lower flux density. In table 4.2 are given the exposure conditions and TDS peak temperatures for each case.

Both LGW and SGW samples showed a single TDS desorption peak at low exposure temperature and low flux, and two peaks at high flux indicating the presence of two or more trapping sites with different energies. On one hand, the peak desorption temperatures were higher at low flux exposures compared to the high flux at low exposure temperatures. On the other hand, the TDS temperature peaks were higher ($\sim$100 K) for SGW compared to LGW samples which could originate from the fact that the grain boundaries as well as the larger amount of intrinsic defects (due to the mechanical treatment) increase the total number of trapping sites [15].

The integrated amount of deuterium from the TDS profiles is given in figure 4.9. In the graph are included also the NRA measurements which were measured at one single energy ($\sim$1.2 MeV) probing a depth up to $\sim$1 μm, clearly much

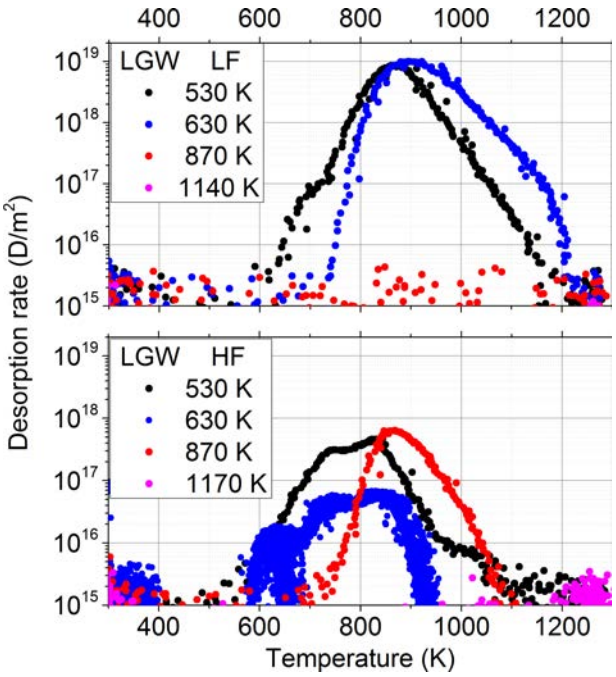

Figure 4.8: TDS spectra of desorbed deuterium from samples exposed to low ($\sim 10^{22} m^{-2} s^{-1}$) and high ($\sim 10^{24} m^{-2} s^{-1}$) particle flux density.

Sample name	Surface T (K)	Ion flux $(m^{-2}s^{-1})$	Exposure time (s)	T_{peak} (K)
LGW (PSI-2)				
W2	530	9E21	11111	875
W4	630	9E21	11111	895
W3	870	9E21	11111	-
LGW15	1140	1.2E22	8334	-
LGW (Magnum-PSI)				
$Nr.6\_140213$	530	3.5E23	286	730, 840
$Nr.5\_140213$	630	4.6E23	217	730, 880
$Nr4\_140213$	870	7E23	143	865
LGW6	1170	1.6E24	63	-

Table 4.2: Exposure conditions of LGW samples and results on the areal density of blisters and TDS peak temperature

shallower than the real deuterium diffusion depth. Similarly as in SGW samples, the total amount of desorbed deuterium for the low flux density cases are in a good agreement with the data provided by Alimov *et al.* [7]. Deuterium retention

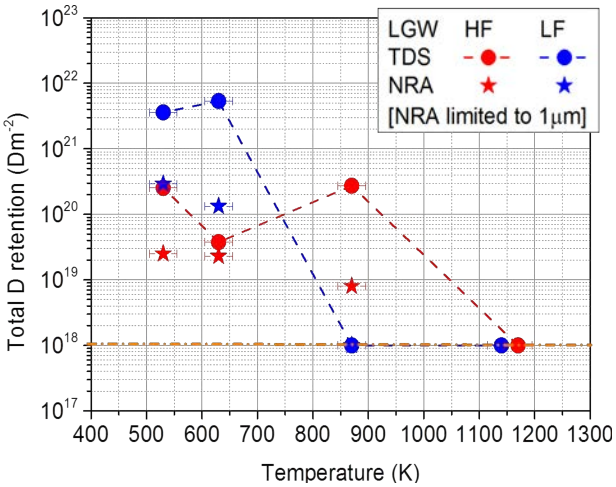

Figure 4.9: TDS and NRA results on total deuterium retention in tungsten samples as a function of surface temperature, exposed to a fluence of $10^{26}\ m^{-2}$ *and various surface temperatures. The blue and red curves represent the exposures to low and high flux density respectively.*

at 530 K and 630 K is higher for low flux exposures due to the temperature and time dependence of diffusion [16]. Shorter exposure time at Magnum-PSI compared to PSI-2, leads to lower diffusion of deuterium at low temperature. The total deuterium retention at high particle flux density and high temperature exposure (870 K) is higher because deuterium is implanted into the sample and trapped due to a faster and more intensive process as a result of a much higher particle flux density. Deuterium retention at low flux density and high temperature (870 K) decays due to the thermo-desorption of deuterium from the defects. The absence of deuterium in tungsten under these conditions prevents the surface modification, as confirmed previously by Alimov *et al.* [11]. The total deuterium retention for LGW was smaller than for SGW at low exposure temperature and low flux and the trend reversed for high exposure temperature. The opposite of the aforementioned behavior was observed in the case of high flux exposures.

To summarize, the experiments with SGW and LGW samples showed that the surface modifications and deuterium retention depend strongly on the exposure temperature and ion flux density. Surface modifications depend on the material microstructure while the deuterium retention differs with about one order of magnitude, depending on the temperature range. However, the same variation trend of total deuterium retention with ion flux and exposure temperature was observed independently on the material microstructure. It was shown that the maximum of deuterium retention depends on the incident ion flux at a given fluence and ion energy. It increases with increasing the ion flux. From the TDS measurements was

observed that the maximum of deuterium retention for low flux density ($\sim 10^{22}$ $m^{-2}s^{-1}$) was reached at ~630 K and for high flux density ($\sim 10^{24}$ $m^{-2}s^{-1}$) was at ~870 K. Neither deuterium nor surface modifications were found on the sample exposed to low flux at above 870 K. As a result of a longer exposure time, deuterium diffused to a deeper range in the material at low temperature while it thermally desorbed at higher temperatures (870 K). In the high flux case deuterium diffused deeper due to the high temperature and the higher rate of defects production by the plasma irradiation process. In addition, the concentration of solute deuterium in the implantation zone is higher compared to the low-flux exposure, leading to a higher fraction of occupied traps than that in the case of low flux exposure. Thermal desorption temperature peaks were generally higher for SGW compared to LGW samples, suggesting that the grain boundaries (plus a higher amount of existing intrinsic defects) increase the total number of the trapping sites. The total deuterium retention followed the same trend for both grain sizes: higher total retention for low flux exposure compared to high flux exposure at $T < T_{peak}$ and a reversal of this trend at $T > T_{peak}$ (T_{peak} is the exposure temperature at which the retention is maximal).

4.1.3 Recrystallized Tungsten (RecW)

In the light of decreasing further the amount of intrinsic defects in the material, recrystallized samples at 2273 K were exposed to pure deuterium plasma at similar conditions. From the SEM scanning, it was observed that blistering occurred only at low particle flux density and low exposure temperature of 520 K (figure 4.10). Blisters had a diameter of 10-20 μm and a flat top surface. From the cross-sectional cut with the focused ion beam, cracking along the grain boundary, starting at a depth of 4 μm extending up to 16 μm, was observed (figure 4.11).

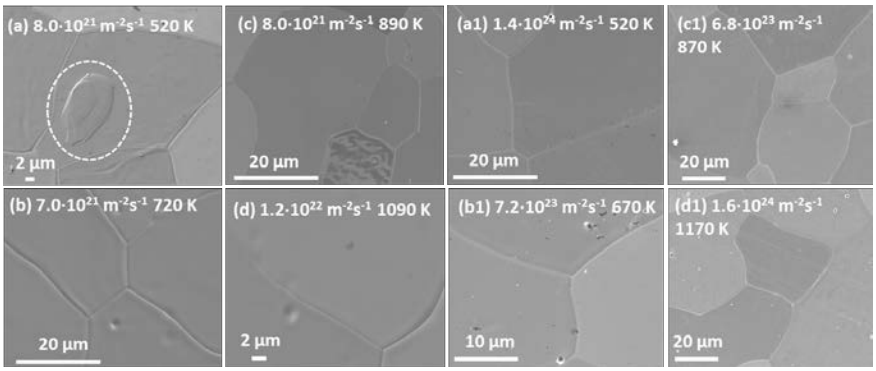

Figure 4.10: SEM images taken on the RecW samples after exposure to D plasma at PSI-2 (a)-(d) and Pilot-PSI (a1)-(d1) at a fluence of $10^{26} m^{-2}$ and incident ion energy of 40 eV.

Alimov *et al.* [7] found similar flat-top blisters on his recrystallized tungsten samples (rec. at 2073 K) after exposure to similar plasma conditions at 595 K. While Balden *et al.* [2] referred to these surface modifications as extrusions, he found them to appear at a rather low areal density after exposure to 500 K and ion flux of $10^{20}\ m^{-2}s^{-1}$.

Deuterium diffusion is enhanced by the presence of grain boundaries whereas trapping slows it down [17]. When the local concentration of deuterium in bulk material exceeds the solubility limit, overpressurized gas filled cavities are formed, which tend to release the stress by pushing dislocations to the grain boundaries. The dislocation motion in the crystal is carried out through the lattice planes in a certain direction which is most favorable energetically. This leads to plastic deformation in the material, crack formation and agglomeration of deuterium at the grain boundaries [18].

Blistering is dependent on the plasma loading conditions which also influence the deuterium depth profile in the metal. From the NRA measurements (figure 4.12), it can be inferred that deuterium content was distributed in three main regions: (i) up to 0.5 μm there was a drop from the surface content to $3 \cdot 10^{-4}$ at.fr and $\sim 6 \cdot 10^{-5}$ at.fr for the case $(520K)_{LF}$ and $(520K, 670K)_{HF}$ respectively, (ii)

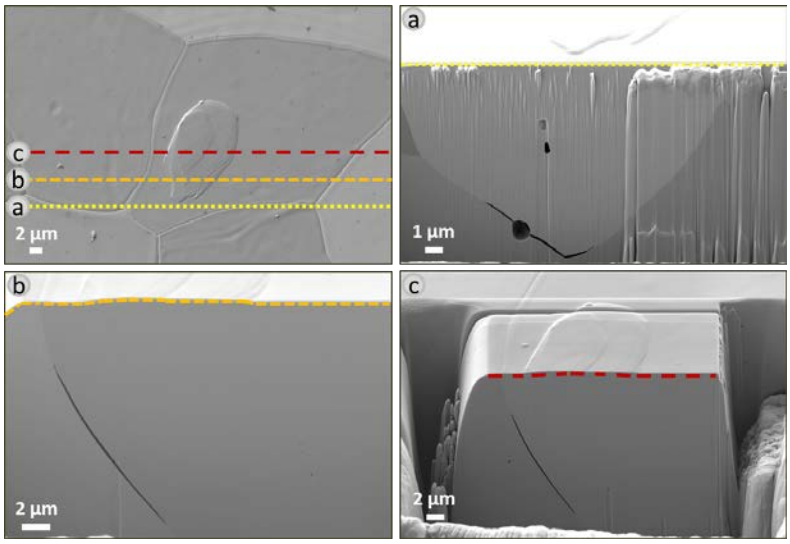

Figure 4.11: SEM images taken on the RecW sample after the cross-sectional cutting of one of the blisters with the focused ion beam (FIB)

0.5-4 μm the deuterium concentration varied in the range $\sim 6 \cdot 10^{-5} - 3 \cdot 10^{-3}$ at.fr, (iii) and the bulk >4 μm. Similar profiles have been identified in earlier publications [19].

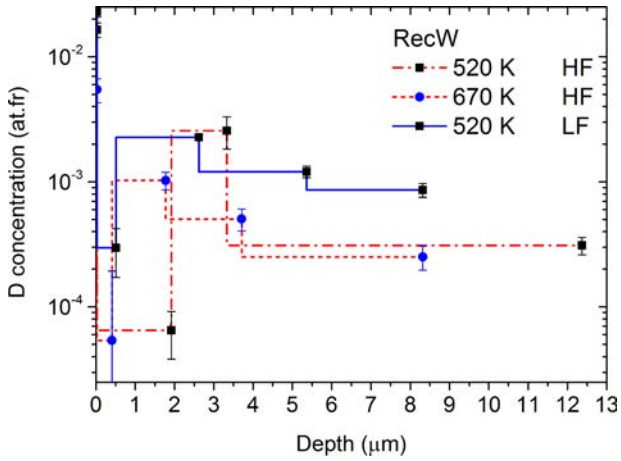

Figure 4.12: Deuterium depth distribution profiles in recrystallized tungsten samples as measured with the NRA technique

As seen from the graph 4.12, deuterium concentration dropped in the first 0.5 μm. It will be shown from the CRDS simulations that the concentration drop in the

first 0.5 μm for the samples $(520K)_{LF}$ and $(670K)_{HF}$, may have occurred due to an artifact during NRADC deconvolution. In the second region 0.5-4 μm, deuterium concentration was higher in the sample exposed to low flux and low temperature $(520K)_{LF}$ compared to the high flux cases. Up to 2 μm in depth, there was a 25 times larger deuterium content in $(520K)_{LF}$ compared to $(520K)_{HF}$. A higher inventory in this region could serve as a more efficient source of deuterium diffusing into the bulk. When the solubility and diffusivity reached the limits, blister nucleation and cracking at the grain boundaries may appear. Also in this case, the exposure conditions and TDS peak temperatures are summarized in table 4.3.

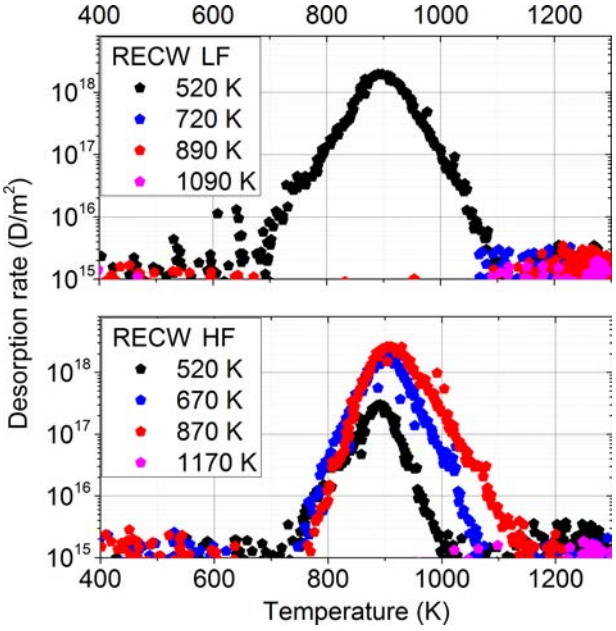

Figure 4.13: TDS spectra of desorbed deuterium from the recrystallized tungsten samples exposed to low ($\sim 10^{22}\ m^{-2}s^{-1}$) and high ($\sim 10^{24}\ m^{-2}s^{-1}$) particle flux density.

Another indication on the deuterium depth profile and trapping in the material was delivered from the TDS measurements. In the graph 4.13, one single release peak for all the samples exposed to high and low particle flux, was detected. The desorption peak temperature of sample $(520K)_{LF}$ was at 887 K while at high flux exposures $(520K, 670K, 870K)_{HF}$ the release temperatures had a maximum at 886 K, 865 K and 905 K, respectively. Samples $(520K)_{LF}$ and $(520K)_{HF}$ revealed an almost identical desorption peak temperature with the difference that the desorption in the former case started at lower temperatures (at $\sim$650 K) compared to the latter case (at $\sim$730 K), it ended at a higher temperature and had a ten times higher desorption peak. These measurements suggest for a deeper diffusion of

Sample name	Surface T (K)	Ion flux $(m^{-2}s^{-1})$	Exposure time (s)	T_{peak} (K)
RECW (PSI-2)				
RECWJ1	520	8E21	12500	887
RECWJ2	720	7E21	14286	-
RECWJ3	890	8E21	12500	-
RECWJ4	1090	1.2E22	8334	-
RECW (Pilot-PSI)				
RECW1	520	1.4E24	71	886
RECW2	670	7.2E23	139	865
RECW3	870	6.8E23	147	905
RECW4	1170	1.6e24	63	-

Table 4.3: Exposure conditions of RECW samples and results on the areal density of blisters and TDS peak temperature

deuterium into the bulk material in the case of low flux exposure. As it is seen also in the graph 4.14, the total amount of deuterium retained at the exposure conditions $(520K)_{LF}$ was about ten times higher than $(520K)_{HF}$ case. Under these conditions, one may presume the diffusion length in the material to be scaled as the square root of time. In these experiments, the exposure time had a difference of two orders of magnitude.

Deuterium release of the samples exposed to high particle flux density $(520K, 670K, 870K)_{HF}$ started at a temperature range of 730-770 K at an increasing order according to the exposure temperature. These profiles showed an increase of deuterium diffusion with temperature, indicating the negligible role of trapping-detrapping process of deuterium in the lattice and its enhancement through the grain boundaries. From the literature research it was found that the peak height of sample $(520K)_{LF}$ was about three times lower compared to Alimov *et al.* [7] experiment, and the desorption peak temperature was ∼40 K higher. There was a very good compatibility of the total deuterium retention with Alimov *et al.* [7] results at $(520K)_{LF}$ while at $(720K)_{LF}$ Alimov found a total retention of 2×10^{19} Dm^{-2}. This discrepancy could be attributed to the different scale of material recrystallization, leading to a lower defect density.

In the graph 4.14 is evident the temperature at which the deuterium retention had a maximum; it happened at around 500 K and 900 K at low and high flux respectively. In the low flux case, a rather high amount of deuterium was retained while at 720 K no deuterium was detected from the TDS setup. At elevated temperatures, deuterium was thermally desorbed from the material. The largest amount of retained deuterium at high flux exposure was found at an exposure temperature of 870 K. The discrepancy between the NRA and TDS values on the total retention, may come from the same reasons explained earlier, mainly related to the deeper

diffusion of deuterium in the sample or due to the localized NRA measurement.

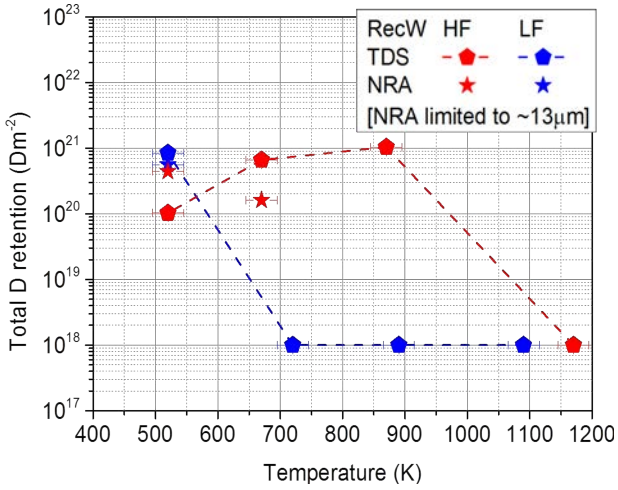

Figure 4.14: NRA and TDS results on total deuterium retention on the recrystallized tungsten samples as a function of surface temperature, exposed to a fluence of $10^{26}\ m^{-2}$ *and various surface temperatures. The blue and red curves represent the exposures to low and high flux density respectively.*

4.1.4 Single Crystal Tungsten (SCW)

In order to eliminate the influence of grain boundaries on the deuterium retention and surface modifications, single crystals were considered in the investigations. Electron microscopy scanning of the single crystal tungsten samples with a (110) lattice plan oriented parallel to the exposed surface, revealed blister formation independently on the exposure temperature and particle flux density. With increasing particle flux, the areal density, shape and lateral size of the blisters increased. At low particle flux and temperature $(520K)_{LF}$, dome-shaped and flat-top blisters of 0.1-1 μm in diameter, were formed. At temperature 680 K, only sparse dome-shaped blisters were found (diameter $<1\mu$m) while only flat-top blisters (lateral size 0.5-1μm) were found at 910 K.

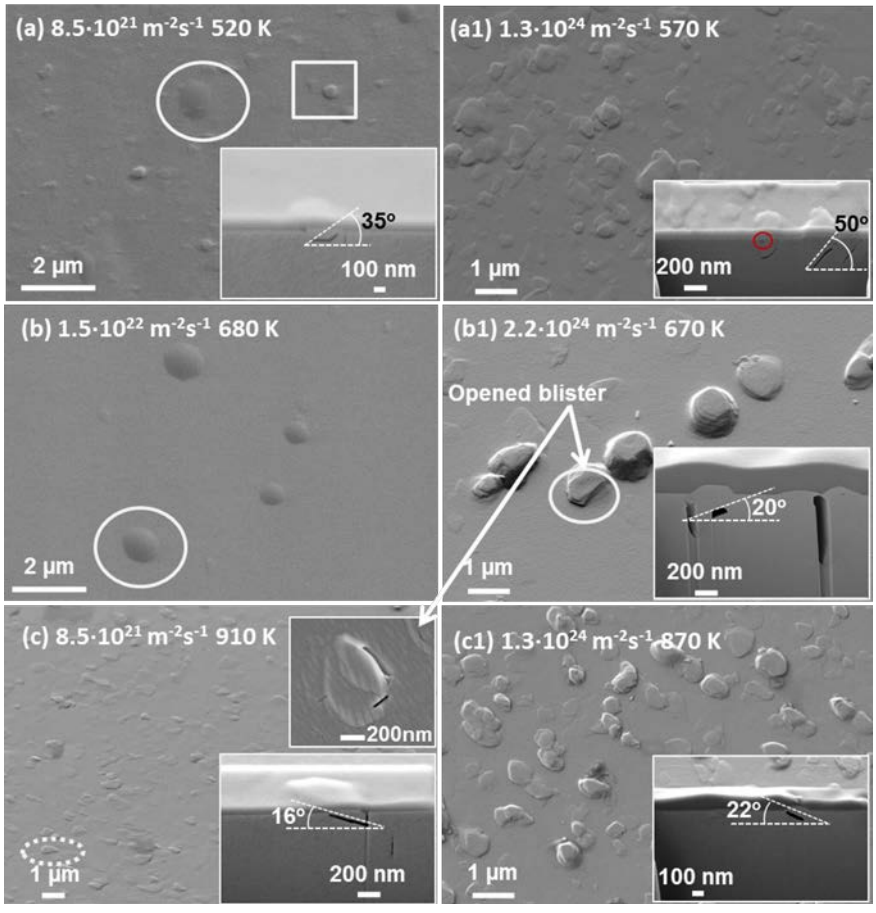

Figure 4.15: SEM images taken on the SCW samples after exposure to D plasma at PSI-2 (a)-(c) and Pilot-PSI (a1)-(c1) at a fluence of $10^{26}\ m^{-2}$ *and incident ion energy of 40 eV.*

Blisters formed at 910 K had openings to the surface as shown in figure 4.15 (c). On the other hand, exposure of single crystal at higher particle flux $(570K)_{HF}$, caused the formation of blisters with a rather flat top and size 0.5-2 μm. At higher temperature $(670K)_{HF}$, blisters appeared at a lower density, still flat-top shaped with a size of 0.1-1 μm and mainly opened. The blister density increased at $(870K)_{HF}$ while the lateral blister size and shape remained similar to lower temperature, although with a higher density.

SEM images taken on the cross sectional cuts, done with a focused ion beam, showed the presence of openings and cavities under the surface. Cavities were detected in the first few nm below the surface (figure 4.15 (a1)). Voids of a lenticular shape were found at a typical depth of ~200 nm, 50-100 nm thick, oriented either perpendicular to the sample surface (generally up to 1 μm deep), or at a certain angle varying from 16 to 50^0.

Earlier studies proposed that the direction of these cavities is related to the gliding in the low-index slip system $\{110\}$ <111> (gliding within the (110) planes in the [111] direction) [20]. However, three slip systems are known to be active in bcc lattices: $\{110\}$<111>, $\{112\}$<111> and $\{123\}$<111>. Physically this occurs when dislocation slip occurs along the <111> direction in the (110), (112) or (123) planes. The <111> direction has the closest packing and is therefore common to all active slip systems [18, 21]. To illustrate, in figure 4.16 are schematically drown bcc lattices and planes (111), (221), (110) and [111] direction.

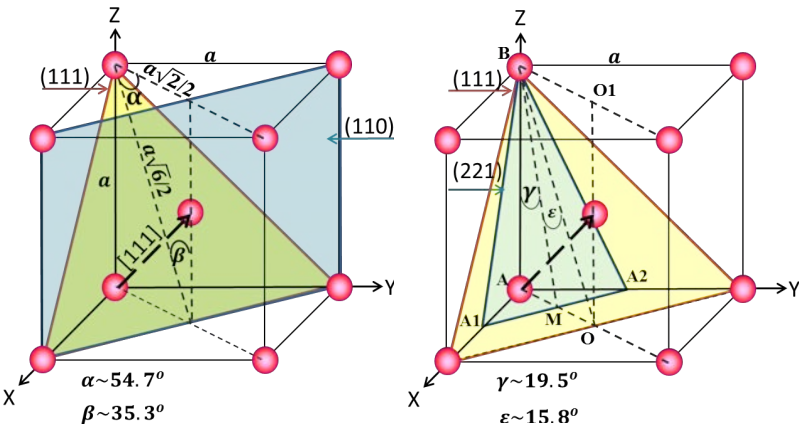

Figure 4.16: Illustration of (110) and (221) crystallographic planes in a bcc lattice and the corresponding angles forming with (111) plan and [111] direction.

Crystal orientations as regard to the applied stress, and temperature have a direct impact on the slip system mechanisms in bcc lattices. High deuterium concentration and plasma irradiation exert stresses and cause dislocations to move through the lattice planes in the direction which is most favorable energetically. In

case of [111] gliding direction, the plane (110) would form the angles $\alpha \sim 54.7^0$ and $\beta \sim 35.3^0$ with plane (111) (see table 4.4).

It was specified before that plane (110) was parallel to the exposed surface. If the gliding plane would be (221), the possible angles, as also shown in figure 4.16, would be $\epsilon \sim 15.8^0$ and $\gamma \sim 19.5^0$. Following these considerations, the cavities which occurred at low temperature $(520K)_{LF}$ and $(570K)_{HF}$, form angles of 35^0 and 50^0 with the surface, respectively. This may be related to the gliding of the (110) plane in the [111] direction, as foreseen. On the other hand, at high flux and temperatures $(670K, 870K)_{HF}$, the formed angles are 20^0 and 22^0. These are actually two of the known slip systems in tungsten, namely (112) [111] and (123) [111]. While at higher temperatures, $(910K)_{LF}$, cavities form typical angels of $\sim 16^0$ which corresponds to the gliding in [111] direction of the (221) plane.

To generalize, these results suggested that at temperatures lower than 670 K, dislocations move along the $\{110\}$ <111> gliding system, while at higher exposure temperatures, $\{112\}$ <111>, $\{123\}$ <111> and $\{221\}$ <111> systems were more favorable.

(110)(111)	35.3^o	(110)[111]	54.7^o	$(520K)_{LF}$	$(570K)_{HF}$
(112)(111)	19.5^o	(112)[111]	70.5^o		$(670K)_{HF}$
(123)(111)	22.2^o	(123)[111]	67.8^o		$(870K)_{HF}$
(221)(111)	15.8^o	(221)[111]	74.2^o	$(910K)_{LF}$	

Table 4.4: Angles between planes of various gliding systems in a bcc lattice

Deuterium depth profiling in single crystal tungsten samples was done from NRA measurements, as plotted in figure 4.17. The deuterium content can be divided intuitively in three regions, similarly as Alimov *et al.* [19] observed after exposure of single crystal and polycrystalline samples to high energy incident deuterium ions (200 eV): (i) up to 0.5 μm, (ii) 0.5-2 μm, (iii) and the bulk >2 μm. The first 0.5 μm of the samples retained a rather high amount of deuterium reaching around 10^{-2} at.fr. This was possibly related to the presence of small blisters and cavities below the surface. While deeper cavities, typically oriented perpendicularly with the surface could be responsible for the second region of deuterium content which extends at about 1.5-2μm. The retention from 2-4 μm is relatively lower compared to other microstructures investigated, amounting to $3 \cdot 10^{-6}$ - $3 \cdot 10^{-5}$ at.fr.

In figure 4.18, the TDS profiles of SCW samples exposed to high and low plasma flux density are given. It has to be noted that the measurement of $(520K)_{LF}$ failed due to technical complications of the TDS setup. The deuterium release after exposure at high flux density plasma started a 650-700 K and had typically one clear peak and a shoulder at lower temperature. Specifically, the sample $(570K)_{HF}$ showed release peaks at 775 and 822 K, sample $(670K)_{HF}$ had peaks

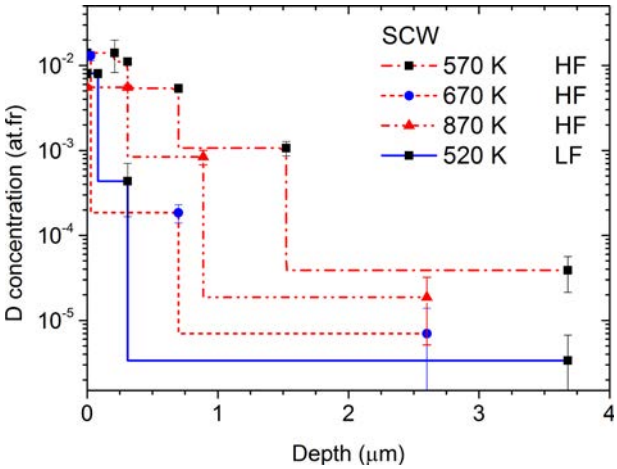

Figure 4.17: Deuterium depth distribution profiles in single crystal tungsten samples as measured with the NRA technique

at 710 and 815 K, and the highest temperature sample $(870K)_{HF}$ had a peak at 810 K and a shoulder at about 720 K. The appearance of peaks and shoulders indicates that more than one trapping sites with different activation energies could be present in the material. In table 4.5 are summarized the exposure conditions and TDS desorption peak temperatures of SCW samples.

Sample name	Surface T (K)	Ion flux $(m^{-2}s^{-1})$	Exposure time (s)	T_{peak} (K)
SCW (PSI-2)				
SCWJ1	520	8.5E21	11765	-
SCWJ2	680	1.5E22	6667	-
SCWJ3	910	8.5E21	11765	-
SCW (Pilot-PSI)				
SCW1	570	1.3E24	77	775, 822
SCW2	670	2.2E24	45	710, 815
SCW3	870	1.3E24	77	810

Table 4.5: Exposure conditions of SCW samples and results on the areal density of blisters and TDS peak temperature

The integrated amount of retained deuterium, according to the TDS measurements (figure 4.19), had a maximum at $(670K)_{HF}$ and it dropped at about one order of magnitude at $(870K)_{HF}$. According to Haasz *et al.* [17], diffusion in single crystal tungsten is trap-limited and saturation at 500 K occurs at three times lower fluence compared to 300 K, possibly due to the de-trapping of deuterium

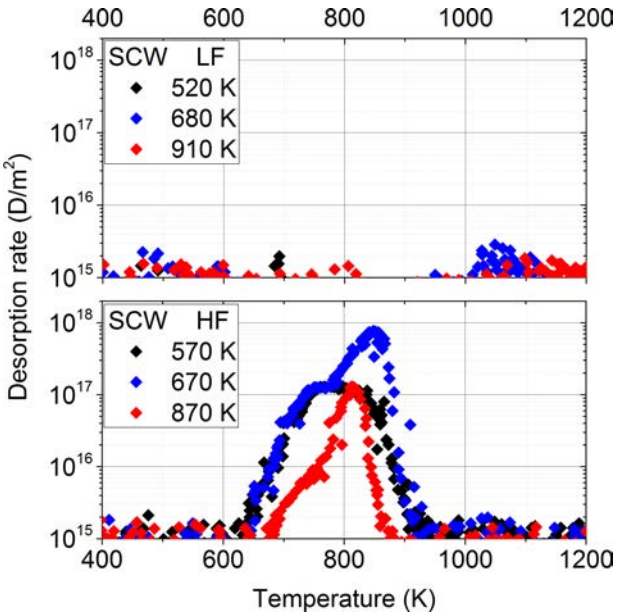

Figure 4.18: TDS spectra of desorbed deuterium from the single crystal tungsten samples exposed to low ($\sim 10^{22}\ m^{-2}s^{-1}$) and high ($\sim 10^{24}\ m^{-2}s^{-1}$) particle flux density.

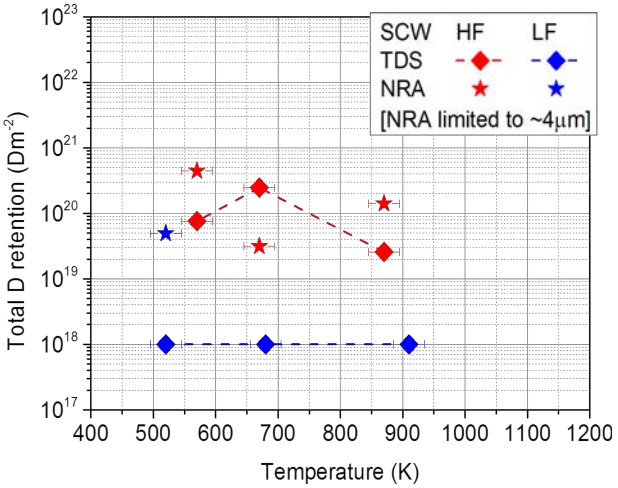

Figure 4.19: TDS results on total deuterium retention on the single crystal tungsten samples as a function of surface temperature, exposed to a fluence of $10^{26}\ m^{-2}$ and various surface temperatures. The blue and red curves represent the exposures to low and high flux density respectively.

from defects (0.7-1 eV) at higher temperatures. Considering also that in a single crystal the grain boundaries are missing, deuterium diffusion is consequently slower and limited to the trapping in the first few micrometers. Also in this case there is a discrepancy between NRA and TDS measurements about the calculation of the total amount of deuterium retention. In case of sample $(520K)_{LF}$, NRA integration was clearly larger because the TDS measurements were not available. While in other cases, concerning the samples which were exposed to high particle flux, the discrepancy might appear due to either thermo desorption at room temperature or non homogeneous plasma loading of the sample surface.

4.1.5 Summary and modeling results

The present work results on surface modifications and deuterium retention in tungsten, after exposure to pure deuterium plasma, revealed a pronounced dependence on material microstructure, incident particle flux and surface temperature. Exposure to higher particle flux decreased the maximum of deuterium retention and caused blister formation even at high temperatures.

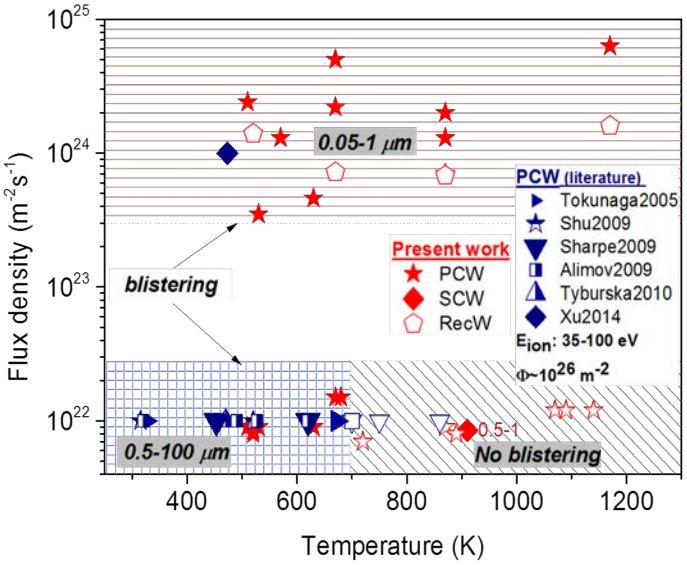

Figure 4.20: Lateral blister size is given as a function of exposure temperature and incident flux density. Empty symbols indicate the lack of blistering. The red stars (★), pentagons (⬠) and filled diamonds (◆) represent the present work results on blistering of the "as received" (LGW and SGW), RECW and SCW samples, respectively. The literature data (blue symbols) correspond to polycrystalline tungsten material [4, 10, 11, 22–24]

In figure 4.20, blister formation domain is given as a function of exposure temperature and particle flux conditions, including the relevant literature results on polycrystalline tungsten. Exposures at low particle flux density ($\sim 10^{22}\ m^{-2}s^{-1}$), confirmed the known results: blisters were suppressed at temperatures above 700 K in polycrystalline samples. Blister shape, lateral size and density appeared in a large variety, depending mainly on the exposure temperature, material microstructure, sample preparation and production history. However, this was not the case for single crystal samples because blistering persisted even at exposure temperature of 910 K. At high particle flux density ($\sim 10^{24}\ m^{-2}s^{-1}$), blistering appeared independently on the exposure temperature, except on the recrystallized samples where no blisters were observed. At higher exposure flux, the maximum of the lateral blister size decreased by two orders of magnitude, compared to the low flux

exposure.

The factors that may influence the appearance of nanostructures in case of high flux compared to the low flux exposure are related to the defect formation during irradiation itself and heat dissipation into the bulk [25]. Exposure to high particle flux leads to the formation of additional defects in the crystal, due to the deuterium diffusion and imbalance between solubility, diffusion to the bulk and surface recombination [4]. In order to ensure similar surface temperatures at fluxes which varied by two orders of magnitude, the sample cooling had to be more efficient when the particle flux was higher. Therefore, heat dissipation was related to the temperature gradient through the bulk. The temperature gradient during short exposures (i.e at Magnum-PSI), was much steeper compared to longer exposures (at PSI-2) leading to a shorter diffusion depth. A shorter exposure time may also lead to a short time given to the traps (vacancies) to agglomerate and create clusters for blister nucleation. The latter could be supported by the formation of the high density of small blisters which in addition are distributed more homogeneously.

Incident particle flux density impact was studied also in terms of deuterium depth distribution and total retention in the samples. Depth profiling of retained deuteritum in exposed tungsten samples was performed with the nuclear reaction analysis (NRA) technique using ^3He ions with energies in the range of 0.5 to 6 MeV. The results indicated that deuterium was retained in almost all samples up to the NRA probing depth of about 10 μm with maximal deuterium concentration of about 2 at.$\%$ in the very near surface region of several tens to hundreds nm, decreasing typically to about 0.1 at.$\%$ at about 1 μm depth. The deuterium concentration at a depth of above 5 μm varied from 0.001$\%$ to 0.1$\%$ for different samples. After exposure to low flux plasma, deuterium depth profile was generally smoother towards larger depths, compared to high flux exposure cases, where the profile was rather steep in the first few micrometers. However, this held true in case of polycrystalline samples whereas in case of single crystal, the depth profiles were similar at either incident flux. With increasing temperature, deuterium was found to diffuse to larger depths.

The total deuterium retention was measured by means of thermal desorption spectroscopy (TDS). In the cases with low exposure temperatures, the total deuterium retention was one to two orders of magnitude higher after exposure to the low flux compared to the high flux density. On the contrary, an opposite increase of the total deuterium retention at high exposure temperatures was observed for the high particle flux case compared to lower flux exposures. In such a way, the maximum of the total deuterium retention was observed to occur at a higher temperature in the case of high incident particle flux ($\sim$850 K) compared to low flux exposures ($\sim$650 K). Overall, experimental results on deuterium retention were similar for all the investigated tungsten microstructures. Deuterium retention decreased at high temperatures and the maximal retention was lower for high flux

exposures. However, due to the shift of the maximal retention to higher temperatures, the amount of deuterium retained at temperatures above 800 K was higher at high flux rather than at low flux, being still about one order of magnitude lower than the maximal retention at low flux.

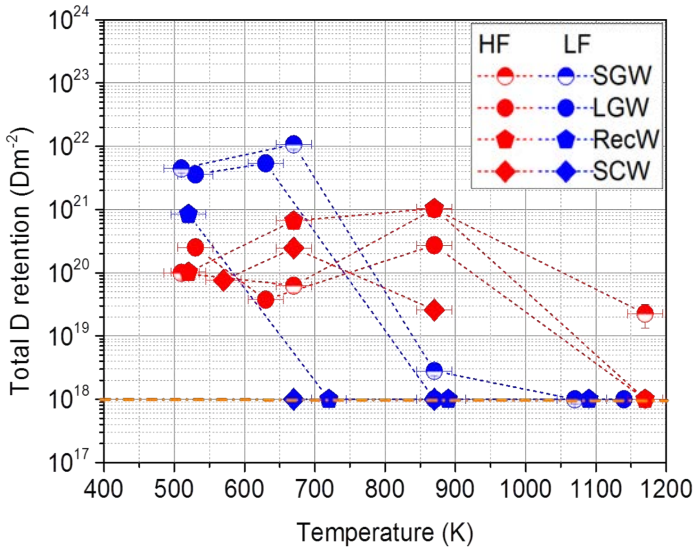

Figure 4.21: TDS results on total deuterium retention on the four different microstructure tungsten samples as a function of surface temperature, exposed to a fluence of $10^{26} m^{-2}$ *and various surface temperatures. The blue and red curves represent the exposures to low and high flux density respectively.*

The maximum on total retention is a result of the correlation between the incident particle flux and surface temperature. Deuterium diffusion and its trapping in the material are thermally activated processes which means they strongly depend on the temperature. The total amount of deuterium that remains in the sample depends on the diffusion depth and trapping energies, relying finally on the equilibrium between the trapping and thermal diffusion at room temperature. Deuterium diffusion depth depends on the exposure time and temperature: higher exposure time leads to deeper the diffusion. Therefore, the long exposure time at low flux plays a similar role as the high temperature does during higher flux exposure, both leading to longer diffusion depths and subsequently, larger amount of retained deuterium.

The trends of deuterium retention in tungsten can be attributed to the interplay of processes of damage creation, deuterium recycling and return back into plasma, and deuterium diffusion deeper into the bulk. For the same total fluence, low flux exposures correspond to longer exposure times than high flux exposures. At low

flux and high temperature, long exposure times allow for deuterium diffusion into the bulk, as well as for desorption at the plasma facing surface. At high flux, larger concentration gradients of deuterium can be expected to be build, leading potentially to stronger material damage and/or faster growth of deuterium filled bubbles or voids. At the same time, diffusion of deuterium deep into the material allows for deuterium trapping at intrinsic lattice defects, such as vacancies, dislocations and grain boundaries in case of polycrystalline samples. For typical grain sizes of about several μm to several tens of μm, short exposure times do not allow for efficient deuterium diffusion to grain boundaries, so it is then presumably trapped at intra-granular defects. According to DFT calculations, dislocation loops and grain boundaries can act as fast diffusion paths for deuterium, both towards the bulk and towards the surface. At the same time, kinks and jogs on dislocation lines and irregularity of grain boundaries can serve as nucleation sites for deuterium accumulation and growth of bubbles, e.g. by means of dislocation loop punching mechanism.

It is however inquisitive to understand how significant can these numbers be in terms of ITER divertor inventory. Assuming the retention to be, in the least optimistic case, the maximum for each particle flux in the given temperature range. For example, if in case of low flux, the retention would be 10^{22} Dm^{-2}, temperature range 500-700 K, total incident fluence 10^{26} m^{-2} and exposure time of 10^4 s, the total amount of retained deuterium in the divertor area (210 m^2) would be 6.97 mg (0.2788 mg per ITER discharge). Considering high flux, assuming the retention in the range $5 \cdot 10^{20}$ Dm^{-2}, temperature range 500-900 K, total incident fluence 10^{26} m^{-2} and exposure time of 10^2 s, the total amount of retained deuterium in the divertor area (210 m^2) would be 0.35 mg (1.4 mg per ITER discharge). Depending on how much the retention would be at high flux ($5 \cdot 10^{20}$-10^{21}), the total inventory at high flux would be 5 to 10 times larger than at low flux, per unit time. *J. Roth and K. Schmid* [26] cite in their paper that in a steady state fusion device, the total amount of retained tritium might vary in the range between 20 g (at 373 K) and 20 mg (773 K). However, the total retention will be attributed to the trapped deuterium in the metal, as the solute inventory in ITER divertor will the desorbed during discharges.

In order to get insight into trapping energies of deuterium retained in tungsten after experiments described in this work, modeling of the measured thermal desorption spectra was performed using the rate equations approach implemented in the Coupled Reaction Diffusion Systems (CRDS) code. The initial distribution of trapped deuterium was deduced from NRA depth profiles. In few cases, the implantation phase, i.e. the plasma exposure, was also simulated assuming the empty trap distribution corresponding to the same NRA profiles. In these cases, no difference with the cases without simulation of implantation was observed, since plasma exposure just leads to filling of empty traps (no damage creation imple-

mented). Considering the discrepancy between NRA and TDS measurements on the total amount of deuterium inventory, the NRA profiles had to be scaled in order to fit the maximum of the TDS profiles. The main parameters which were used in the CRDS modeling, are summarized in table 4.6.

In all the simulated cases several assumptions had to be imposed in order to reproduce the measured TDS peaks. First of all, in order to reproduce narrow widths of the peaks, deuterium re-trapping at defects had to be switched off. Secondly, the de-trapping frequency, i.e. the pre-exponential factor of the Arrhenius type equation for de-trapping had to be adjusted to values about 120-500 times less than typical Debye frequencies. Constant temperature ramp of 0.2 was used for the recrystallized and single crystals and the real temperature ramp was implemented in the code for the simulation of the SGW samples, since its linearity was not homogeneous (see figure 4.23). With such a setup, the TDS peaks could be reasonably well reproduced assuming either one trapping energy of 2.2 eV (recrystallized tungsten) or two trapping energies of 1.9 eV and 2.0 eV for single crystal tungsten and 2.0 eV and 2.3 eV for other polycrystalline samples. CRDS simulations indicate that to better reproduce the high temperature tail of TDS peaks for high temperature exposure samples, as well as for low flux cases, deeper retention profiles of deuterium than measured by NRA have to be assumed. In particular, a low density of intrinsic traps of about $5 \cdot 10^{-4}$ at.$\%$ up to mm scale was used in the recrystallized tungsten cases. This is in line with the assumption of deeper deuterium diffusion at high temperatures and longer exposure times. Simulations indicate that deuterium can diffuse even up to the opposite side of 4-mm thick samples during long exposure time.

In figures 4.22 and 4.23, the experimental data and simulated curves with the CRDS code are plotted. The trapping energies in single crystal samples could be attributed to trapping in defects such as dislocations, vacancy clusters or small cavities which were observed in the near surface region. For the simulations it was necessary to assume traps profile up to 10 μm deep in case of single crystal tungsten while in for the recrystallized tungsten, trapped deuterium reached mm scale. In both, recrystallized and SGW samples, it was proved that higher exposure temperature and longer exposure times lead to deeper deuterium diffusion in the material. Diffusion depth scaled as square root of exposure time in RECW1 and RECWJ1 samples.

No evidences of lower trapping energies could be seen from the measured TDS spectra, thus suggesting that either the low energy trap sites get depopulated during exposure due to high exposure temperature or that deuterium trapped at such trap sites gets first re-trapped in high energy traps before being released at higher temperatures. From the physical point of few, such a combination of facts can be explained in the frame of void formation at nucleation sites on dislocation loops and grain boundaries. Deuterium is then trapped on the inner surfaces of such

Sample	Exp. T (K)	TDS T_{peak} (K)	$E_{trap}1$ (eV)	$\nu_{de-trap}$ s^{-1}	Trap distribution a*NRA profile	$E_{trap}2$ (eV)	$\nu_{de-trap}$ s^{-1}	Trap distribution NRA scaling factor
SCW1	570	775, 822	1.9	ν/120	0.07*(up to 10 μm)	2.0	ν/250	0.09 up to 10 μm
SCW2	670	710, 815	1.9	ν/120	0.40*(up to 10 μm)	2.0	ν/500	5.0 up to 10 μm
SCW3	870	780, 810	1.9	ν/200	0.01*(up to 10 μm)	2.0	ν/200	0.33 up to 10 μm
RECW1	520	886				2.2	ν/200	0.35 +5e-6*(8.5μm<x<40μm)
RECW2	670	865				2.2	ν/200	1.5 +5e-6*(8.5μm<x<1mm)
RECW3	870	905				2.2	ν/200	2.0 +5e-6*(8.5μm<x<1mm)
RECWJ1	520	887				2.2	ν/200	1.0 +5e-6*(8.5μm<x<0.5mm)
SGW1(W10)	510	852, 930	2.0	ν/200	0.35*(up to 8 μm)	2.2	ν/200	0.2 up to 8 μm
SGW3(W12)	870	965				2.3	ν/200	1.75 +5e-6*(8.5μm<x<2mm)
SGWJ1(W8)	510	963				2.3	ν/200	4.5 +5e-6*(8.5μm<x<0.5mm)

Table 4.6: Main parameters included in the CRDS modeling

voids, which can be formed by loop punching or vacancy clustering. The energy barrier for deuterium to move from the inner surface of the void into the material bulk should be then comparable with that for deuterium atoms on a free tungsten surface, which is estimated to be of about 2 eV in the literature. The frequency factor for de-trapping cannot be then directly related to the Debye frequency of the lattice and can be expected to depend on the size of the void and the amount of deuterium there. If dislocations provide also low energy trap sites, then deuterium released from them at lower temperatures would diffuse fast along dislocation lines and will be re-trapped at voids. Deuterium released from the void directly into the bulk can then diffuse to the surface almost without re-trapping, due to relatively sparse distribution of voids.

Another simulation done with the CRDS code was dedicated to the pulsed exposure at Pilot-PSI and its influence on deuterium retention. Temperature ramp was simulated as plotted in figure 4.24 and implantation and desorption were simulated and compared with the constant temperature heating ramp (steady state exposure). From the simulation it was concluded that the pulsed exposure, number of pulses, exposure temperature or waiting time between pulses did not have any influence on deuterium inventory. At low trapping energies, deuterium could be released after every plasma pulse but in case of high binding energy, deuterium is trapped and "frozen" in traps, even after plasma is switched off.

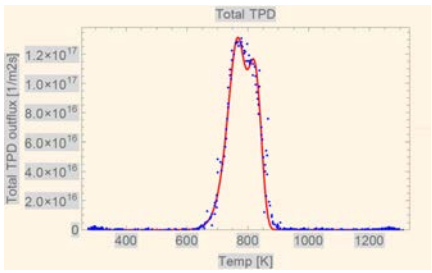

(a) SCW1 (570 K - HF)

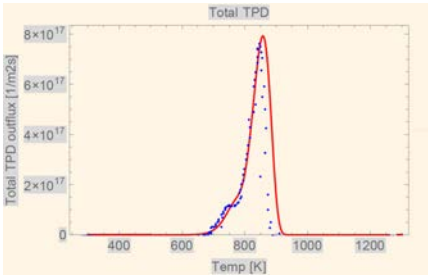

(b) SCW2 (670 K - HF)

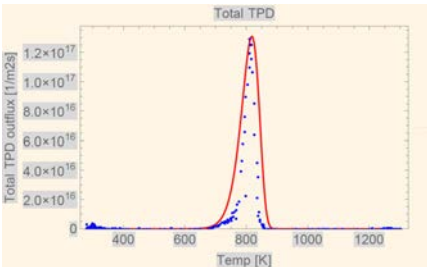

(c) SCW3 (870 K - HF)

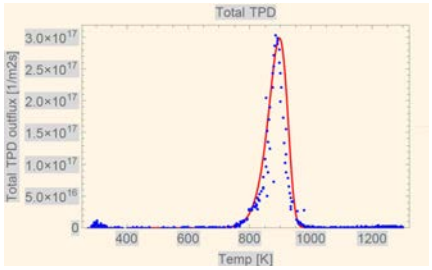

(d) RECW1 (520 K - HF)

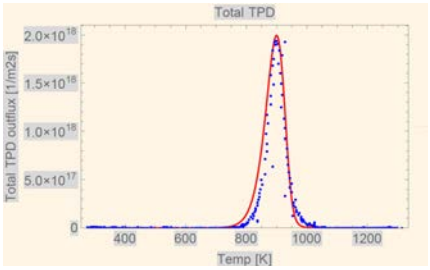

(e) RECW2 (670 K - HF)

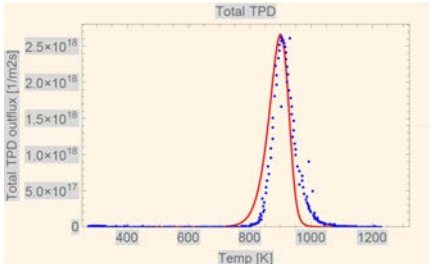

(f) RECW3 (870 K - HF)

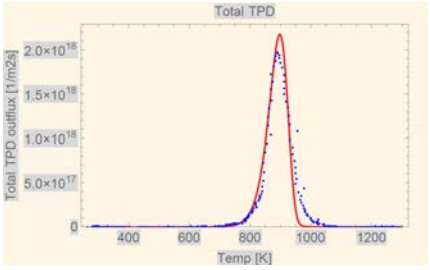

(g) RECWJ1 (520 K - LF)

Figure 4.22: CRDS simulation of ScW and RecW samples

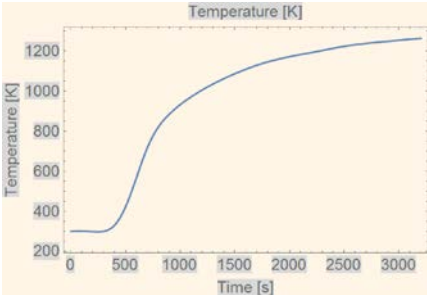

(a) Real TDS T_{ramp} of SGW samples

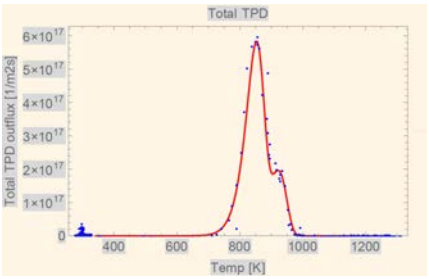

(b) SGW1 (510 K - HF)

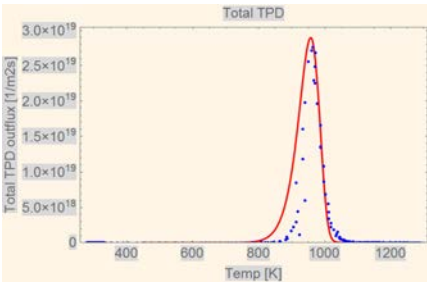

(c) SGWJ1 (510 K -LF)

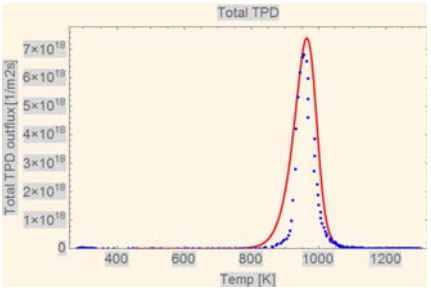

(d) SGW3 (870 K - HF)

Figure 4.23: CRDS simulation of SGW samples

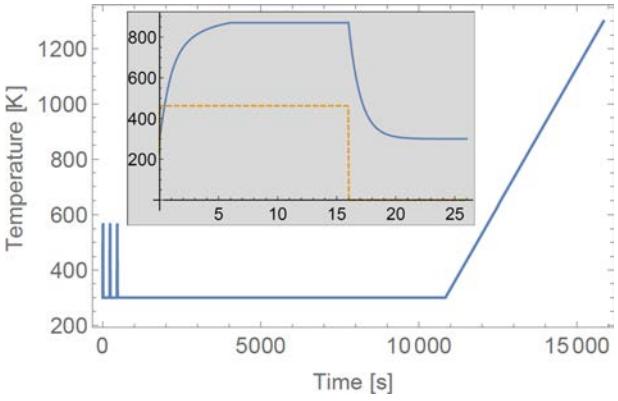

Figure 4.24: Temperature evolution during exposure at Pilot-PSI used to simulate implantation and desorption

4.2 Mixed D/He plasma exposure of recrystallized tungsten

Numerous investigations have been performed assessing the influence of helium irradiation on tungsten, as one of the plasma species in a fusion reactor. He bombardment produces surface morphology changes on tungsten such as cracking, bubble formation and nanostructure growth on the surface, referred to as fuzz [27–32]. In the present work, a set of experiments was dedicated to the influence of He impurities in D plasma, typically 5% of He ions, and its impact on the flux dependence of deuterium retention and surface morphology. Recrystallized tungsten samples were exposed to a temperature range 520-1090 K at a particle flux $\sim 10^{22}\ m^{-2}s^{-1}$ at PISCES-A linear plasma device. The total ion fluence was $10^{26}\ m^{-2}$. The exposure conditions are summarized in table 4.7.

Sample name	Gas mixture	Temperature (K)	Ion flux $(m^{-2}s^{-1})$
RecPA1	5%He/D_2	520	8.01E21
RecPA2	5%He/D_2	720	1.24E22
RecPA3	5%He/D_2	890	1.75E22
RecPA4	5%He/D_2	1090	2.06E22
RecPA5	D_2	520	8.62E21

Table 4.7: RECW samples exposed at PISCES-A at fluence $10^{26}\ m^{-2}$.

In figure 4.25 the SEM images on the samples are given. After exposure to He/D plasma environment, samples showed resilience to blistering. At 520 K the surface was roughened due to the small pyramidal structures. These nanostructures, which are considered as a precursor of fuzz formation, were reported earlier after pure He exposures at lower particle flux [33]. With increasing temperature to 720 K, small pinholes of a few nanometers and ridges which become less extrusive at 890 K, were found. Development of pinholes is thought to come due to the activation of thermal vacancies which are mobile at high temperatures therefore, the internal gas pressure is in equilibrium with bubble growth until they reach the metal surface. Another mechanism could be related to the mobility of the bubbles due to the lateral stress which drives them close to the surface [25]. Exposure of recrystallized samples at 1090 K caused the formation of nanorods which reached a length of above 200 nm from the surface (figure 4.26).

As mentioned before, the fuzzy structures generally occur at temperatures 1000-2000 K, ion energy $E_{ion} \geq 20eV$ and fluence $\sim 10^{25}\ m^{-2}$ [29] (figure 2.13). The growth rate of the modified layer increases with temperature and the square root of exposure time, indicating a diffusive step dependence [30, 34] and its thickness is determined by plasma erosion rate [35]. However, the presence of small amount of carbon or beryllium impurities in the plasma hinder the fuzz

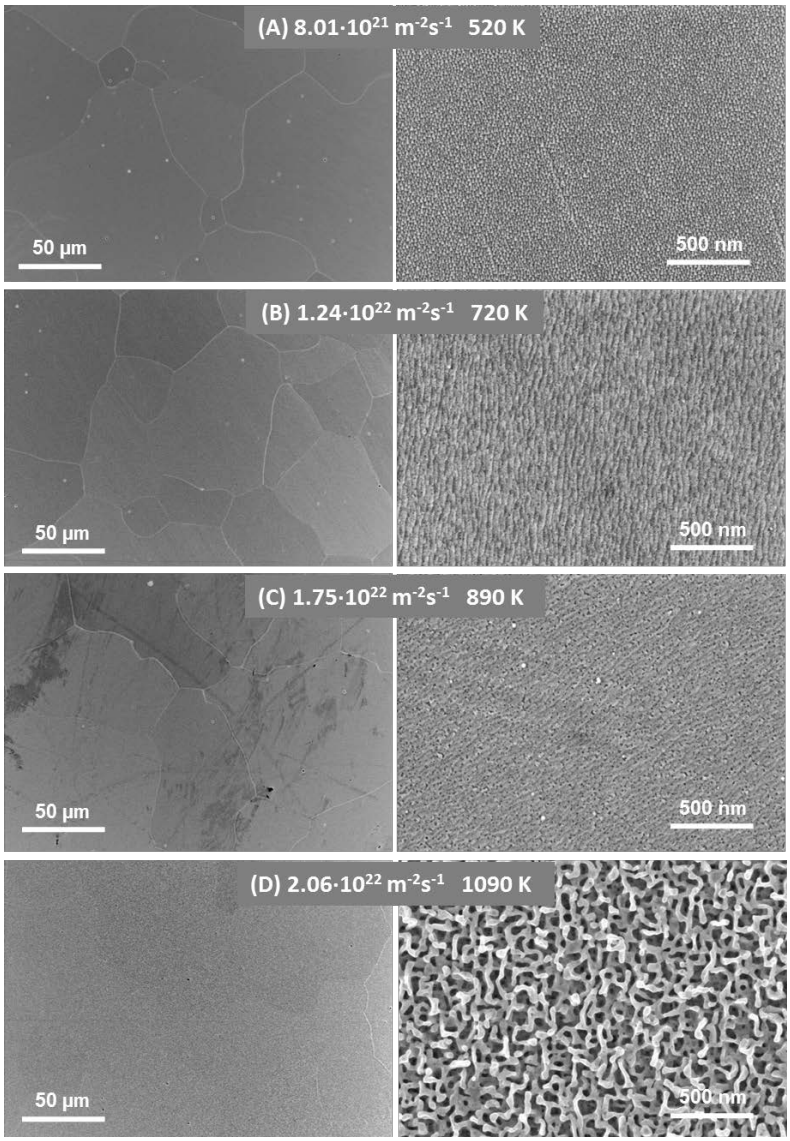

Figure 4.25: SEM images taken on the RecW samples after exposure to 5% He/D plasma at PISCES-A at a fluence of $10^{26}\ m^{-2}$ and incident ion energy of 40 eV. The surface temperature was varied from 520 to 1090 K.

formation rate, favoring the formation of tungsten alloys layers [28]. The proposed mechanisms for fuzz formation are typically based on the bubble formation and nanorod growth which could arise for example from the coalescence of small overpressurized He bubbles to the surface [29], tungsten flow over the He bubble

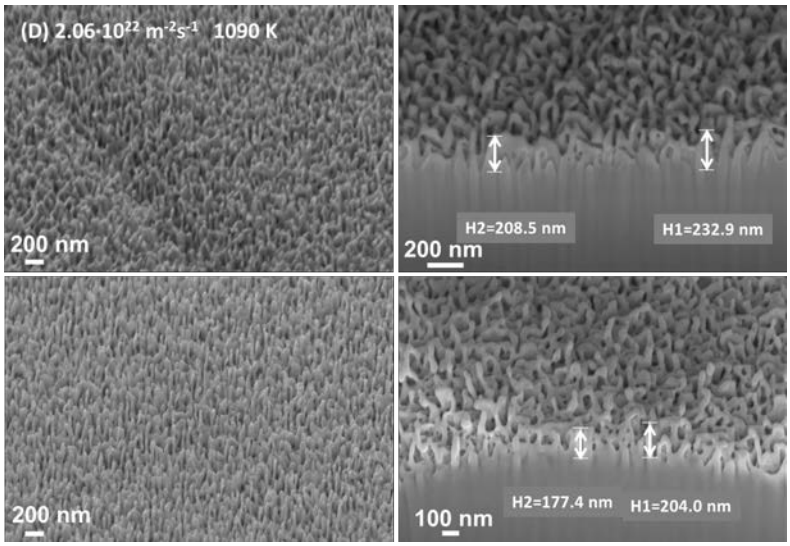

Figure 4.26: SEM images taken on the sample after exposure to 5% He/D plasma at PISCES-A at a fluence of 10^{26} m^{-2} and surface temperature of 1090 K. From the cross sectional FIB cuts, the nanorods are visible at a length of above 200 nm from the surface

skin (viscoelastic model [36]) or via loop punching and bubble rupture [37].

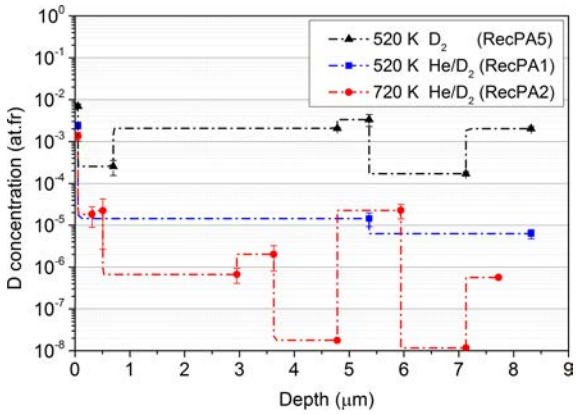

Figure 4.27: Deuterium depth profiles of recrystallized samples exposed to pure deuterium plasma and mixed plasma with 5% He content

NRA measurements indicated that deuterium concentration dropped up to two orders of magnitude (figure 4.27 and 4.28), when 5% of He was added to pure D plasma. When temperature increased to 720 K, deuterium content dropped even further. A common feature of deuterium depth profiles is the fact that retention

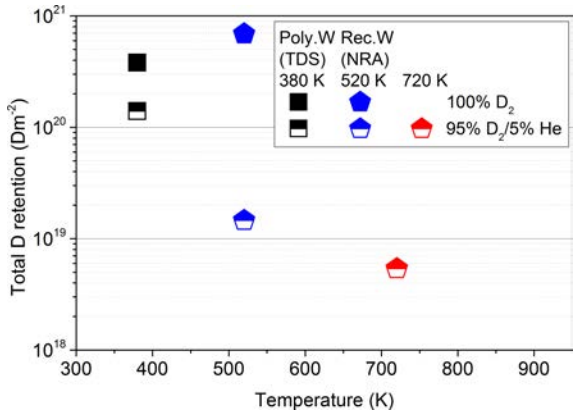

Figure 4.28: Total deuterium retention as calculated from the NRA measurements for the present exposures of the recrystallized samples and previous results from polycrystalline samples [38]

dropped considerably in the first 50 nm. Total retention of deuterium calculated from the NRA measurements was found to be similar to values reported from Alimov *et al.* [11]. Retention after exposure of the recrystallized sample at PISCES to pure deuterium plasma was $6.91 \cdot 10^{20}\ m^{-2}$, while it was found $8.45 \cdot 10^{20}\ m^{-2}$ from the TDS measurements after exposure to PSI-2 (520 K). In samples RecPA1 and RecPA2, a total amount of $1.46 \cdot 10^{19}\ m^{-2}$ and $5.38 \cdot 10^{18}\ m^{-2}$ was retained, respectively. At the same flux and total fluence used in the present experiments at 380 K, Reinhart [38] found from the TDS data, an amount of $3.8 \cdot 10^{20}\ m^{-2}$ and $1.4 \cdot 10^{20}\ m^{-2}$ after exposure to pure D plasma and $95\%D2 + 5\%He$ (figure 4.28).

Previous studies have shown that deuterium retention and blistering is suppressed when tungsten samples are pre-exposed to He plasma at 700 K and polished to a mirror finish [39]. This observation was confirmed later on, where besides the blister suppression, it was reported a decrease in the total amount of deuterium inventory occurring at temperatures higher than 400 K. [11, 38, 40, 41]. The argument of deuterium intake suppression after exposure to helium seeded plasmas is based on the He bubble formation in the implantation zone where D is trapped at the periphery of He bubbles [42]. Therefore, He bubble layer serves as a barrier for deuterium to diffuse deeper and in addition it dissipates the stresses formed by the local supersaturation of deuterium [43].

4.3 He and H transient heat and particle loads on polycrystalline tungsten

The aim of the present study is to address the effect of He nano-bubble layer formation in the near surface region of tungsten under ITER relevant steady state and transient heat and particle loads. Edge localized modes were simulated in terms of frequency, pulse duration and energy, and power densities [44]. The changes of the thermal conductivity were investigated and compared with the relevant exposures in hydrogen.

Simulations predict a temperature range 600-1200 K for major part of the outer divertor (figure 2.9), coinciding with the temperature of bubble layer formation [45]. ELM repetition rate (f_{ELM}) is of the order of 10 Hz with a 1 ms pulse duration and 0.2-0.5 MJm^{-2} energy density [44]. The present plasma devices currently operating and capable of simulating similar ITER divertor plasma conditions are Magnum-PSI and Pilot-PSI situated at DIFFER [46–48]. This study was entirely carried out at Pilot-PSI linear plasma device where the relevant steady state and transient particle and heat loads were obtained by using a pulsed plasma source and a high power laser (ms-pulse duration) in case when longer exposure time was required. Temperature measurements were done with a FLIR SC7500MB fast infrared camera with a high recording frequency of 3 kHz, which allowed a good temporal resolution of the temperature trace during the plasma exposure.

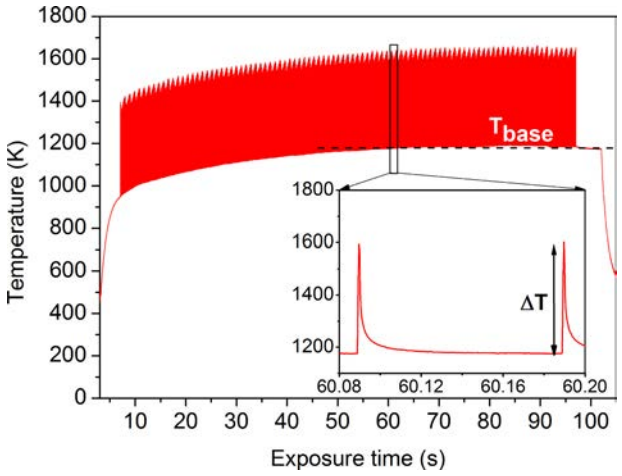

Figure 4.29: Infrared camera temperature profiles during one plasma shot in He, where steady-state and transient loads were combined. The real temperature was converted from digital data and calculated assuming the temperature dependent emissivity coefficients

In figure 4.29, an example of the temperature profile recorded with an infrared camera during one discharge of He plasma is given. The base temperature was

set initially by the plasma heating until the seventh second of the plasma operation, when the laser was triggered, raising the temperature at a value of ΔT above the base temperature. For lower fluences (total exposure time up to 100 s), the combination of steady-state and transient heat and particle loading on the sample was achieved by using a pulsed plasma source (setup description is given in chapter 3). The real temperature was converted from digital level data and calculated assuming the temperature dependent emissivity coefficients of tungsten.

ITER grade tungsten samples were mechanically polished, annealed for 1 hour in 1273 K and ultrasonically cleaned in acetone and alcohol (30 min each) to remove the polishing residuals. Two sets of identical samples were exposed to He and H under similar plasma exposure conditions, ion energy and surface temperature. Heat load density was varied from $\sim$0.2 to $\sim$0.3 MJm^{-2} and power density achieved during steady state and transients was up to 6.1 and 420 MWm^{-2} per plasma discharge, respectively. Surface temperatures achieved ranged between 670-770 K and 970-1170 K. Total exposure time to plasma was $\sim$100 s and 1000 s while the ion fluence scaled from $\sim 3 \cdot 10^{25}$ to $1.5 \cdot 10^{27}$ m^{-2}. Samples were biased to a negative potential, yielding an ion energy of 40 eV. A summary of the exposure conditions of tungsten samples in He and H is given in table 4.8. During the He exposures of samples ELMW2 and ELMW3, 10% (gas flow) of H was added to the plasma in order to improve the plasma source performance and minimize the amount of eroded material from the cathode. In table 4.9, results on the surface impurity content, roughness, and heat flux calculations after exposure, are included. The mass of tungsten samples was measured before and after exposure to the plasma and the observed changes were negligible, indicating no erosion conditions.

Surface morphology changes were investigated with a scanning electron microscope (SEM) on the surface and cross sections after cutting with a focused ion beam (FIB). From the SEM images it was shown that all the sample surfaces were modified after exposure. In addition to cracking, a rather thick porous layer was present after exposure to helium plasma. Subsequently, a careful surface elemental composition analysis was done with the energy-dispersive X-ray spectroscopy technique (EDX). No significant amount of deposited material during exposure was detected on the surface of the samples exposed to H plasma. However, 75% of the samples exposed to He plasma, were heavily contaminated with Mo, which most probably was eroded from the plasma source under such exposure conditions. In table 4.8, the deposited samples are highlighted in gray color and the Mo content together with the layer thickness were analyzed with EDX and FIB/SEM techniques. In the appendix are given the SEM pictures (C.1, C.2, C.3) taken on the cross section cuts of the samples, where a thick porous Mo layer was found on the surface. In figure C.4 is given a qualitative EDX spectrum on the IGW3 sample exposed to He, indicating the presence of Mo, which constituted the major

part (in wt%) of the scanned area.

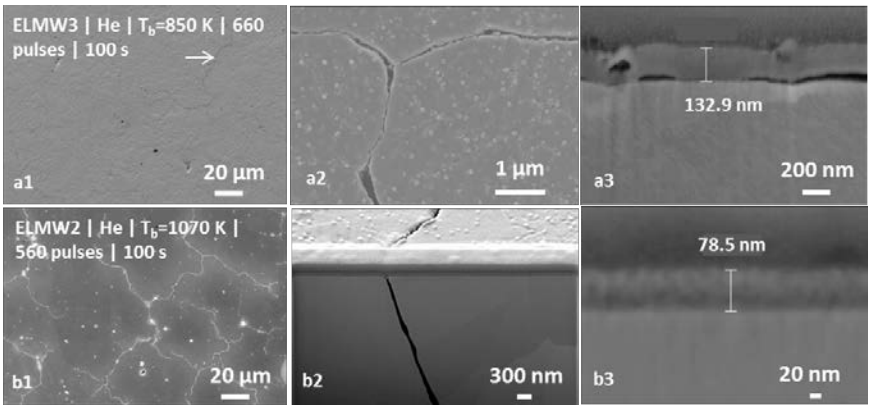

Figure 4.30: Tungsten samples exposed to He plasma for 100 s at 850 K (a1-a3) and 1070 K (b1-b3) at 660 and 560 plasma pulses respectively

Exposure of tungsten samples to He plasma for 100 s at 850 K (4.30 a1-a3) and 1070 K (4.30 b1-b3) at 660 and 560 plasma pulses respectively, resulted in the formation of a fine cracking network in case of higher temperature (1070 K), while at lower temperature (850 K) cracks appeared at a lower density. A thin porous layer of about 78-130 nm was formed on the surface, which, most likely, based also on the EDX analysis, was formed due to the plasma impurity deposition. The fine cracks which were formed at higher temperature, were at about 100 nm wide and spread a several μm in the depth, with no clear indication of an along-the-grain-boundary propagation.

Repeating the same exposures in H resulted in larger cracking at both, low and high temperatures (figure 4.31). Samples were exposed to H plasma for 100 s at 800 K (4.31 e1, e2) and 1120 K (4.31 f1, f2) at 660 and 560 plasma pulses respectively. The relevant exposure in steady state H plasma at 770 K is given in figures 4.31 m1 and m2. After the H exposure at lower temperature (800 K), large cracks, up to 2 μm wide and above 28 μm deep, occurred. At higher exposure temperature (1120 K), similar sparse cracks were formed but they propagated to smaller depths, typically up to 11 μm. Differently from the similar He exposure at high temperature, where the cracking network covered the whole exposed area with fine cracks, in the H case they were more sparse and localized. As expected, the steady state exposure in H didn't cause any surface modifications to the sample surface (4.31 m1, m2 and 4.32 n1, n2). When the number of plasma pulses increased to 960, a large crack was formed at 670 K (4.32 g1, g2), easily visible to the bare eye while at higher temperature 980 K (4.32 h1, h2) the surface of the sample was considerably roughened but no cracks were found probably due to the differences in the energy density and the peak power density.

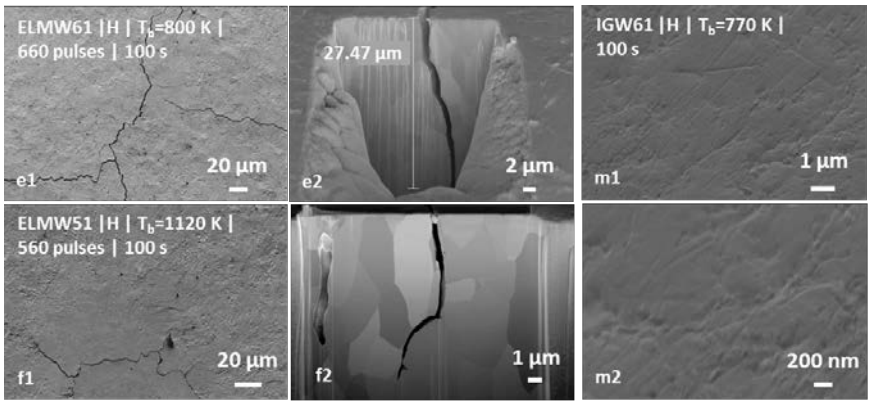

Figure 4.31: Tungsten samples exposed to H plasma for 100 s at 800 K (e1, e2) and 1120 K (f1, f2) at 660 and 560 plasma pulses respectively. The relevant exposure in steady state H plasma at 770 K is given in figures m1 and m2

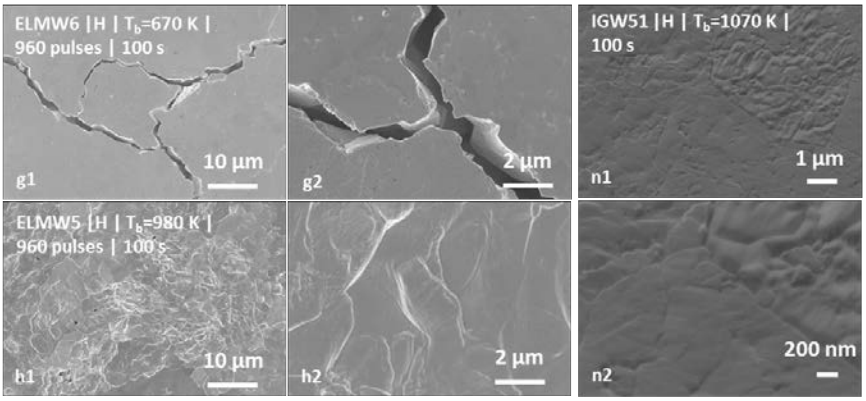

Figure 4.32: Tungsten samples exposed to H plasma for 100 s and 960 plasma pulses at 670 K (g1, g2) and 980 K (h1, h2). The relevant exposure in steady state H plasma at 1070 K is given in figures n1 and n2

Roughness measurements were done using a DEKTAK stylus profilometer and the results are given in table 4.9. In all cases of H and He exposure, the roughness of the samples increased when the base temperature increased from 770 to 1070 K. The difference in roughness when the temperature increased was more pronounced after 105 s of H exposure and 960 plasma pulses (samples ELMW5 (207 nm) and ELMW6 (38 nm)). Sample ELMW6 after exposure to 670 K base temperature had large cracks, up to 2 μm wide, while the sample ELMW5 after exposure to 1070 K had no detectable cracks but up to 5 times rougher surface.

As stated earlier, infrared thermography was used to measure the sample sur-

face temperature during exposure. In figure 4.29 is plotted the temperature evolution (IR) on the surface during one plasma shot in He including 900 plasma pulses, which were generated at a frequency of 10 Hz, during 100 s of total plasma exposure. Heat fluxes deposited on the tungsten samples (table 4.9) were calculated from the measured temperature profiles using THEODOR code [49] which solves numerically the heat conduction equation [50]:

$$\rho C dT(x,t)/dt = \nabla(-k dT(x,t)/dx). \tag{4.1}$$

C and k are the temperature dependent heat capacity and heat conduction coefficient and T(x,t) is the time dependent measured temperature on the surface. The real surface temperature was calculated by considering the temperature dependent emission coefficients, assuming that the whole area of interest had the same background temperature which was already known. The boundary conditions were defined from the heat conductivity coefficients at the top and at the bottom of the sample. The heat conductivity coefficient at the top of the sample was dependent on the measured temperature evolution with the IR camera on the surface while at the bottom it was related to the calculated temperature on the back of the sample, including the sample holder ,which transmission coefficient could be found empirically [51].

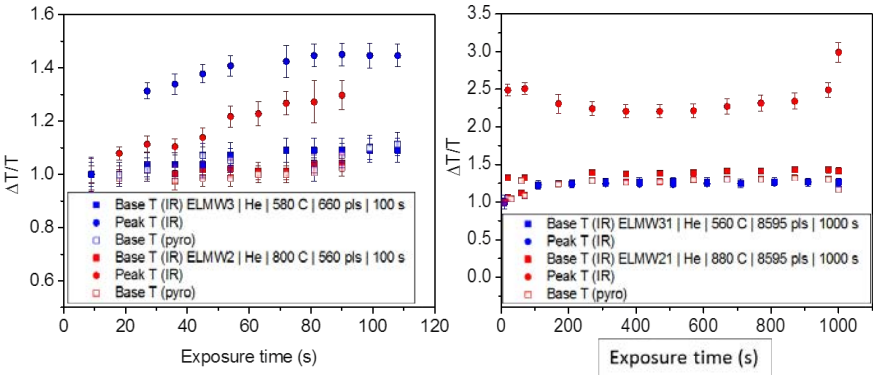

Figure 4.33: ΔT is normalized over the first pulses and plotted versus exposure time for all samples exposed to He transients. On the left plot, samples were exposed to the pulsed plasma source (560, 660 pulses) and on the right one, a laser was used to get 8595 pulses

In figure 4.33 and 4.34 are plotted the exposure time dependence of ΔT which is normalized over the first pulses for base and peak temperatures, as calculated from the IR camera measurements. On the left plot in figure 4.33, samples were exposed to He plasma pulses for about 100 s (ELMW2, ELMW3). Base temperature and emissivity remained rather constant, while the peak temperature increased up to 1.45 compared to the first pulse temperature. Similar increasing trend was

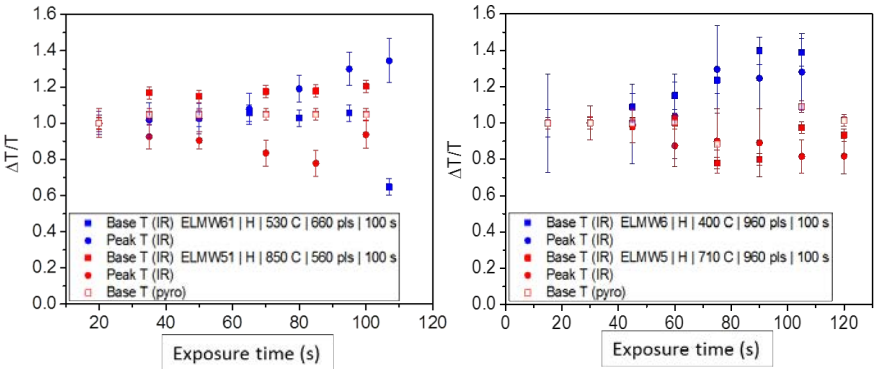

Figure 4.34: ΔT is normalized over the first pulses and plotted versus exposure time for all samples exposed to H transients. In both cases, the pulsed plasma source was used to achieve 560 and 660 pulses (on the left) and 960 pulses (on the right plot)

observed for both samples, indicating deterioration of the thermal conductivity of tungsten surface. In case of the right graph (ELMW21, ELMW31), the increase of the peak temperature at high exposure temperature could be attributed to the Mo porous layer formed on the surface which reached up to 1 μm thickness.

Base and peak temperatures in case of H exposures (figure 4.34) didn't reveal a clear dependence, except for the low exposure temperature where the peak temperature increased up to 1.4 compared to the first plasma pulse.

Sample name	Gas	Base T (K)	Pulse nr.	Particle flux ($m^{-2}s^{-1}$)	Exposure time (s)	Fluence (m^{-2})
ELMW3	He (+10% H)	850	660	7.7E23	99	7.7E25
ELMW2	He (+10% H)	1070	560	7.6E23	99	7.6E25
ELMW31	He	830	8595 (laser)	1,4E24	1000	1.4E27
ELMW21	He	1150	8595 (laser)	1,3E24	1000	1.3E27
IGW5	He	770		1,7E24	100	1.7E26
IGW6	He	1070		1,5E24	100	1.5E26
IGW3	He	770		1,6E24	1000	1.6E27
IGW4	He	1070		1,5E24	1000	1.5E27
ELMW61	H	800	660	3,4E23	107	3.6E25
ELMW51	H	1120	560	3,2E23	100	3.2E25
ELMW6	H	670	960	2.8E23	105	2.9E25
ELMW5	H	980	960	3.0E23	105	3.1E25
IGW61	H	770		3,8E23	100	3.8E25
IGW51	H	1170		4,8E23	100	4.8E25

Table 4.8: ITER-grade tungsten samples exposed in Pilot-PSI linear plasma device to He and H plasmas, under steady-state conditions and transient heat and particle loads. The highlighted samples were deposited with Mo during the plasma exposure.

Sample name	Delta T (K)	Energy density (MJm^{-2})	Peak power density (MWm^{-2})	Baseline power density (MWm^{-2})	Roughness R_a (nm)	Mo content Wt%	Mo layer μm
ELMW3	320	∼0.3	200-300	4.4	37	38.36	0.132
ELMW2	240	∼0.2	180-230	5.5	44	27.17	0.078
ELMW31	350	∼0.27	230-270	4.5	53	74.05	1.094
ELMW21	420	∼0.29	150-420	6.1	57	68.16	1.2
IGW5					26	79.83	
IGW6					48	83.91	
IGW3					29	78.8	4.49
IGW4					51	75.18	1.87
ELMW61	570	∼0.25	230-330	5.1	118		
ELMW51	720	∼0.32	310-390	5.7	120		
ELMW6	370	∼0.2	120-180	6.4	38		
ELMW5	490	∼0.2	130-320	4.8	207		
IGW61					30		
IGW51					29		

Table 4.9: ITER-grade tungsten samples exposed in Pilot-PSI linear plasma device to He and H plasmas, under steady-state conditions and transient heat and particle loads. The highlighted samples were deposited with Mo during the plasma exposure.

References

[1] Material Specification for the Supply of Tungsten Bars for the ITER Divertor. *IDM Number: ITER_D_2X38PN v. 1.0*. 2010.

[2] M. Balden. *et al. Deuterium retention and morphological modifications of the surface in five grades of tungsten after deuterium plasma exposure*. Journal of Nuclear Materials, 452:248–256, 2014.

[3] H. Y. Xu. *et al. Observations of orientation dependence of surface morphology in tungsten implanted by low energy and high flux D plasma*. Journal of Nuclear Materials, 443:452–457, 2013.

[4] H. Y. Xu. *et al. Deuterium-induced nanostructure formation on tungsten exposed to high-flux plasma*. Journal of Nuclear Materials, 2014.

[5] R. A. Causey. *Hydrogen isotope retention and recycling in fusion reactor plasma-facing components*. Journal of Nuclear Materials, 300:91–117, 2002.

[6] E. Kautto. *et al. Analysing Methods for Thermal Desorption Spectra*. Physica Scripta, 55:628–633, 1997.

[7] V. Alimov. *et al. Temperature dependence of surface morphology and deuterium retention in polycrystalline ITER-grade tungsten exposed to low-energy, high-flux D plasma*. Journal of Nuclear Materials, 420:519–524, 2012.

[8] G. Luo. *et al. Incident energy dependence of blistering at tungsten irradiated by low energy high flux deuterium plasma beams*. Journal of Nuclear Materials, 347:111117, 2005.

[9] A. Manhard. *Deuterium Inventory in Tungsten After Plasma Exposure: A Microstructural Survey*. PhD thesis, Universitat Augsburg, 2011.

[10] W. M. Shu. *et al. Recent findings on blistering and deuterium retention in tungsten exposed to high-fluence deuterium plasma*. Journal of Nuclear Materials, 386-388(C):356–359, 2009.

[11] V. Alimov. *et al. Surface morphology and deuterium retention in tungsten exposed to low-energy, high flux pure and helium-seeded deuterium plasmas*. Physica Scripta, T138:014048, 2009.

[12] W. Shu. *et al. Temperature dependence of blistering and deuterium retention in tungsten exposed to high-flux and low-energy deuterium plasma*. Fusion Engineering and Design, 83:10441048, 2008.

[13] G. N. Luo. *et al. Influence of blistering on deuterium retention in tungsten irradiated by high flux deuterium 10-100 eV plasmas*. Fusion Engineering and Design, 81:957962, 2006.

[14] Y.Z. Jia. *et al. Surface morphology and deuterium retention in tungsten exposed to high flux D plasma at high temperatures*. Journal of Nuclear Materials, 457:213219, 2015.

[15] Hong-Bo Zhou. *et al. Investigating behaviours of hydrogen in a tungsten grain boundary by first principles: from dissolution and diffusion to a trapping mechanism*. Nuclear Fusion, 50:025016, 2010.

[16] R. Frauenfelder. *Solution and Diffusion of Hydrogen in Tungsten*. Journal of Vacuum Science and Technology, 6:388, 1969.

[17] A. A. Haasz. *et al. Deuterium retention in single crystal tungsten*. Journal of Nuclear Materials, 290-293:85–88, 2001.

[18] T Yalcinkaya. *et al. BCC single crystal plasticity modeling and its experimental identification*. Modelling and Simulation in Materials Science and Engineering, 16(8):085007, 2008.

[19] V. Alimov. *et al. Depth distribution of deuterium in single- and polycrystalline tungsten up to depths of several micrometers*. Journal of Nuclear Materials, 337339:619623, 2005.

[20] S. Lindig. *et al. Subsurface morphology changes due to deuterium bombardment of tungsten*. Physica Scripta, 014040 (5pp), 2009.

[21] C. R. Weinberger. *et al. Slip planes in bcc transition metals*. International Materials Reviews, 58(5):296–314, 2013.

[22] K. Tokunaga. *et al. Blister formation and deuterium retention on tungsten exposed to low energy and high flux deuterium plasma*. Journal of Nuclear Materials, 337339:887891, 2005.

[23] J. P. Sharpe. *et al. Retention behavior in tungsten and molybdenum exposed to high fluences of deuterium ions in TPE*. Journal of Nuclear Materials, 390391:709712, 2009.

[24] B. Tyburska. *Deuterium Retention in Carbonand Self-Implanted Tungsten*. PhD thesis, Marie Curie-Sklodowska University, Lublin, Poland, 2010.

[25] B. M. U. Scherzer. *Development of surface topography due to gas implantation*. Springer-Verlag, 1983.

[26] J. Roth and K. Schmid. *Hydrogen in tungsten as plasma-facing material*. Physica Scripta, T145(014031), 2011.

[27] B. Cipiti and G.L. Kulcinski. *Helium and deuterium implantation in tungsten at elevated temperatures*. Journal of Nuclear Materials, 347:298306, 2005.

[28] M. Baldwin. *et al. The effects of high fluence mixed-species (deuterium, helium, beryllium) plasma interactions with tungsten*. Journal of Nuclear Materials, 390391:886890, 2009.

[29] S. Kajita. *et al. Formation process of tungsten nanostructure by the exposure to helium plasma under fusion relevant plasma conditions*. Nuclear Fusion, 49(6pp):095005, 2009.

[30] G. De Temmerman. *et al. Nanostructuring of molybdenum and tungsten surfaces by low-energy helium ions*. Journal of Vacuum Science and Technology, A 30(041306), 2012.

[31] M. Li. *et al. Radiation damage of tungsten surfaces by low energy helium atom bombardment A molecular dynamics study*. Journal of Nuclear Materials, 433:1722, 2013.

[32] Zhang Fu. *et al. Thermal desorption and surface modification of He+ implanted into tungsten*. Journal of Nuclear Materials, 329333:692–696, 2004.

[33] M. Baldwin. *et al. Nanostructure formation on tungsten exposed to low-pressure rf helium plasmas: A study of ion energy threshold and early stage growth*. Journal of Nuclear Materials, 415:S104S107, 2011.

[34] M. J. Baldwin and R. P. Doerner. *Helium induced nanoscopic morphology on tungsten under fusion relevant plasma conditions*. Nuclear Fusion, 48:035001 (5pp), 2008.

[35] R. P. Doerner. *et al. An equlibrium model for tungsten fuzz in an eroding plasma envinronment*. Nuclear Fusion, 51(043001), 2011.

[36] S. I. Krasheninikov. *Viscoelastic model of tungsten fuzz growth*. Physica Scripta, T145(014040):4pp, 2011.

[37] A. Lasa. *et al. Loop punching and bubble rupture causing surface roughening - A model for W fuzz growth*. EPL, 105(25002).

[38] M. Reinhart. *Influence of impurities on the fuel retention in fusion reactors*. PhD thesis, Fakultat fuer Physik und Astronomie der Ruhr-Universitat Bochum, 2015.

[39] D. Nishijima. *et al. Suppression of blister formation and deuterium retention on tungsten surface due to mechanical polishing and helium pre-exposure*. Nuclear Fusion, 45(7):669–674, 2005.

[40] M. Miyamoto. *et al. Observations of suppressed retention and blistering for tungsten exposed to deuterium-helium mixture plasmas*. Nuclear Fusion, 49(6), 2009.

[41] M. Miyamoto. *et al. Microscopic damage of tungsten exposed to deuterium-helium mixture plasma in PISCES and its impacts on retention property*. Journal of Nuclear Materials, 415:S657S660, 2011.

[42] Y. Ueda. *et al. Simultaneous irradiation effects of hydrogen and helium ions on tungsten*. Journal of Nuclear Materials, 386-388:725–728, 2009.

[43] H. T. Lee. *et al. Hydrogen and helium trapping in tungsten under simultaneous irradiations*. Journal of Nuclear Materials, 363365:898903, 2007.

[44] R. Pitts. *Response of tungsten surfaces to helium plasma exposure under ITER relevant steady state and repetitive (sub-melting threshold) transient conditions. Technical Specifications*. https://user.iter.org/?uid=NEAK42, 2014.

[45] R. Pitts. *et al. A full tungsten divertor for ITER: Physics issues and design status*. Journal of Nuclear Materials, 438(S48S56), 2013.

[46] J. Rapp. *et al. Plasma-facing materials research for fusion reactors at FOM Rijnhuizen*. Romanian Journal of Physics, 56:30–35, 2011.

[47] G. De Temmerman. *et al. High heat flux capabilities of the Magnum-PSI linear plasma device*. Fusion Engineering and Design, 88:483, 2013.

[48] J. Scholten. *et al. Operational status of the Magnum-PSI linear plasma device*. Fusion Engineering and Design, 88:17851788, 2013.

[49] A. Hermann. *et al. Energy flux to the ASDEX-Upgrade diverter plates determined by thermography and calorimetry*. Plasma Physics and Controlled Fusion, 37:17, 1995.

[50] T. Eich. *et al. ELM resolved energy distribution studies in the JET MKII Gas-Box divertor using infra-red thermography*. Plasma Physics and Controlled Fusion, 49:573604, 2007.

[51] T. Morgan. *et al. A high-repetition rate edge localised mode replication system for the Magnum-PSI and Pilot-PSI linear devices*. Plasma Physics and Controlled Fusion, 56(10pp):095004, 2014.

5
Conclusions and outlook

Plasma parameters at the surface of the ITER divertor will vary in a broad range, therefore the main focus of this thesis was to assess their impact on tungsten, as the plasma facing material. The new findings obtained in this study, shed light on the main question concerning the impact of particle flux on surface modifications and deuterium retention. The role of material microstructure, plasma impurities, and particle and heat transients, were addressed.

In the frame of analyzing the trapping and diffusion processes of deuterium, experiments were carried out on "as-received" polycrystalline, recrystallized and single crystal tungsten samples. The aim was to separate the effects of grain boundaries and crystallographic defects of the material. Single crystals had a low dislocation density while thermal treatment at high temperatures increased the grain size and decreased the dislocation density to negligible levels allowing identifying the role of grain boundaries in deuterium trapping and diffusion.

Polycrystalline (thermally treated at 1273 K and recrystallized at 2273 K) and single crystal tungsten samples (110 orientation) were exposed to the same plasma fluence of $10^{26}\ m^{-2}$ and ion energy of 40 eV. The exposure temperature was varied between 510 and 1170 K. Deuterium flux, therefore the exposure time, varied within two orders of magnitude ($\sim 10^{22}$ - $\sim 10^{24}\ m^{-2}s^{-1}$). This approach was accomplished by using linear plasma devices such as PSI-2 and Magnum/Pilot-PSI which are able to generate fluxes in the required range.

These experiments showed that surface modifications depend strongly on the exposure temperature and ion flux density. After exposure to high particle flux density, blisters of lateral size 0.05-1 μm appeared on annealed polycrystalline and on single crystal tungsten samples. Blistering persisted even at temperatures above 700 K where, exposures to lower particle flux density, blistering is normally suppressed due to the thermal desorption of deuterium during plasma exposure.

The factors that could influence the appearance of blisters in the case of high flux density compared to the low flux density exposure are related to the heat dissipation into the bulk and an excessive amount of deuterium in the implantation zone due to the low solubility and diffusion to the bulk or recombination at the surface. Moreover, exposure to high particle flux density led to the formation of additional defects in the crystal which may form trapping sites for deuterium and act as centers for bubble nucleation.

However, blisters were completely absent on recrystallized samples after exposure to high flux densities due to the low dislocation density and enhanced diffusion through the grain boundaries. It was also found that the direction of lenticular cavities formed in single crystal tungsten samples was related to the gliding in the low-index slip system mechanism. Results suggested that at temperatures below 670 K, dislocations move along the (110) <111> gliding system, while at higher exposure temperatures, (112) <111>, (123) <111> and (221) <111> systems were more favorable.

Deuterium retention was measured by means of thermal desorption spectroscopy (TDS) and nuclear reaction analysis (NRA). It was found that the maximum of deuterium retention depends on the incident ion flux at a given fluence and ion energy. It increases with increasing the ion flux density. From the TDS measurements it was observed that the maximum of deuterium retention for low flux density ($\sim 10^{22}\ m^{-2}s^{-1}$) was reached at $\sim$650 K and for high flux density ($\sim 10^{22}\ m^{-2}s^{-1}$) at $\sim$850 K. In the cases with low exposure temperatures, the total deuterium retention was one to two orders of magnitude higher after exposure to the low flux compared to the high flux density. On the contrary, an opposite increase of the total deuterium retention at high exposure temperatures was observed for the high particle flux case compared to lower flux density exposures.

Experimental results on deuterium retention show a similar behavior when varying the exposure temperature, for all the investigated microstructures. Deuterium retention decreased at high temperatures and the maximal retention was lower for high flux exposures. However, due to the shift of the maximal retention to higher temperatures, the amount of deuterium retained at temperatures above

800 K was higher at high flux rather than at low flux, being still about one order of magnitude lower than the maximal retention at low flux. Extrapolating the TDS values under exposure conditions used in this study to ITER, total deuterium inventory from 0.2788 mg (500-700 K) to 1.4 mg (500-900 K) would accumulate in 210 m^2 of surface area per plasma pulse, assuming an average inventory of 10^{22} and $5 \cdot 10^{20}$ Dm^{-2} at low and high flux, respectively. However, considering the small divertor area which will be exposed to such high fluxes and thermal desorption during ITER discharges, the total inventory might not be of large significance.

The trends of deuterium retention in tungsten can be attributed to the interplay of processes of damage creation, deuterium recycling and return back into plasma, and deuterium diffusion deeper into the bulk. For the same total fluence, low flux exposures correspond to longer exposure times than high flux exposures. At low flux and high temperature, long exposure times allow for deuterium diffusion into the bulk, as well as for desorption at the plasma facing surface. At high flux, larger concentration gradients of deuterium can be expected to be build, leading potentially to stronger material damage and/or faster growth of deuterium filled bubbles or voids. At the same time, diffusion of deuterium deep into the material allows for deuterium trapping at intrinsic lattice defects, such as vacancies, dislocations and grain boundaries in case of polycrystalline samples. For typical grain sized of about several μm to several tens of μm, short exposure times do not allow for efficient deuterium diffusion to grain boundaries, so it is then presumably trapped at intra-granular defects.

Modeling of the measured thermal desorption spectra was performed using the rate equations approach implemented in the Coupled Reaction Diffusion Systems (CRDS) code. The TDS peaks could be reproduced assuming either one trapping energy of 2.2 eV (recrystallized tungsten) or two trapping energies of 1.9 eV and 2.0 eV for single crystal tungsten and 2.0 eV and 2.3 eV for other polycrystalline samples. The deuterium depth profiles from NRA, were assumed as trap profiles. Re-trapping of deuterium at defects was not taken into account in order to simulate the thin experimental profiles, while de-trapping frequency was adjusted to values about 120-500 times lower than typical Debye frequencies.

With such a setup, CRDS simulations indicate that to better reproduce the high temperature tail of TDS peaks for high temperature exposure samples, as well as for low flux cases, deeper retention profiles of deuterium than measured by NRA have to be assumed. In particular, a low density of intrinsic traps of about $5 \cdot 10^{-4}$ at.$\%$ up to mm scale was used in the recrystallized tungsten cases. This was in line with the assumption of deeper deuterium diffusion at high temperatures and longer exposure times. Simulations indicate that deuterium can diffuse even up

to the opposite side of 4-mm thick samples during long exposure time. CRDS simulations confirmed the deeper deuterium diffusion at higher temperatures and exposure time.

Helium will be present in ITER during nuclear and non-nuclear phase of operation. A set of experiments was dedicated to the influence of He impurities in D plasma, typically 5% of He ions, and its impact on the flux dependence of deuterium retention and surface morphology. Recrystallized tungsten samples were exposed to a temperature range 520-1090 K at particle flux densities of $\sim 10^{22}$ $m^{-2}s^{-1}$ at the PISCES-A linear plasma device. The total ion fluence was 10^{26} m^{-2}. Scanning electron microscopy revealed that the surface was roughened at lower temperatures (520 K) the surface was roughened and at 720 K, small pinholes of a few nanometers appeared on the surface. Exposure of recrystallized samples at 1090 K caused the formation of nanorods which reached a length of above 200 nm.

NRA measurements indicated that deuterium concentration dropped up to two orders of magnitude when 5% of He was added to pure D plasma. When temperature increased to 720 K, deuterium content dropped even further. A common feature of deuterium depth profiles is the fact that retention dropped considerably in the first 50 nm. The argument of deuterium intake suppression after exposure to helium seeded plasmas is based on the He bubble formation in the implantation zone where D is trapped at the periphery of He bubbles. Therefore, the induced porosity empties the implantation zone from where deuterium diffusion takes place.

The material response to steady state and transient particle and heat loads during edge localized modes (ELMs) under ITER relevant conditions was considered in the experiments. A set of experiments was carried out addressing the effect of He nano-bubble layer formed in the near surface region of tungsten under ITER relevant steady state and transient heat and particle loads, simulating ITER ELMs in terms of amplitude, frequency and flux densities. The changes on the surface thermal conductivity and the bubble growth rate were investigated and compared with the relevant exposures in hydrogen.

Exposure to He plasma pulses caused the formation of fine cracking network on tungsten samples which occurred at a higher density and smaller depths compared to hydrogen pulsed plasma irradiation. The peak temperature, after exposure to H and He pulsed plasma at 850 K, increased with the same factor of 1.4 compared to the first plasma pulse, indicating a reduction of the power exhaust capability of the target.

Overall, this work brought a substantial amount of new results and analysis, enriching the database especially at high particle flux exposures by providing a systematical investigation. The simulation of the TDS data with the CRDS code was another added value to this contribution, which allowed having an insight on the trapping mechanisms of deuterium in tungsten. However, the results presented here, give the opportunity for further investigations:

Future work could be focused on studying the behavior of deuterium retention from temperature at higher particle fluence. An estimation of the critical fluence which leads to nanostructure formation, at high particle flux densities and temperatures, could be of interest for future fusion devices. In this work, the particle fluence was fixed to $10^{26}\ m^{-2}$. Achieving larger fluences (i.e up to $10^{28}\ m^{-2}$) at low particle flux is rather challenging as the exposure time can be very long, which is not the case for high flux generators.

In the frame of future work, the impact on deuterium retention and blistering can be studied when He or other impurities (i.e Be) are present in the plasma, at high particle flux ($10^{24}\ m^{-2}s^{-1}$). In addition, the impact of particle and heat transient loads in He and H plasma on the bubble layer formation and cracking, could be studied for longer exposure times, various incident ion energies and impurity seeding (i.e N).

A Material selection

A.1 Chemical content and material specifications of tungsten bars

Element	Composition max. wt. %	Permissible variation in wt. %
C	0.01	± 0.002
O	0.01	$+10\%$ relative
N	0.01	+0.0005
Fe	0.01	+0.001
Ni	0.01	+0.001
Si	0.01	+0.001

Table A.1: Chemical composition of W bars

Width x height (mm)	Grain size [ASTM number]
$< 34 \times 34$	6 and finer
$> 34 \times 34$	5 and finer
Density	$\geq 19.0 g/cm^3$
Vickers hardness	$HV30 > 410$

Table A.2: Grain size of the W bar. Samples were cut perpendicular to the rolling direction

B

D experiments

B.1 TDS profiles of tungsten samples after exposure to pure D plasma

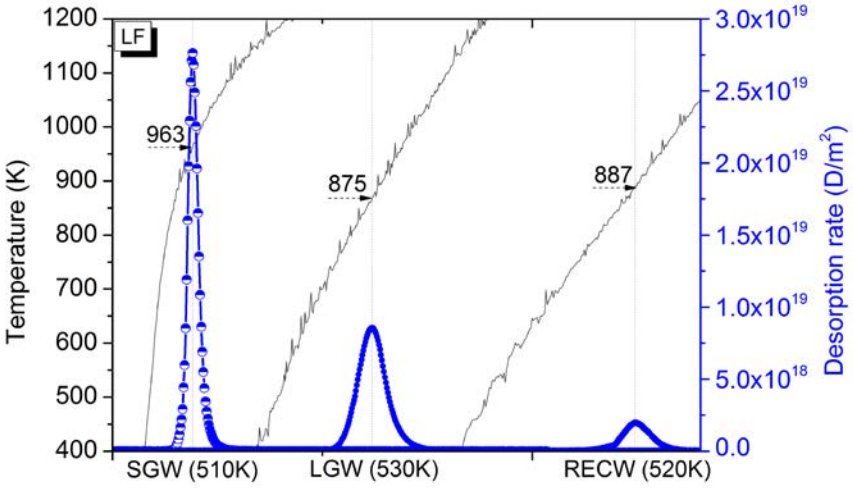

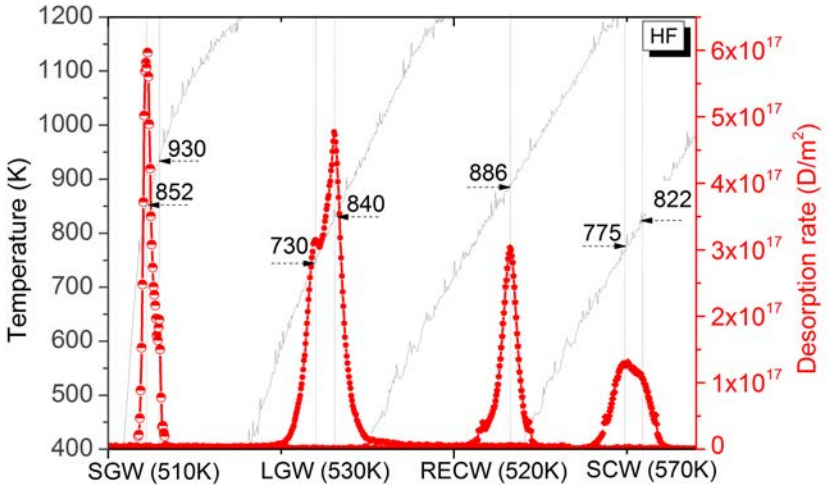
HF
Temperature (K)
Desorption rate (D/m^2)
930
852
730
840
886
775
822
SGW (510K)
LGW (530K)
RECW (520K)
SCW (570K)

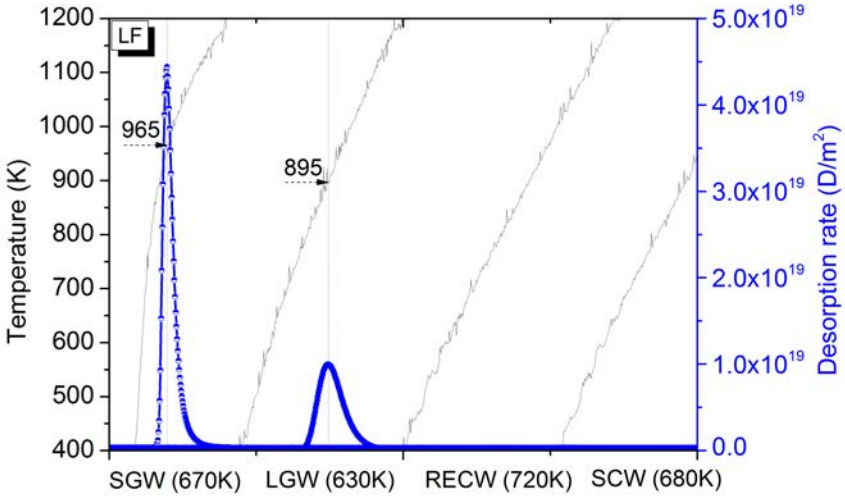
LF
Temperature (K)
Desorption rate (D/m^2)
965
895
SGW (670K)
LGW (630K)
RECW (720K)
SCW (680K)

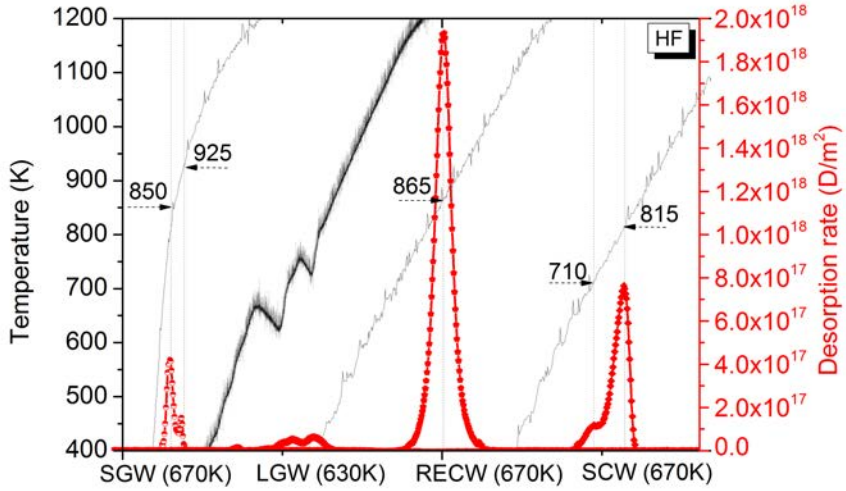
HF
Temperature (K)
Desorption rate (D/m²)
850
925
865
815
710
SGW (670K)
LGW (630K)
RECW (670K)
SCW (670K)

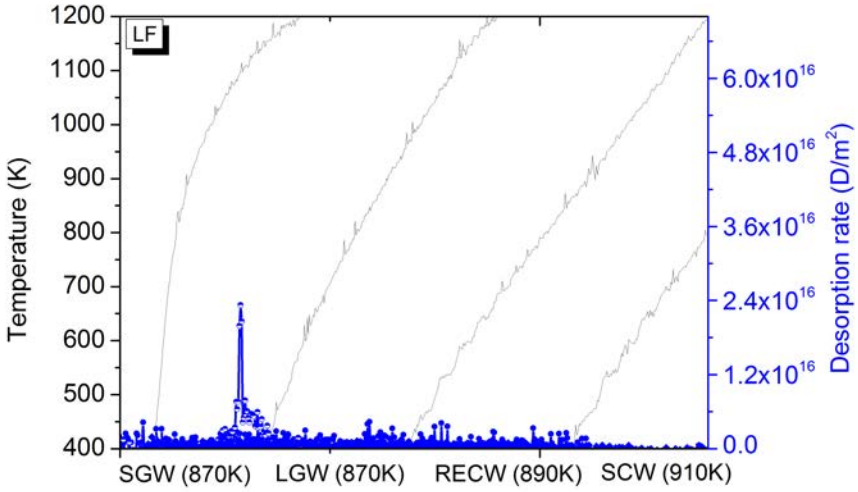
LF
Temperature (K)
Desorption rate (D/m²)
SGW (870K)
LGW (870K)
RECW (890K)
SCW (910K)

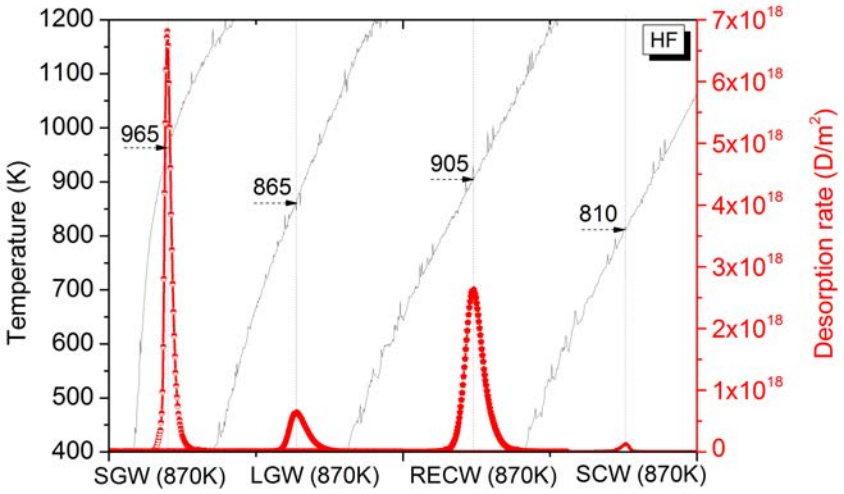
HF
965
865
905
810
Temperature (K)
Desorption rate (D/m²)
SGW (870K)
LGW (870K)
RECW (870K)
SCW (870K)

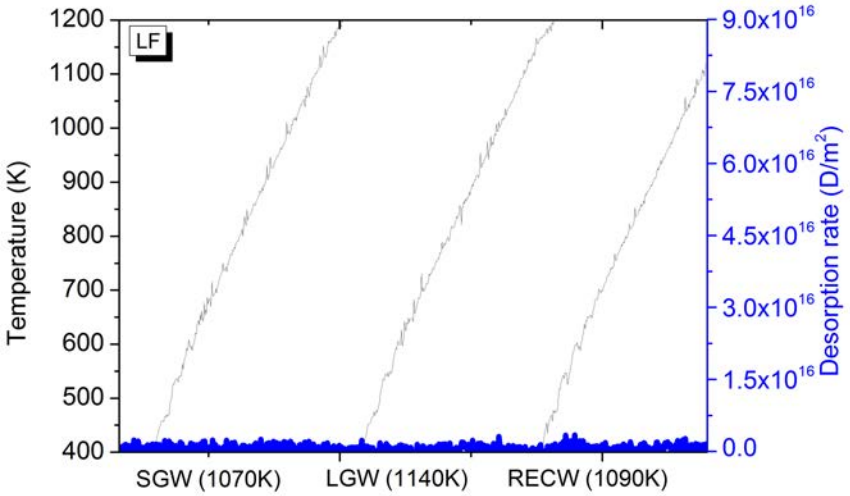
LF
Temperature (K)
Desorption rate (D/m²)
SGW (1070K)
LGW (1140K)
RECW (1090K)

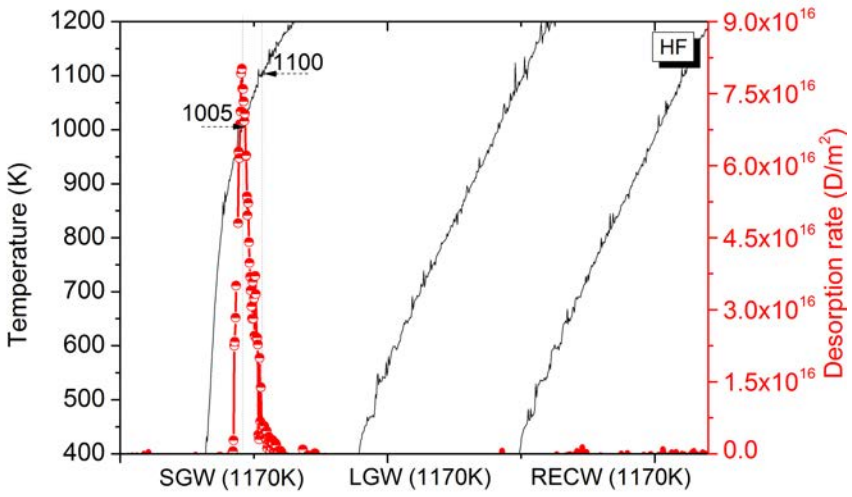
1200
1100
1000
900
800
700
600
500
400
Temperature (K)
9.0x10^16
7.5x10^16
6.0x10^16
4.5x10^16
3.0x10^16
1.5x10^16
0.0
Desorption rate (D/m^2)
1100
1005
HF
SGW (1170K)
LGW (1170K)
RECW (1170K)

C

He/H experiments

C.1 Surface analysis of Mo-deposited tungsten samples after exposure to H and He plasma

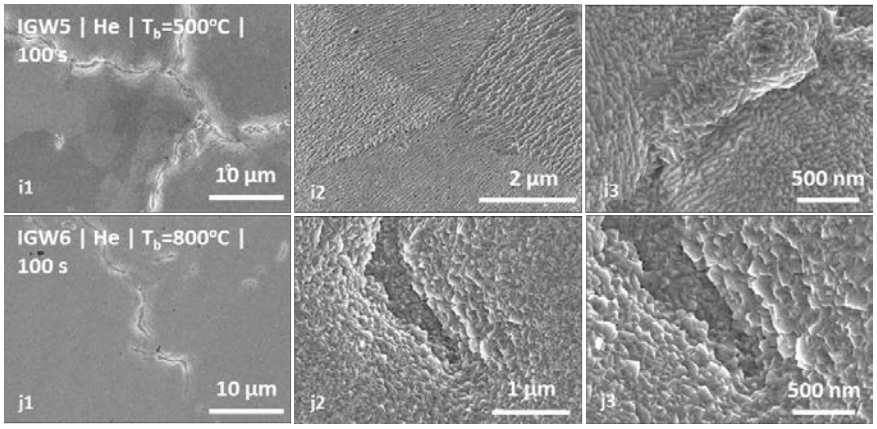

Figure C.1: SEM images on the ITER-grade tungsten samples exposed at Pilot-PSI to steady state He plasma for 100 s

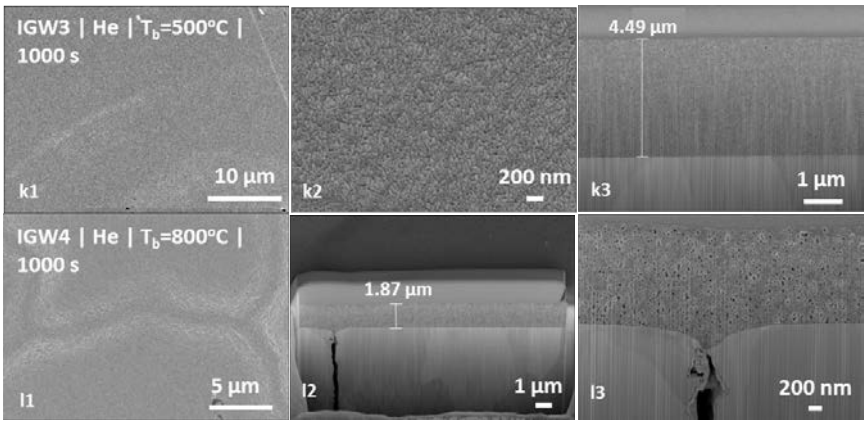

Figure C.2: SEM images on the ITER-grade tungsten samples exposed at Pilot-PSI to steady state He plasma for 1000 s

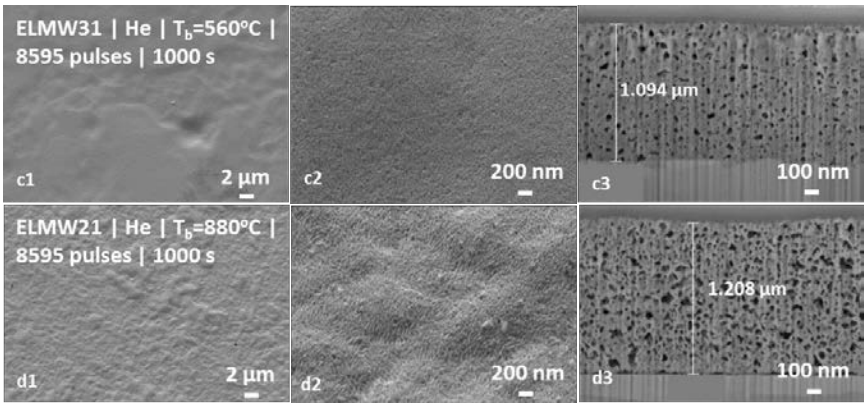

Figure C.3: SEM images on the ITER-grade tungsten samples exposed at Pilot-PSI to He plasma for 1000 s and 8595 laser pulses

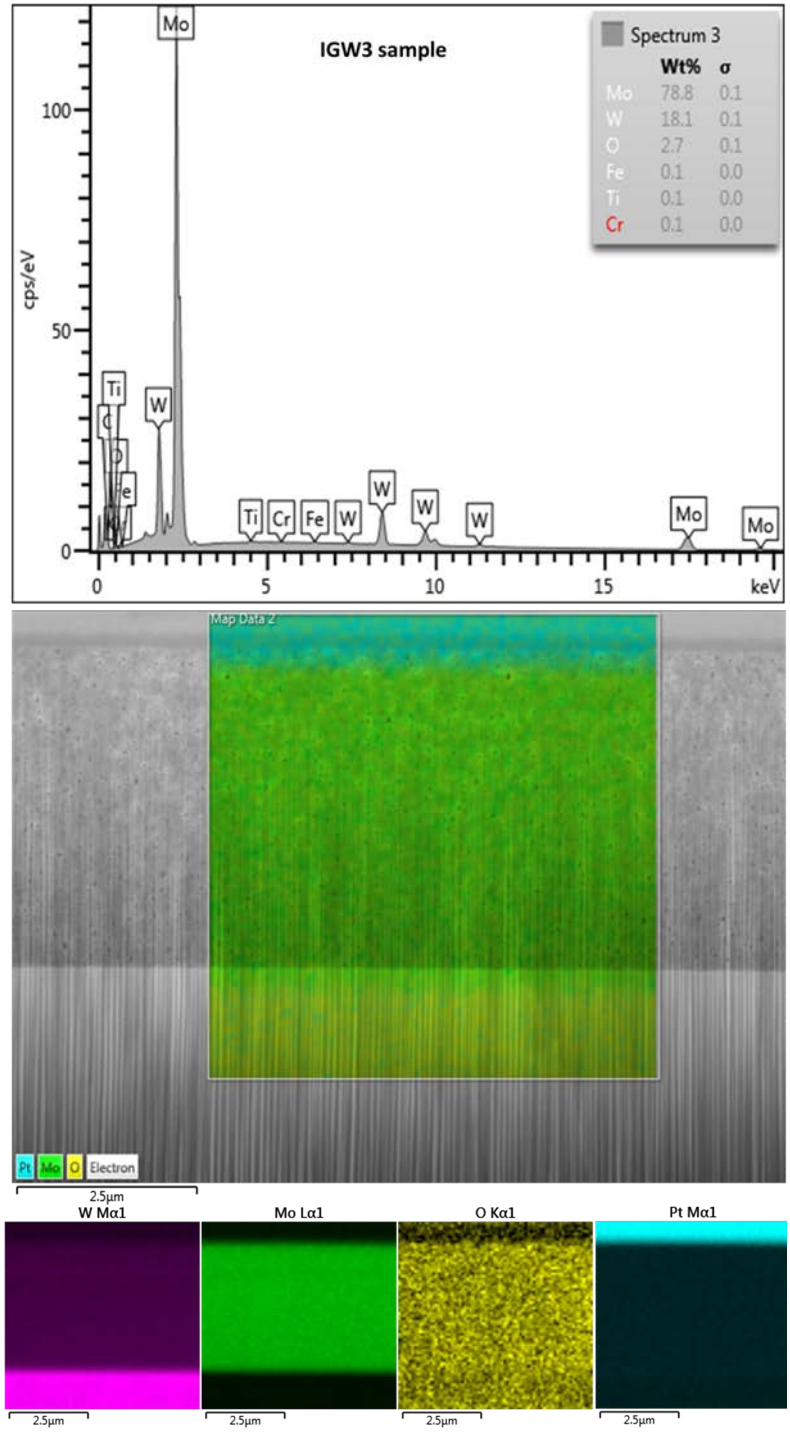

Figure C.4: Elemental analysis performed with EDX on the IGW3 sample after exposure to steady state He plasma for 1000 s.